CONTENTS

	Page	
SUMMARY	1	1/A5
NOMENCLATURE	3	1/A7
1. INTRODUCTION	5	1/A9
2. EXPERIMENTAL FACILITY	9	1/A13
3. EXPERIMENTAL PROCEDURES AND DATA REDUCTION	18	1/B9
3.1 Typical Test Runs	18	1/B9
3.2 Segment Heat Transfer Coefficients	18	1/B9
3.3 Corrections and Experimental Uncertainties	20	1/B11
3.4 Reproducibility	22	1/B13
4. EXPERIMENTAL RESULTS	23	1/B14
4.1 Presentation Variables and Parameters	23	1/B14
4.2 Documentation of Data Base	25	1/C2
4.3 Geometrically Similar Configurations	26	1/C3
4.3.1 Mean Nusselt Numbers	26	1/C3
4.3.2 Low-Resolution Nusselt Number Profiles	27	1/C4
4.3.3 Statistical Analysis	32	1/C9
4.4 Low-Resolution Heat Transfer Characteristics	36	1/C13
4.4.1 Effect of Channel Height	36	1/C13
4.4.2 Effect of Hole Diameter	37	1/C14
4.4.3 Effect of Hole Spacing	39	1/D2
4.4.4 Effect of Hole Pattern	40	1/D3
4.5 Higher-Resolution Heat Transfer Characteristics	42	1/D5
5. SUMMARY OF RESULTS	54	1/E10
6. CONCLUDING REMARKS	56	1/F9
REFERENCES	58	1/E14
APPENDIX A - CORRECTION FOR SEGMENT HEAT TRANSFER COEFFICIENTS DUE TO SURFACE TEMPERATURE DEPRESSION AT TEST PLATE SEGMENT INTERFACES	60	1/F2
APPENDIX B - TABULAR DATA	64	1/F6

Item 830-H-14 NAS1.26:3217

JAN 81 [redacted]

NASA Contractor Report 3217

COMPLETED

ORIGINAL

Multiple Jet Impingement Heat Transfer Characteristic - Experimental Investigation of In-Line and Staggered Arrays With Crossflow

L. W. Florschuetz, D. E. Metzger,
D. I. Takeuchi, and R. A. Berry

GRANT NSG-3075
JANUARY 1980

NASA

86

NASA Contractor Report 3217

Multiple Jet Impingement Heat Transfer Characteristic - Experimental Investigation of In-Line and Staggered Arrays With Crossflow

L. W. Florschuetz, D. E. Metzger,
D. I. Takeuchi, and R. A. Berry
Arizona State University
Tempe, Arizona

Prepared for
Lewis Research Center
under Grant NSG-3075

National Aeronautics
and Space Administration

**Scientific and Technical
Information Office**

1980

CONTENTS

	Page
SUMMARY	1
NOMENCLATURE	3
1. INTRODUCTION	5
2. EXPERIMENTAL FACILITY	9
3. EXPERIMENTAL PROCEDURES AND DATA REDUCTION	18
3.1 Typical Test Runs	18
3.2 Segment Heat Transfer Coefficients	18
3.3 Corrections and Experimental Uncertainties	20
3.4 Reproducibility	22
4. EXPERIMENTAL RESULTS	23
4.1 Presentation Variables and Parameters	23
4.2 Documentation of Data Base	25
4.3 Geometrically Similar Configurations	26
4.3.1 Mean Nusselt Numbers	26
4.3.2 Low-Resolution Nusselt Number Profiles	27
4.3.3 Statistical Analysis	32
4.4 Low-Resolution Heat Transfer Characteristics	36
4.4.1 Effect of Channel Height	36
4.4.2 Effect of Hole Diameter	37
4.4.3 Effect of Hole Spacing	39
4.4.4 Effect of Hole Pattern	40
4.5 Higher-Resolution Heat Transfer Characteristics	42
5. SUMMARY OF RESULTS	54
6. CONCLUDING REMARKS	56
REFERENCES	58
APPENDIX A - CORRECTION FOR SEGMENT HEAT TRANSFER COEFFICIENTS DUE TO SURFACE TEMPERATURE DEPRESSION AT TEST PLATE SEGMENT INTERFACES	60
APPENDIX B - TABULAR DATA	64

SUMMARY

Extensive experimental results for heat transfer characteristics have been obtained for configurations designed to model the impingement cooled midchord region of air cooled gas turbine airfoils. The configurations tested were in-line and staggered two-dimensional arrays of circular jets with ten spanwise rows of holes. The cooling air was constrained to exit in the chordwise direction along the channel formed by the jet orifice plate and the heat transfer surface. Tests were run for chordwise jet hole spacings of five, ten, and fifteen hole diameters; spanwise spacings of four, six, and eight diameters; and channel heights (jet plate-to-heat transfer surface spacings) of one, two, three, and six diameters. Mean jet Reynolds numbers ranged from $5x10^3$ to $5x10^4$. The thermal boundary condition at the heat transfer test surface was isothermal. Tests were run for sets of geometrically similar configurations of different sizes. Overall, hole diameters ranged from 0.0635 cm to 0.762 cm and heat transfer surface chordwise lengths from 6.35 cm to 38.1 cm. Mean and chordwise resolved Nusselt numbers were determined utilizing a specially constructed test surface which was segmented in the chordwise direction. These are documented in tabular form as a function of mean jet Reynolds numbers and geometric parameters. The characteristics of these results are presented and discussed in graphical form. Results for the maximum chordwise resolution of one-third the chordwise hole spacing, referred to as higher-resolution results, reflect the periodic variations of the chordwise heat transfer coefficient profiles. Results resolved to one or two chordwise hole spacings, referred to as low-resolution results, show more clearly the nature of the profiles smoothed across the periodic variations. A significant characteristic of the low-resolution profiles is the occurrence of a minimum value of the heat transfer coefficient for the smaller channel heights and spanwise hole spacings. For the smallest channel height and spanwise hole spacing (one and four hole diameters, respectively) the downstream heat transfer coefficients are significantly larger than the upstream values. The mean heat transfer coefficients are not very sensitive to channel height, regardless of hole spacings. However, for the smaller spanwise spacings the shapes of the chordwise profiles vary significantly with channel height. For a fixed mass flow rate, the mean heat transfer coefficients vary inversely with hole diameter. Reducing the hole diameter tends to provide a more uniform low-resolution heat transfer coefficient profile, but greatly increases the amplitude of the periodic variations. For a fixed flow rate per unit hole area the mean heat transfer coefficient increases as the holes are spaced more closely, but for a fixed flow rate per unit heat transfer surface area the mean coefficient increases as the holes are spaced farther apart. The low-resolution coefficients also follow these trends, but the chordwise profiles for different hole spacings do not always lie uniformly above or below each other, particularly for the smaller channel heights. As the hole spacing is decreased, inline hole patterns result in higher heat transfer coefficients than staggered patterns, particularly for the larger channel heights and toward the downstream end of the channel. The higher-resolution results show that large periodic variations in heat transfer coefficients exist upstream, and, though damped, can remain significant downstream at the tenth row of holes. However, for the densest hole packing at its largest channel height in the staggered pattern, the variations essentially disappear after the seventh row. These and other characteristics of the results are discussed in detail.

BLANK PAGE

NOMENCLATURE

A = heat transfer surface area of individual test plate segment

A_o^* = ratio of jet hole area to opposing heat transfer surface area (open area ratio)

b = thickness of jet plate

c_p = specific heat at constant pressure

d = jet hole diameter

$\overline{G}$ = mean mass flux based on jet hole area

$\overline{G}^*$ = mean mass flux based on heat transfer surface area

h = convective heat transfer coefficient resolved in chordwise direction, averaged across span

$\overline{h}$ = convective heat transfer coefficient averaged over entire heat transfer surface

k = thermal conductivity of air

ℓ = chordwise length of heat transfer surface

N_c = number of spanwise rows in chordwise direction

N_s = number of jet holes across span of heat transfer surface

N_s' = number of jet holes across span of channel

Nu = Nusselt number resolved in chordwise direction, averaged across span, hd/k

$\overline{Nu}$ = Nusselt number averaged over entire heat transfer surface, $\overline{h}d/k$

P_e = channel exhaust pressure

P_o = plenum pressure

Q = heat rate from individual test plate segment

$\overline{Re}$ = mean jet Reynolds number, $\overline{G}d/\mu$

$\overline{Re}^*$ = mean superficial Reynolds number, $\overline{G}^*d/\mu$

T_o = plenum air temperature

T_r = fluid reference temperature for defining heat transfer coefficient, equivalent to adiabatic wall temperature

T_s = heat transfer surface temperature

x = chordwise location along heat transfer surface measured from upstream end of channel

x_n = chordwise jet hole spacing

y_n = spanwise jet hole spacing

z = channel height or jet plate-to-impingement surface spacing

μ = dynamic viscosity

Note: Symbols as used in Appendix A are defined in nomenclature list within that Appendix.

1. INTRODUCTION

Impingement with high velocity gas jets has become an established method of convectively cooling or heating surfaces in a wide variety of process and thermal control applications. Examples include cooling of gas turbine airfoils and electronic equipment, drying of paper and textiles or other thin layers of films, annealing of metals, and glass tempering operations. The most commonly used jet openings are slots and circular holes. For applications requiring highly localized heating or cooling a single circular jet may suffice. For long, but very narrow areas a single row of circular jets or a single slot jet may be appropriate. The single row or slot may also be adequate, in some cases, for treating sheets of material which can be moved continuously past the row or slot. However, where all portions of a surface of larger expanse must be continuously heated or cooled, multiple slot jets or two-dimensional arrays of jet orifices are required.

For gas turbine engines a significant application utilizing a two-dimensional array of jets is the cooling of the midchord region of stator and turbine airfoils. One such arrangement is illustrated in Fig. 1.1. Impingement air from the midchord array flows rearward along the channel formed between the inlet plenum and the airfoil envelope, discharging at the trailing edge. Flow from the upstream jets in the array imposes a crossflow on those located downstream. In this arrangement air discharged from the jet row provided for cooling of the leading edge is then used to provide localized film cooling, and does not interact with the midchord array jets. However, in alternate arrangements, leading edge cooling air is permitted to flow rearward inside the airfoil envelope where it becomes an initial crossflow influence on the midchord array.

In addition to the increased heat rates attainable relative to nonimpinging flows, the jet array provides the designer with potential for a high degree of control of the distribution of surface heat transfer characteristics. By varying the flow and geometric parameters, including the number, size, and spacing of the jet orifices as well as the orifice plate-to-cooled surface height, the potential exists for adjustment of the heat transfer coefficients to achieve a specified distribution in surface temperature or heat flux.

For the cooled gas turbine airfoil, it should ultimately be possible to account for the variation in the external hot gas heat transfer coefficients and arrive at an optimum internal impingement array that minimizes the required amount of coolant flow. Such an optimum array will, in general, be irregular, but modern chemical machining methods make this quite feasible. Such optimization will require a detailed knowledge of the effect of array geometry on the internal impingement heat transfer characteristics including the effect of the crossflow.

It appears that knowledge of the effects of array configuration on heat transfer characteristics has been inadequate for achievement of optimal designs, even when consideration is restricted to uniformly spaced arrays. Gauntner, et al [1], recently reported results of measurements on an actual gas turbine

vane with midchord cooling provided by a uniformily spaced two-dimensional jet array. These results illuminated the inadequacy of existing correlations for predicting heat transfer performance of such arrays. In particular, the study revealed that questions remained unanswered concerning the important crossflow influence on downstream heat transfer as a function of array geometry.

The present investigation was initiated with the primary objective of determining heat transfer behavior for a range of uniformly spaced array configurations which model those of interest in current and contemplated gas turbine airfoil cooling applications. The first phase of the test program was designed to model impingement cooling of the midchord region according to the scheme indicated in Fig. 1.1. The laboratory configuration used to model this midchord cooling scheme is illustrated schematically in Fig. 1.2. The test facility was designed, however, to also permit subsequent testing in the presence of an initial crossflow introduced upstream of the array.

The original test program included the measurement of both mean and chordwise resolved heat transfer coefficients for uniform rectangular (inline) arrays of jets as a function of flow rate and geometric parameters, with the objective of developing a correlation which would be of direct use to the designer. Subsequently, the program was expanded to include staggered jet hole array patterns as well as determination of chordwise jet flow distributions. The current objective is to develop, for design application, correlations of chordwise resolved heat transfer coefficients as a function of: (1) jet and crossflow rates associated with the individual spanwise jet rows, and (2) geometric parameters. This activity is currently underway.

It is the purpose of this report to provide a description of the basic heat transfer test rig, to document the extensive chordwise resolved and mean heat transfer results obtained for both the inline and staggered array patterns as a function of overall or mean flow rate, and to present and discuss the observed trends and characteristics of the data.

The range of geometric parameters covered is as follows (nomenclature defined in Fig. 1.2):

$$x_n/d = 5, 10, \text{ and } 15$$
$$y_n/d = 4, 6, \text{ and } 8$$
$$z/d = 1, 2, 3, \text{ and } 6$$

The number of spanwise rows of holes for each array was fixed at ten. The thickness of the jet orifice plate was maintained equal to the hole diameter. Results were obtained for mean jet Reynolds numbers from 5×10^3 to 5×10^4. The thermal boundary condition at the test surface was isothermal.

Tests were run for geometrically similar configurations of different sizes in order to examine scaling effects. Overall, hole diameters ranged from 0.0635 cm (0.025 in.) to 0.762 cm (0.3 in) and heat transfer surface chordwise lengths from 6.35 cm (2.5 in.) to 38.1 cm (15.0 in.).

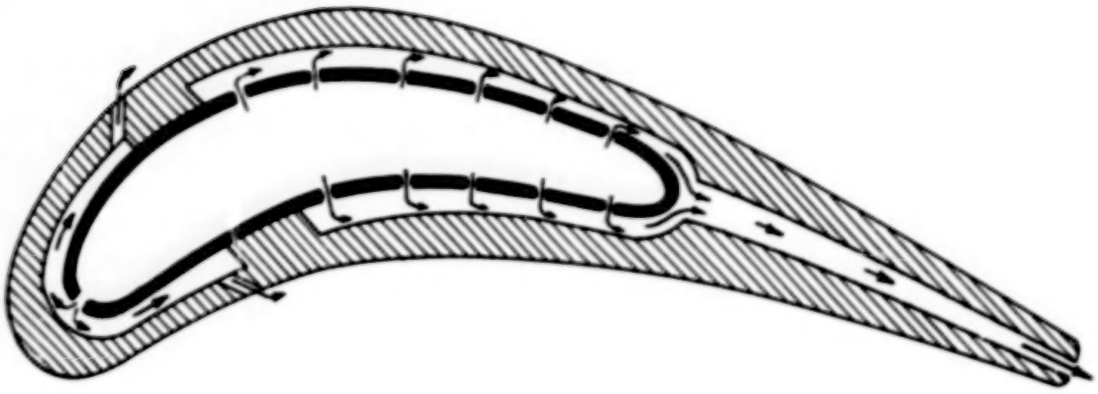

Fig. 1.1 Example of cooled gas turbine airfoil with midchord cooling by jet array impingement scheme.

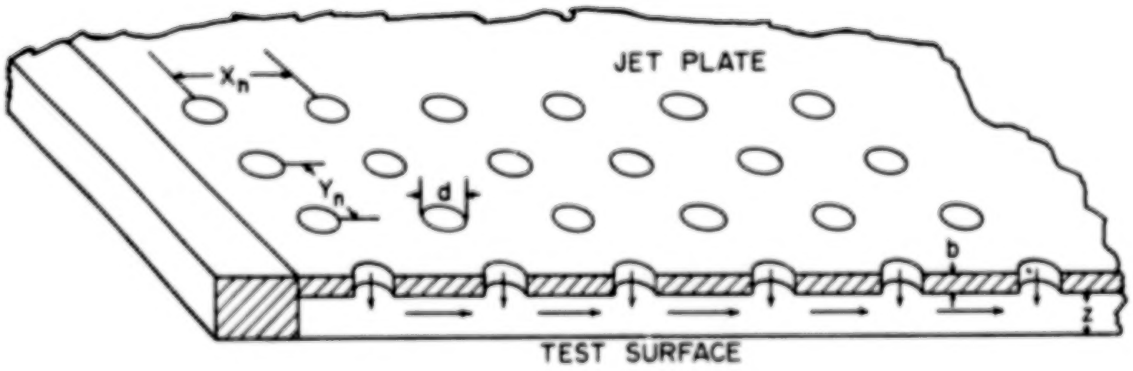

Fig. 1.2 Basic test model geometry and nomenclature.

The larger size configurations permitted better spatial resolution of heat transfer coefficients. The highest chordwise resolution obtained was one-third of the chordwise hole spacing. This resolution permitted observation of pronounced periodic chordwise variations in the heat transfer coefficients. Heat transfer coefficients resolved to one or two chordwise hole spacings do not detect the periodic variations, but show more clearly the chordwise trends smoothed across the periodic variations. Results are presented and discussed in both forms, referred to as low- and higher-resolution results. Some of the low-resolution and preliminary higher-resolution results were previously presented in [2].

Prior heat transfer studies for two-dimensional arrays of circular impinging jets with flow constrained to exit in a single direction parallel to jet hole rows were reported by Friedman and Mueller [3], Huang [4], Kercher and Tabakoff [5], and Chance [6]. These studies provided either mean heat transfer results or were limited to spatial resolutions greater than or equal to one streamwise hole spacing. Studies which included some high resolution measurements, but in which the flow was not constrained to exit in a single direction were carried out by Gardon and Cobonpue [7] and Hollworth and Berry [8]. A recent review of impinging jet flow heat and mass transfer was provided by Martin [9]. Metzger and Korstad [10] measured mean heat transfer coefficients for a single row of circular impinging jets normal to a cross-flowing air stream. High resolution studies of a single circular impinging jet in the presence of a crossflow were carried out by Bouchez and Goldstein [11] and by Sparrow, Goldstein and Rouf [12].

Mr. R. D. Behee participated in the development of the test facility and the early acquisition and reduction of data. Subsequently, valuable assistance in these tasks was provided by Mr. J. M. Bitner and Mr. C. R. Truman.

2. EXPERIMENTAL FACILITY

The test facility consists basically of a compressed air supply, an air flow metering section, and interchangeable plenum/jet plate assemblies which produce arrays of jets impinging on an instrumented heat transfer test surface. Chordwise and spanwise cross-sectional views of the assembly of the major components are shown in Figure 2.1 for one plenum size. A single test plate unit consisting of a segmented copper test plate with individual segment heaters, the necessary thermal insulation, and the test plate support structure, is utilized for all tests. AC power input levels to the segment heaters are individually controlled by separate variacs associated with each heater. The segmented design provides for control of the chordwise thermal boundary condition at the heat transfer test surface, as well as for determination of spatially resolved heat transfer coefficients in the chordwise direction. The jet plate under test, positioned by the jet plate holder, is bolted to the lower flange of the plenum, which is, in turn, bolted to the test plate unit. The jet plate lower surface is positioned relative to the heat transfer surface via interchangeable spacers to permit covering the desired range of channel heights.

Laboratory compressed air is piped to the plenum and passed through the plenum packing to provide a uniform flow upstream of the jet plate. After passing through the jet plate the air exhausts to atmospheric pressure by flowing along the channel formed by the jet plate, the test surface, and the spacer.

There are four interchangeable plenums, each of a different chordwise length, subsequently designated A, B, C, and D in order of increasing length. Thus, the channel length varies depending on the size of the particular plenum/jet plate assembly being utilized. The thermally active length of the test plate consists, for a given test, of those test plate segments which are immediately opposite the jet plate. The maximum active chordwise length is 38.1 cm (15 in.) (30 segments by 1.27 cm (0.5 in.) per segment), with an additional segment at the downstream end to serve as a guard element. For tests utilizing smaller sizes, in which only a fraction of the test plate was thermally active, the segment immediately downstream of the active portion served as a guard element.

The aluminum jet plates were 1.1 cm (7/16 in.) thick for the A and B sizes, and 1.7 cm (11/16 in.) for the C and D sizes, with the jet holes appropriately counterbored to provide a plate thickness at each hole location equal to the jet hole diameter. The larger overall thickness of the jet plate design was dictated primarily by the need to insure accurate channel heights during test runs, a particularly critical requirement for the narrowest channel heights. The counterbore was three jet hole diameters, except for the narrowest hole spacings where two jet hole diameters was used. In one test with a channel height of one jet hole diameter, a 2d counterbore plate was used with the counterbored holes subsequently bored out to 3d, and the test repeated. The results were identical to within experimental uncertainty.

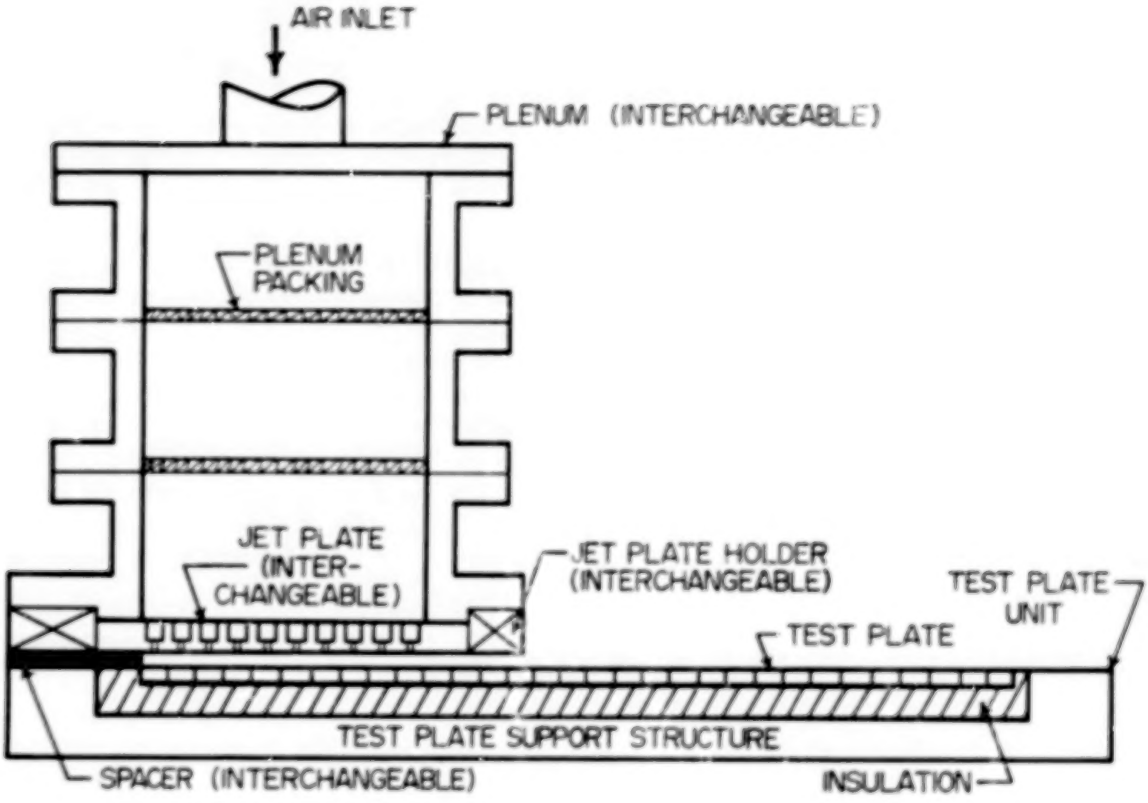

CHORDWISE VIEW

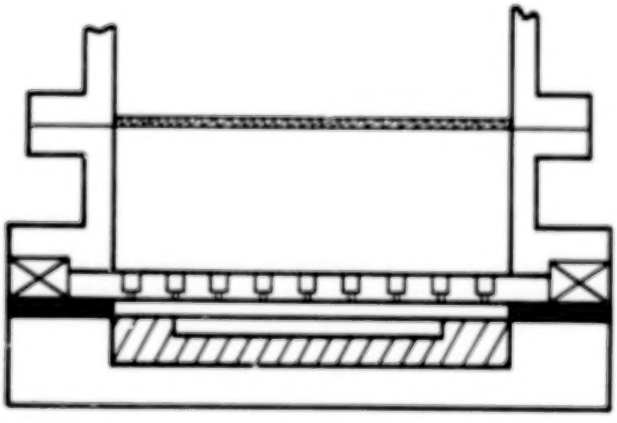

SPANWISE VIEW

Fig. 2.1 Test unit assembly

The significant dimensions and geometric characteristics of the interchangeable plenum/jet plate/spacer configurations for which data is reported are summarized in Table 2.1. Jet plates included in the test program had uniformly spaced jet hole arrays of both inline and staggered patterns. For brevity, specific geometric configurations will be represented throughout this report by notations such as A(10, 6)I, the prefix A indicating an A-size configuration with chordwise hole spacing $x_n/d = 10$, spanwise spacing $y_n/d = 6$, and with inline hole pattern as designated by the suffix I; or A(10, 6, 2)I further indicating a specific channel height, $z/d = 2$. For indicating staggered patterns the suffix S replaces I. Where no distinction as to configuration size or hole pattern is necessary the prefix or suffix is dropped and notations such as (10, 6) or (10, 6, 2) will be utilized. Inline patterns are characterized by jet holes located at the intersection points of a rectangular grid. Each staggered pattern is identical to its inline counterpart, except that alternating spanwise rows were offset by one-half the spanwise spacing. The photographs in Fig. 2.2 show the downstream faces of both the inline and staggered patterns for configuration B(5, 8).

The spanwise width of the heat transfer surface (test plate) was fixed at 12.2 cm (4.8 in.). This dimension permitted symmetrical alignment of the edges of the test plate with respect to the jet hole centerlines for all spanwise hole spacings tested.

The channel width provided always exceeded the test plate width (Fig. 2.1, spanwise view). This permitted the jet hole pattern to extend beyond the edges of the test plate, thus minimizing flow pattern edge effects on the heat transfer characteristics. A single channel width of 18.3 cm (7.2 in.) permitted symmetrical alignment of jet holes with the channel edges for all inline hole patterns, except one. Also, with this channel width the number of holes across the channel span always exceeded the number across the test surface by two or more (Table 2.1). The single exception is C(5, 8)I which required a 16.3 cm (6.4 in.) channel width for symmetrical alignment while providing an excess of one hole across the channel span.

For staggered hole patterns, achievement of symmetry with respect to the channel edges requires special consideration, since alternating spanwise rows are offset one-half of the spanwise hole spacing. To obtain the same total number of holes across the span for each spanwise row would require having one-half a hole at the two channel edges for the offset rows. An alternate approach is to provide one less hole for each alternating offset row, and compensate by setting the channel width at a value midway between that which would provide symmetry for offset rows and that which would provide symmetry for non-offset rows. This is the approach which was adopted here. Appropriate channel widths for the staggered patterns tested are indicated in Table 2.1. However, to minimize the number of spacers which had to be machined, some early tests were conducted using existing standard channel width spacers of 18.3 cm (7.2 in.), as noted in the Table. The effect of this was expected to be minor, which was later verified by a comparison test conducted for configuration C(10, 8, 2)S with the appropriate nonstandard channel width, 17.3 cm (6.8 in.), for this staggered pattern utilized.

Table 2.1 Geometric Characteristics of Configurations Tested

Plenum Size	ℓ cm (inches)	d & b cm (inches)	x_n/d	y_n/d	z/d	① Hole Patterns	② N_s	③ N'_s	④ Channel Width cm (inches)	# of Active Segments	Maximum Chordwise Resolution	Channel Length cm (inches)
A	6.35(2.5)	0.0635(0.025)	10	6	1,2,3,6	I,S	32	48	18.1*(7.125)	5	$2x_n$	10.8(4.25)
				8	1,2,3	I	24	36	--			
B	12.7(5.0)	0.254(0.100)	5	4	1,2,3	I,S	12	18	17.8*(7.00)	10	x_n	17.1(6.75)
				8	1,2,3,6	I,S	6	9	17.3*(6.80)			
		0.127(0.050)	10	4	1,2,3	I,S	24	36	18.0*(7.10)			
				8	1,2,3	I,S	12	18	17.8*(7.00)			
C	25.4(10.0)	0.508(0.200)	5	4	1,2,3	I	6	9	--	20	$\frac{1}{2} x_n$	29.8(11.75)
				6	1,2,3	I	4	6	--			
				8	1,2,3	I,S	3	4	18.3(7.2)			
		0.254(0.100)	10	4	1,2,3	I,S	12	18	17.8*(7.00)			
				6	1,2,3	I	8	12	--			
				8	1,2,3	I,S	6	9	17.3(6.80)			
D	38.1(15.0)	0.762(0.300)	5	4	1,2,3	I	4	6	16.8(6.60)	30	$\frac{1}{3} x_n$	41.3(16.25)
					1,3	S						
		0.381(0.150)	10	4	1,2,3	I	8	12	--			
				8	1,2,3	I	4	6	--			
		0.254(0.100)	15	4	1,2,3	I	12	18	--			
				6	1,2,3	I	8	12	--			
				8	1,2,3	I	6	9	--			

Notes:
① I denotes inline hole pattern, S denotes staggered.
② The number of holes across the test plate span, N_s, varies depending on hole spacing; the number along the chord, $N_c = \ell/x_n$, was fixed at 10 for all tests reported herein.
③ The number of holes across the channel for inline patterns, N'_s, was the same for all 10 spanwise rows for a given jet plate. For staggered patterns, the number of holes across the channel for odd numbered rows (counted from upstream) was N'_s holes while for even numbered rows it was N'_s-1. The single exception is C(5,8)S which had N'_s+1 holes for odd numbered rows and N'_s holes for even numbered rows.
④ The channel width was fixed at 18.3 cm (7.2 in.) for all inline patterns, with the single exception of C(5,8)I which was 16.3 cm (6.4 in.). The channel widths listed in the Table are those appropriate for the staggered patterns. However, for cases marked by an asterisk (*) a standard channel width, 18.3 cm (7.2 in.), was actually used in the tests. See text for further explanation.

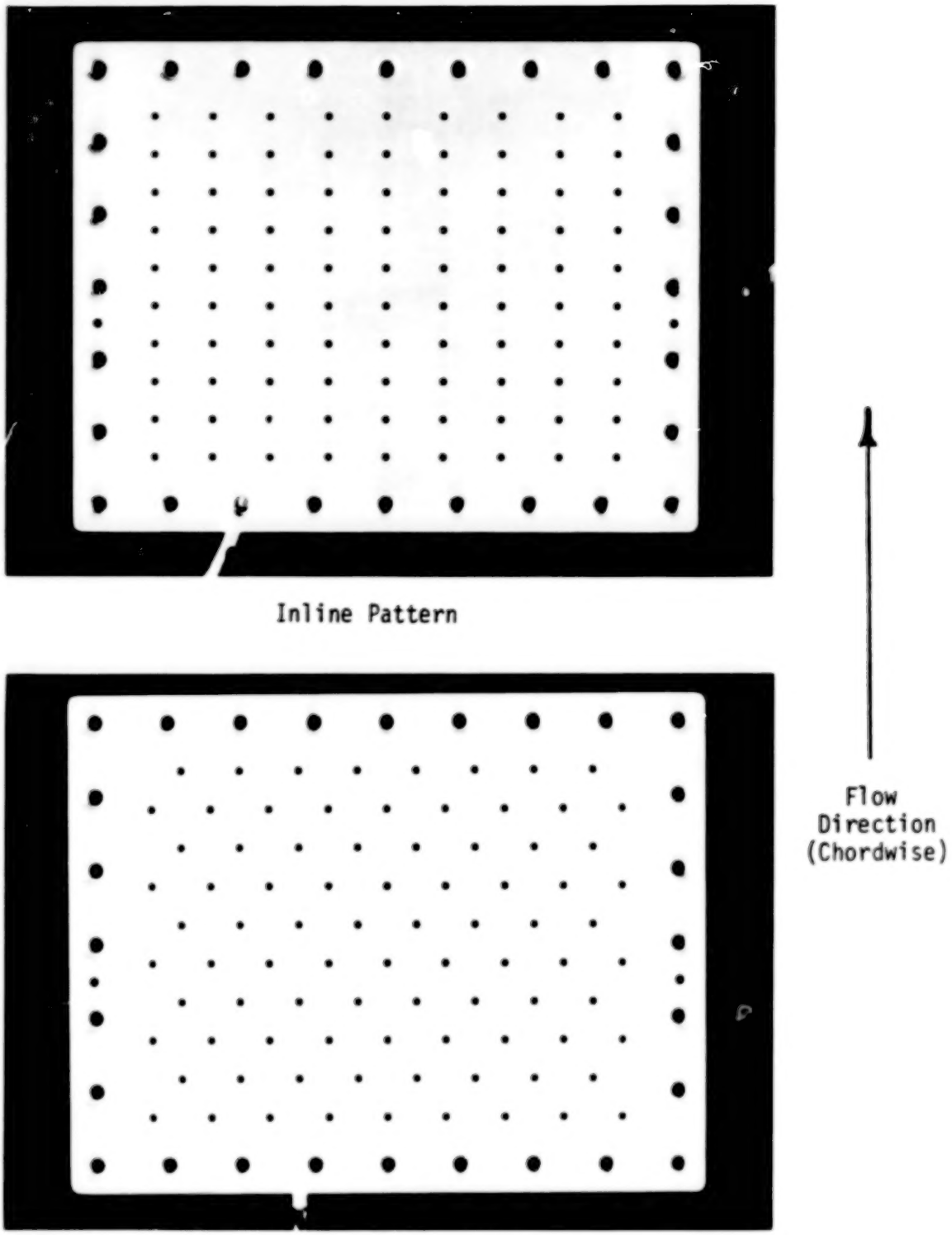

Fig. 2.2 Corresponding inline and staggered jet array hole patterns illustrated for configuration B(5, 8).

The results were consistent with those of the earlier test to within experimental uncertainty.

The number of spanwise rows of holes, equivalent to the ratio of the active heat transfer surface length to the chordwise hole spacing, was fixed at 10 for all tests. Thus, the first configuration listed in the Table, A (10, 6)I, had 480 holes over the channel with 320 over the test surface itself. This was the maximum number of holes in any plate.

The maximum possible chordwise resolution of heat transfer coefficients is also specified in the Table in terms of the chordwise hole spacing. The relationship between the chordwise hole locations and the test plate segments for each plenum size is represented in Fig. 2.3. It may be observed that the jet plates were in every case mounted so that the active heat transfer surface extended a distance $x_n/2$ upstream of the first spanwise row of holes, and the same distance downstream of the tenth (i.e., last) row.

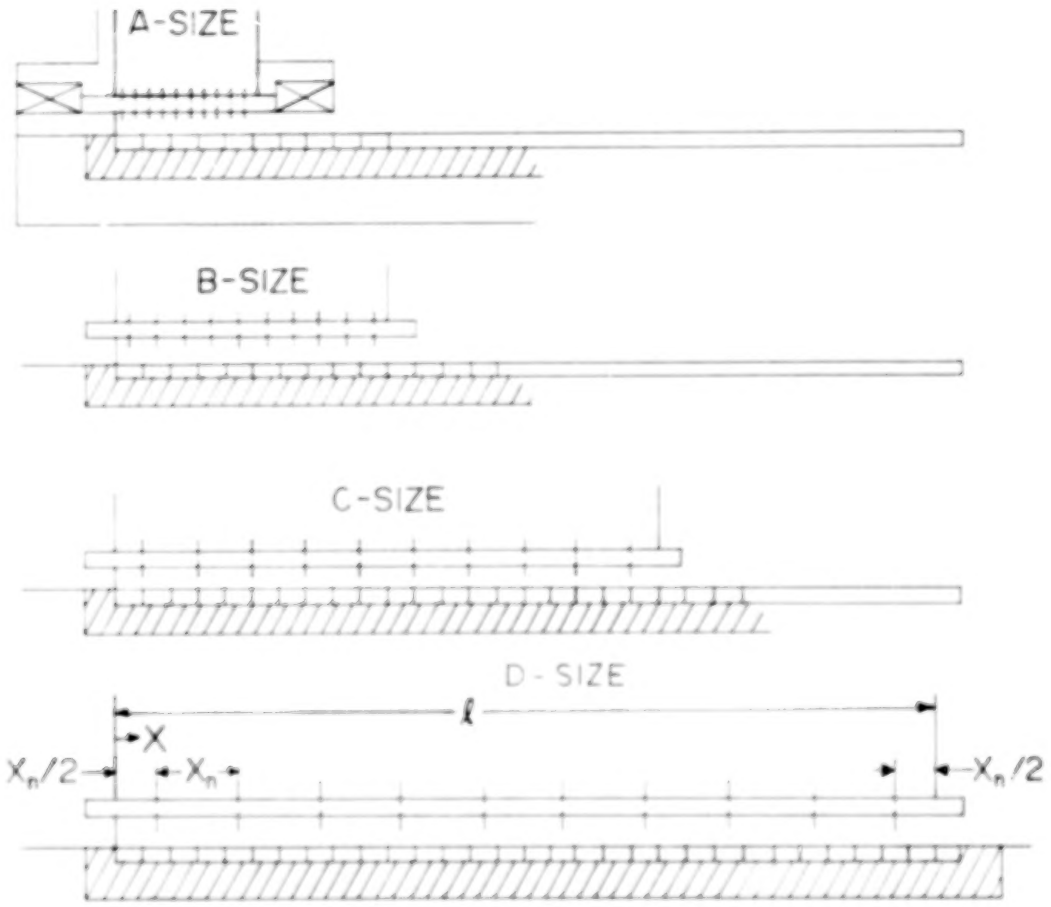

Fig. 2.3 Location of spanwise jet hole rows relative to test plate segments.

A detailed schematic representation of the test plate construction is shown in Fig. 2.4. The copper test plate segments were 0.635 cm (1/4 in.) thick and 1.19 cm (15/32 in.) wide with 0.079 cm (1/32 in.) balsa wood insulation bonded between adjacent segments to minimize heat leak. The segment thickness was selected based on estimates from a one-dimensional heat conduction model, as the smallest value which would still insure an essentially uniform spanwise temperature distribution. This was a compromise with the desire to minimize segment-to-segment heat leak which would decrease continuously with decreasing segment thickness. The individual heaters were foil-type bonded to the underside of each segment, each with power input controlled by a separate variac. The edges and undersides of the segment/heater assemblies were bonded to basswood, selected for the combination of structural and insulating qualities it provided. Those insulation surfaces which would have formed part of the channel and been exposed to the air flow were surfaced with 0.079 cm (1/32 in.) Lexan plastic to provide a smooth aerodynamic surface and prevent possible erosion of the basswood and balsa.

The primary temperature instrumentation in the test plate consisted of copper-constantan thermocouples mounted in the geometric center of each copper segment, with a redundant thermocouple in each segment offset 1.52 cm (0.6 in.) in the spanwise direction. In addition, several segments at intervals along the plate had additional offset thermocouples mounted out to the edge to verify that the spanwise temperature distributions during testing were essentially uniform (Fig. 2.5). Segment number 1 is the upstream segment and has five thermocouples. Segments 5, 10, 20 and 30 each have three, while all remaining segments have two each for a total of 69. Both the heater and the thermocouple leads (not shown in the Figures) were routed vertically downward through the basswood and aluminum base of the test plate unit.

In early tests jet plate temperatures were monitored via thermocouples mounted at four locations spaced over the jet plate, but this practice was discontinued when it was found that these temperature levels did not significantly affect the heat transfer characteristics of interest. The plenum air temperature was monitored with a copper-constantan thermocouple, and plenum pressure with either a manometer or Bourdon gage, via a static pressure tap in the sidewall of the plenum. Air flow rates were determined via a sharp-edged orifice plate located in the flow metering section upstream of the plenum.

Electrical measurements associated with determination of heater power inputs were normally made after conversion to dc by a solid-state signal conditioner. In early tests, however, the ac signal levels were read out on a digital voltmeter and manually recorded. Initially, thermocouple outputs were also manually determined by a hand balance potentiometer, using an ice bath reference junction. Subsequently, both thermocouple outputs and signal levels for determination of heater power outputs were readout via a digital data logger.

Subsequent to the installation of the thermocouples in the individual copper test plate segments, but prior to the permanent bonding of the segments into the test plate unit, the thermocouples were checked for consistency. This was accomplished by placing the segments on a 1.27 cm (1/2 in.) thick aluminum plate. Each segment was clamped tightly to the plate and was also in direct contact with adjacent segments. This assembly was then thoroughly insulated and allowed to stabilize overnight. Utilizing an ice-bath reference junction and a manual-balance potentiometer, each thermocouple potential was then care-

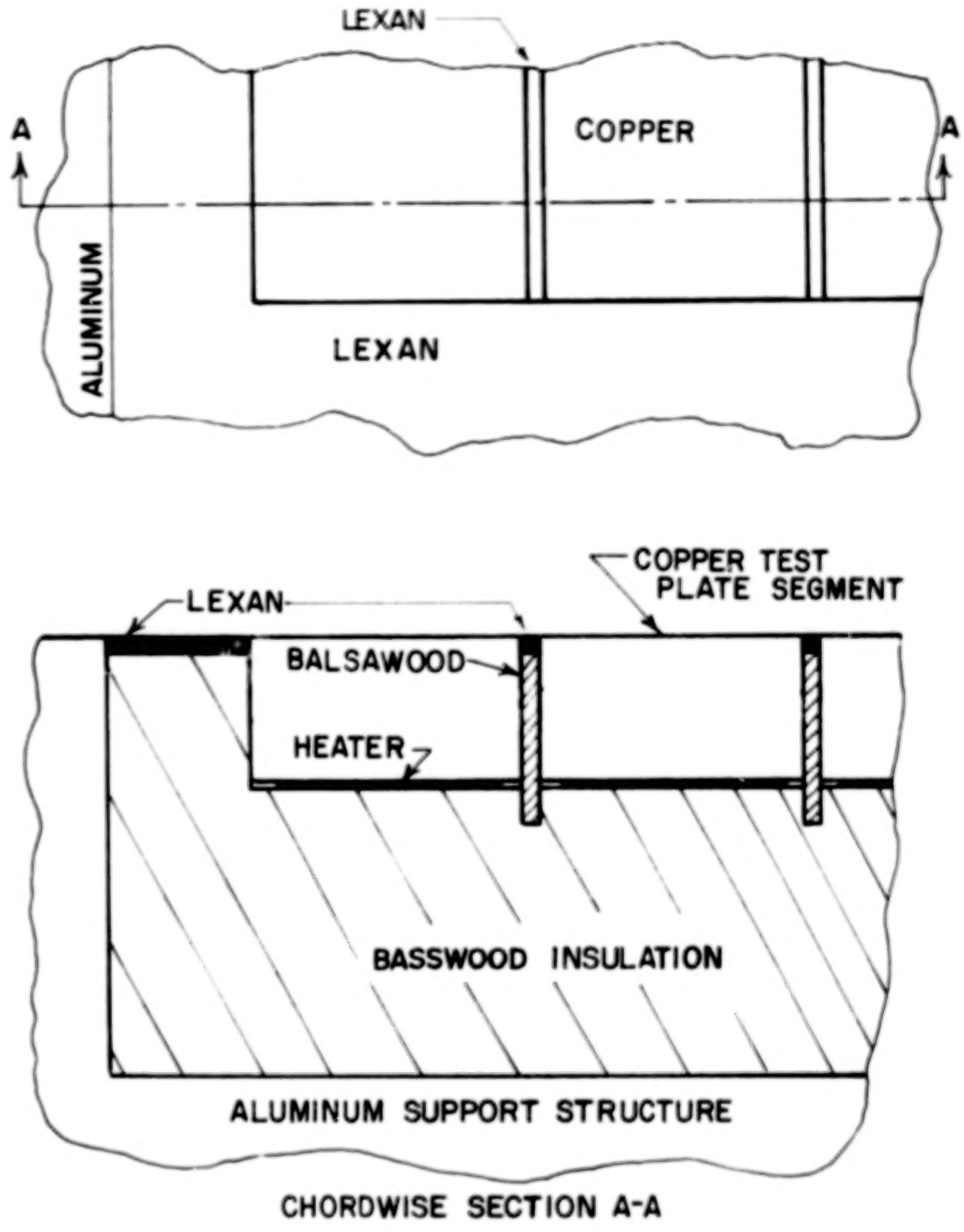

Fig. 2.4 Heat transfer test plate construction details.

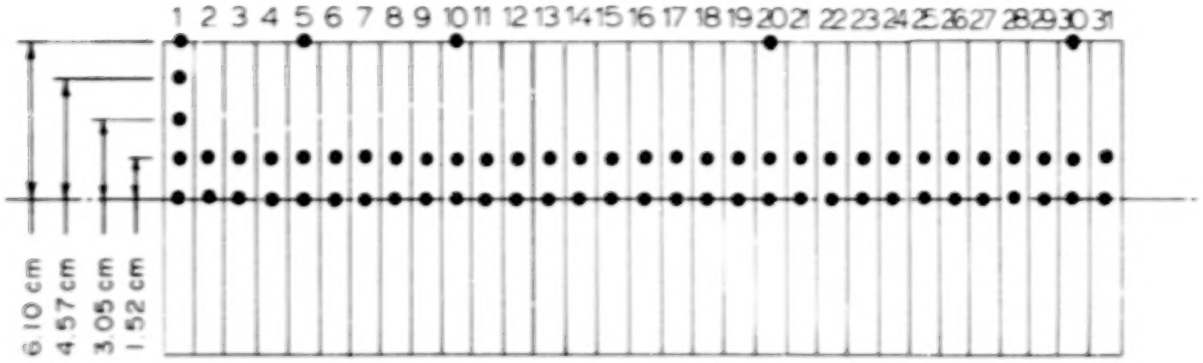

Fig. 2.5 Heat transfer test plate thermocouple locations.

fully checked. The consistency proved to be excellent with a maximum variation of two microvolts (0.05K).

Prior to initiation of any heat transfer tests the pressure uniformity across the upstream (plenum) side of the jet plate was checked utilizing the first jet plate fabricated, A(10,6)I. With the jet plate mounted on the corresponding plenum, flow was established which was permitted to exhaust directly to ambient. The pressure uniformity was checked by inserting a small Pitot tube, in turn, into individual jet holes. The maximum variation observed was 2.6%, with part of this undoubtedly due to small differences in Pitot tube positioning in the holes and uncertainties in manometer readings.

It was thought advisable to qualify each jet plate for jet hole uniformity by checking the flow uniformity while exhausting to a uniform pressure. These flow distribution surveys were made by pressing the squared-off end of a thick-walled soft plastic tube onto the jet plate around individual holes. Flow from the covered jet hole was then routed to a laminar-flow-meter. For jet plates with 0.0635 cm (0.025 in.) hole diameters the maximum single hole flow rate deviation from the mean for the given plate was 13% or less. Ninety-nine percent deviated by less than 10%, while 95% deviated by less than 5%. The only exception was A(10,6)I which had one hole deviating by 24%, with 99% deviating by less than 15%, and 95% deviating by less than 10%. For the 0.127 cm (0.050 in.) hole diameter plates, the largest maximum deviation for any given plate was 12%, while the smallest maximum was 6%. For these plates 99% of the holes deviated by anywhere from less than 4% to less than 8%, depending on the plate. Deviations for 95% of the holes were less than 3%. For plates with hole diameters equal to or greater than 0.254 cm (0.100 in.) the largest maximum deviation was 10%, while all other maximum deviations were less than 5%. Typically, 99% of the holes deviated by less than 2%. The spatial distribution of the nonuniformities in flow rate appeared to be random. The maximum deviation of the mean flow rate over a spanwise row from the mean over all ten spanwise rows was 2.5% or less, including the A(10,6)I plate. On the basis of these qualification tests it appeared that any nonuniformities present would not significantly affect the generality of test results for chordwise resolved, spanwise averaged heat transfer coefficients.

3. EXPERIMENTAL PROCEDURES AND DATA REDUCTION

3.1 Typical Test Runs

A given test run was initially defined by setting up a selected geometric configuration. This entailed attaching a selected jet plate to the corresponding size plenum, which was in turn mounted over the test plate unit with an intervening channel height spacer of selected thickness. Thus, the geometric scale of the configuration was established at a specific jet hole diameter and active heat transfer surface length as well as establishing the spanwise and chordwise hole spacing, hole pattern (inline or staggered), channel height and maximum possible chordwise resolution of heat transfer coefficients.

The setting of a constant mass flow rate to the plenum completed the definition of a typical test run. When steady state was achieved with zero power input to the test plate segment heaters, the segment temperatures were recorded. These temperatures closely approximated the adiabatic wall temperature profile along the test surface. The adiabatic wall condition was not precisely achieved primarily because of small but unavoidable heat leaks. Next, power inputs to segment heaters were individually adjusted to maximum values, under the constraint that the test surface was essentially isothermal. This was accomplished by manual adjustment of the individual variacs which controlled the individual power inputs to the active segment heaters, until the segment centerline thermocouple readings were uniform. Maximum power input was limited, depending on flow conditions, either by temperature limitations of materials in the test plate unit or by current limitations in the switching circuit used for recording the individual power inputs to the heaters. Maximum segment-to-plenum air temperature differences utilized were typically about 30K, with the plenum air temperature in the vicinity of 300K. Finally, the power input was adjusted to nominally half of the maximum value, but again with individual heaters adjusted so as to maintain an essentially isothermal surface. At each power input level, individual segment power inputs and temperatures were recorded. Additional information recorded included the plenum air pressure and temperature, the barometric pressure, the pressure drop across the flow metering orifice, and the orifice upstream pressure and temperature. This completed a heat transfer test run.

The time allowed to insure thermally stable conditions following start-up of the air supply compressors was about two hours. Time intervals required between readings for different power levels at the same flow rate were about 45 minutes. At least one hour was allowed for adjustment to steady state subsequent to the setting of a new flow rate. Thus, under normal conditions, the elapsed run time from compressor start-up to obtain the raw data for a given configuration at a single flow rate was about 3.5 hours; for two flow rates about 6 hours; and for three flow rates about 8.5 hours.

3.2 Segment Heat Transfer Coefficients

Segment heat transfer coefficients were determined based on the defining equation

$$h = (Q/A)/(T_s - T_r) \ . \qquad (3.1)$$

Q is the segment heat rate determined from the measured power input to the segment heater suitably corrected for heat leaks; A is the segment surface area; T_s is the segment surface temperature as determined from the thermocouple imbedded at the center of the copper segment suitably corrected for temperature drop from thermocouple to surface; and T_r is a fluid reference temperature. Details regarding the corrections are discussed in the next section. At the outset it is assumed only that a suitable reference temperature exists, but it is not explicitly defined. With three sets of test plate segment data (Q/A, T_s) available for a given flow condition (corresponding to the zero, maximum and one-half maximum power input levels) one can use any combination of two sets to give two equations of the above form in the two unknowns h and T_r. Since there are three such combinations of the three data sets, one can compute three values of h for a given flow condition. If the assumption that a suitable reference temperature exists for defining the heat transfer coefficient is correct then these three values should be consistent to within experimental uncertainty. The results indeed show that this is the case. Once this was demonstrated, a minimum of just two data sets at two different power levels for a given flow condition would be necessary. However, the experimental procedure above was retained for all test runs to serve as a constant check on the self-consistency and repeatability of the reduced data. For a 95% confidence level the results for segment heat transfer coefficients were typically self-consistent to within about ± 3%, the larger inconsistencies normally occurring for the low Reynolds number cases. Values reported are the mean of the individual values.

The closest possible experimental condition to an adiabatic wall measurement in the present study was for the zero power input condition. Comparison of T_r values computed by combining data sets for maximum and one-half maximum power with segment surface temperatures measured for the corresponding zero power input case showed that these values agree to within 1% of the $(T_s - T_r)$ differences which occurred during the measurements with power inputs. This verifies that T_r may be correctly identified as the adiabatic wall temperature. The segment heat rates which occurred during zero power measurements due to heat leaks were also less than 1% of the heat rates which existed during power input. The ratio $(T_s - T_r)/(T_s - T_0)$, for measurements with power input, ranged from unity to about 4, increasing with increasing flow rate, decreasing channel height, decreasing size of configuration, and increasing distance from the upstream end of the channel. For example, a value of 4 occurred for the configuration B(10, 4, 1) I at the downstream end of the channel for a mean jet Reynolds number of 2.7×10^4. The value at the upstream end was 1.4. Clearly, for the conditions of these tests, the use, in general of plenum temperature as a fluid reference temperature in defining the heat transfer coefficient would not be appropriate. For the gas turbine application, however, conditions are such that, to a good approximation, one may take $(T_s - T_r)/(T_s - T_0) = 1$. Therefore, knowledge of the heat transfer coefficient and plenum temperature is adequate for calculating heat fluxes in the anticipated application of these results.

3.3 Corrections and Experimental Uncertainties

Consider a composite system consisting of a single foil heater and the copper test plate segment to which it is bonded. The lower (rear) surface of the heater and the ends of the copper segment are insulated by the basswood portion of the test plate unit (Figs. 2.1 and 2.4). The sides of the segment interact with the adjacent segments through the thin strips of balsawood (Fig. 2.4). Three types of heat leak paths may be identified; the back loss directly from the heater, the segment-to-segment leak from the sides of the segment, and the leak from the ends of the segment.

For the isothermal test plate condition, the most significant heat leak was that from the foil heaters directly through the back insulation. This was accounted for by a one-dimensional steady state conduction model, applied individually to each section of the test unit associated with an active segment. For heat transfer coefficients resolved to one chordwise hole spacing the effect of the back loss correction ranged from about 1 to 10% depending on flow rate and configuration under test. The effect of back loss for higher resolution heat transfer coefficients was larger for those upstream segments located between spanwise jet hole rows, since these had relatively low heat transfer coefficients. The largest such effect observed (20%) was for those D-size configurations having the larger hole spacings, the smaller channel heights, and at the lowest flow rates ($\overline{Re} = 5 \times 10^3$). When a segment heat transfer coefficient for which this occurred was averaged in with those for its two neighbors, the corresponding effect was reduced to about 10%, for the resulting resolution of one chordwise spacing. Since the back loss depended primarily on the thermal resistance of the back insulation of basswood, the uncertainty in the back loss correction was primarily due to the uncertainty of this resistance. Assigning a conservative uncertainty of ± 15% to this resistance means that the uncertainty in the heat transfer coefficient attributable to heat leak was ± 3% for the most severe condition encountered, and less than ± 1.5% for typical conditions.

During isothermal tests the maximum nonuniformity of segment centerline thermocouple readings over the active portion of the test plate was normally less than 0.25 K, while the difference between adjacent segments was even smaller, normally less than 0.1 K. During zero power tests maximum temperature nonuniformities were about 7 K, with maximum segment-to-segment differences of about 2 K, these occurring for the maximum flow rates at the narrowest channel heights. Segment-to-segment heat leak corrections were entirely insignificant for the isothermal test conditions. For zero power tests these leaks along with the back loss produced a small net heat rate at the segment surface, normally less than 1% of the heat rates for the corresponding test condition with heater power inputs. While the effect of these segment-to-segment leaks was not really significant for the results reported here, they were accounted for in the data reduction routine, so as to provide the generality necessary for handling possible future tests with highly nonuniform thermal boundary conditions.

The total end surface area of each segment was just 10% of the active surface area, and these end surfaces, which formed the lateral edges of the

test plate, were well insulated. Therefore, the edge heat leak was very small. It was neglected in computing the heat transfer coefficients since surface temperatures at the centerline of the test plate were also used in these computations. There is a small dropoff in temperature approaching the ends of the segment, so that the spanwise average surface temperature is slightly below the centerline value. Neglecting this small temperature nonuniformity tends to compensate for the already small effect of neglecting the edge heat leak.

Since radiation accounted for less than 1% of the heat transfer from the test surface, no correction was made for this effect.

The correction of the segment thermocouple readings required to obtain the surface temperatures was made by assuming one-dimensional heat conduction over the 0.32 cm (1/8 in.) thickness of copper between the thermocouple junction and the surface. The magnitude of this correction on the heat transfer coefficients was always less than 2%, and typically less than 1%.

A final effect to be considered arises from the fact that the chordwise thermal boundary condition is not precisely uniform even if the surface of each copper segment has an identical uniform surface temperature distribution across its chordwise width. Adjacent pairs of copper segments are separated by thin strips of lower conductivity material (Lexan/balsawood composite) to minimize the segment-to-segment heat leak (Fig. 2.4). This causes a depression in the surface temperature profile at each Lexan strip location. The maximum possible depression would occur for an adiabatic surface at the strip locations. In this limiting case, the appropriate surface area to use in computing a segment heat transfer coefficient via Eq. (3.1) would be just the surface area of the copper segment itself, over which the surface temperature would be assumed uniform at T_s. This would provide an upper limiting value for h. The corresponding lower limit for h would occur for the assumption of zero temperature depression. In this limit the total heat transfer surface area associated with each segment (copper segment plus strip surface area) would be used in Eq. (3.1).

The isothermal surface was considered as the reference condition, with a correction applied to account for the temperature depression effect. A two-dimensional heat conduction model was applied to determine this correction (Appendix A). According to this model the correction depends on the thickness and thermal conductivity of the strip material, the ratio of strip surface area to copper surface area, the heat transfer coefficient over the corresponding strip surface area. The latter two quantities and their relative magnitude can vary even for a given flow rate and configuration, depending on the chordwise relation of the jet hole centerlines to the segment locations (Fig. 2.3) and the increasing deflection and diffusion of the jets themselves in the downstream direction due to the buildup of the crossflow. Using measured values of heat transfer coefficients in conjunction with the heat conduction model it was concluded that the use in Eq. (3.1) of the arithmetic mean of the copper surface area and the total surface area associated with each segment of the test plate results in an uncertainty in segment heat transfer coefficients due to this effect of ± 2% for 95% confidence (see Appendix A for details).

For the same confidence level, the uncertainty in the segment heater power determination is estimated to be ± 2%. Uncertainties in segment surface temperature values were ± 0.05K, considered on an arbitrary zero point temperature scale since only differences between these temperatures were involved in determination of heat transfer coefficients.

Composite or overall uncertainties may be estimated according to the method of Kline and McClintock [13] for describing uncertainties in single sample experiments. The resulting composite uncertainty for the heat transfer coefficients, including the fact that each segment heat transfer coefficient is determined based on measurements at three different power levels, ranges from ± 3.5% for cases having the smallest back loss correction to ± 5.4% for those having the largest (D-size at maximum resolution). Uncertainties on jet hole diameters are about ± 3% for the smallest hole size to about 1% for the larger sizes. The resulting uncertainties for Nusselt numbers formed using these heat transfer coefficients and the jet hole diameters then range from ± 4.5 to ± 5.5%. Thus, a reasonable single value for the estimated uncertainty associated with the Nusselt numbers tabulated in Appendix B may be taken as ± 5% for a confidence level of 95%.

The mass flow rate uncertainty is about ± 2%, which with the hole diameter uncertainties results in composite uncertainties for jet Reynolds numbers of about ± 3.5%.

3.4 Reproducibility

As already noted in Section 3.2, the consistency of the results for segment heat transfer coefficients within a given test run, with data obtained at three different power input levels, was normally within ± 3%, for a confidence level of 95%. Several test runs repeated after intervals of one week to two months also gave results normally within about 3% for the same confidence level. One early test run for a B-size configuration was repeated about one year later. The mean heat transfer coefficients differed by 2.6%. Eight of the segment values differed between 0.6 and 3%, while the remaining two differed by 4 and 6%.

4. EXPERIMENTAL RESULTS

4.1 Presentation Variables and Parameters

Heat transfer coefficients are presented here primarily in terms of Nusselt numbers based on jet hole diameter (hd/k). However, in examining the effect of hole diameter on the heat transfer coefficients it is more convenient to use a form of Stanton number ($h/\overline{G}^* c_p$). It is emphasized that all Nusselt or Stanton numbers presented are spanwise averaged values; i.e., the experiments were not designed to provide any degree of spatial resolution across the span of the heat transfer surface. Though a major objective of the experiments was to determine chordwise variations of heat transfer coefficients, it must be kept in mind that the chordwise resolution is limited by the width of the individual segments of the test plate (1.27 cm). This represents as much as 20% to as little as 3.33% of the active heat transfer surface length depending on plenum/jet-plate size in use (A, B, C, or D). In terms of chordwise hole spacing, the maximum possible resolution ranges from $2x_n$ for the A-size to $x_n/3$ for the D-size as previously indicated in Table 2.1 and illustrated in Fig. 2.3. Data from any size configuration can, of course, be averaged over as many segments as desired.

It is convenient to categorize the Nusselt number data as follows. (1) mean values, $\overline{Nu}$, averaged over the entire active heat transfer surface; (2) low-resolution values averaged over x_n or $2x_n$, (3) higher-resolution values averaged over $x_n/3$ or $x_n/2$. As will be seen the higher-resolution results show significant periodic variations of heat transfer coefficients superimposed on the overall chordwise trend, while the low-resolution results show more clearly the overall chordwise trend smoothed across the periodic variations. Both the low and higher-resolution Nusselt numbers are denoted by Nu. Chordwise Nusselt number profiles are illustrated by plotting resolved Nusselt numbers against the streamwise coordinate normalized by the chordwise hole spacing, x/x_n. The spacing of the data points along the abscissa directly reflects the chordwise resolution involved. In these plots vertical arrows along the abscissa are used to directly indicate the spanwise jet hole row locations.

A mean Reynolds number based on jet hole diameter is utilized as the flow parameter. Two definitions of Reynolds number are employed. One is the mean jet Reynolds number, $\overline{Re}$, based on the mass velocity at the jet holes, $\overline{G}$, while the second, $\overline{Re}^*$, 's based on the mass flow rate per unit heat transfer surface area, $\overline{G}^*$. These are related simply thru the ratio of the open or flow area of the jet plate to the opposing heat transfer surface area; i.e.,

$$\overline{Re}^* = Re \cdot A^*_o$$

For the present jet plate design configurations,

$$A^*_o = \frac{\pi}{4} \frac{1}{(x_n/d)\ (y_n/d)}$$

It is well to keep in mind that heat transfer coefficients compared for the same $\overline{G}$ reflect the relative magnitude for comparable pressure drop across the jet plate, while those compared for the same $\overline{G}^*$ reflect the relative magnitude for the same mass flow per unit heat transfer surface area.

In forming the individual segment Nusselt numbers, the thermal conductivity was evaluated at the arithmetic mean of the segment surface temperature and the corresponding fluid reference temperature, T_r. The dynamic viscosity used in forming the mean Reynolds number was evaluated at the arithmetic mean of the isothermal surface temperature and T_r averaged over the length of the heat transfer surface. The temperature dependence of the viscosity and thermal conductivity was based on the following formulas:

$$\mu = \mu_{ref} (T/T_{ref})^{\alpha}$$

where $\mu_{ref} = 1.85 \times 10^{-5}$ (N·s)/m^2, $\alpha = 0.762$, and $T_{ref} = 300$ K,

and

$$k = k_{ref} (T/T_{ref})^{\beta}$$

where $k_{ref} = 0.0261$ W/(m·K), $\beta = 0.844$, and $T_{ref} = 300$ K.

These formulas were determined by least squares fits to the data for air from the TPRC Data Series [14] over the limited range 280 to 340 K which covers the range of the present experiments. Over this range the maximum deviation of any TPRC recommended data point from these formulas is 0.1%.

The heat transfer data for each configuration was normally obtained for several flow rates corresponding to certain nominal jet Reynolds numbers. However, it was not convenient to attempt to preset flow rates for different configurations so as to achieve precisely identical sets of Reynolds numbers. In order to permit comparisons of Nusselt numbers for fixed or selected Reynolds numbers, interpolation formulas based on least squares power function curve fits were developed in the form

$$Nu = C \overline{Re}^n \qquad (4.1)$$

for both Nu and $\overline{Nu}$. The fitting constants C and n were determined individually for each Nu and $\overline{Nu}$ of each configuration. In what follows all figures presenting results for fixed or selected Reynolds numbers are based on the use of the above interpolation formula.

In order to assess the confidence which may be placed in such interpolated data points, the percentage deviation of each measured Nusselt number from its respective fit line was calculated (excepting those few configurations for which only two flow rates were run). The results are summarized in

Table 4.1. They indicate that the confidence which may be placed in interpolated data points appearing in the figures which follow is essentially as good as that for directly measured points.

Table 4.1 Deviations of Measured Nusselt Numbers from Individual Configuration Least Squares Curve Fits

Confidence Level	Maximum Absolute Deviation	
	$\overline{Nu}$†	Nu††
95%	2.5%	3%
99%	3%	4%
100%	4%	9%

† Total number of points, 219.

†† Resolved to $2x_n$ for A-size, x_n for B, C, and D-sizes. Total number of points, 2025.

4.2 Documentation of Data Base

A complete tabulation of both mean and chordwise resolved Nusselt numbers resulting from the test runs conducted for all configurations listed in Table 2.1 is presented in Appendix B. The Nusselt number values are tabulated as a function of the mean jet Reynolds numbers. The chordwise resolved Nusselt numbers are tabulated for the maximum possible resolution as limited by the chordwise dimension of the test plate segments and are referred to as segment Nusselt numbers. The plenum temperature, plenum pressure, and exhaust-to-plenum pressure ratio are also listed for each case.

A word of caution should be noted in connection with the use of the segment Nusselt numbers for the C-size configurations. Here the chordwise resolution is $x_n/2$, with two test plate segments per spanwise hole row (Fig. 2.3). Upstream, where the jet deflection due to crossflow is minimal, the jet impingement points are essentially directly opposite the holes. Because of the resulting symmetry, with precisely two segments per row, periodic variations in the Nusselt numbers, though present, are not detected upstream, even though the resolution is better than one chordwise hole spacing.

In examining or utilizing any of the segment Nusselt number results tabulated in Appendix B, the reader is urged to keep in mind the location of the jet hole rows relative to the test plate segments (Fig. 2.3).

4.3 Geometrically Similar Configurations

In this section both mean Nusselt numbers and chordwise Nusselt number profiles for geometrically similar configurations of different sizes are compared in graphical form. Then the results of a statistical analysis based on the deviations of the data points from least squares fit lines through the various sets of data points for geometrically similar configurations is presented.

4.3.1 Mean Nusselt Numbers

The sets of geometrically similar configurations for which tests were run are summarized in Table 4.2. Mean Nusselt numbers for the two sets which include A-size results are plotted in Fig. 4.1. The A and C size results for the (10, 6) I configuration coincide overall to well within experimental uncertainty. At $z/d = 3$, $\overline{Re} \simeq 2 \times 10^4$ the A and C points differ more noticeably, with the A point falling about 10% below the C point. This difference is still at the margin of the estimated uncertainty band. However, the available channel pressure traverse data indicates that the pressure ratios for this case result in choked flow across the downstream hole rows for the A-size, but not for the C-size.

For the (10, 8)I configuration, test results were obtained for all four sizes. Examination of the mean Nusselt numbers (Fig. 4.1) shows that while they are fairly coincident overall, differences exist which appear to exceed experimental uncertainties. In general, the B, C, and D results are more consistent with each other than they are with the A results. Parallel straight lines (not shown) superposed on the $z/d = 1$ plot would encompass all the B, C, and D data points with a total interval of about 8%. For $z/d = 2$, the interval would be 12%, and for $z/d = 3$, 9% with the exception of the B data point at $\overline{Re} \simeq 5 \times 10^4$. These intervals are within or at the margin of the estimated overall uncertainty of $\pm$ 5%. The excepted B data point falls about 10% below the interval. For this size at the large $\overline{Re}$, the flow was choked across all holes. All of the A points fall slightly outside of the bands indicated above.

For the (5, 4)I and (10, 4)I configurations, results were obtained for sizes B, C, and D. Mean Nusselt numbers for these cases are displayed as a function of $\overline{Re}$ in Fig. 4.2. Here parallel straight lines, enclosing the data points for each individual z/d, require an interval of 10% or less.

Finally, mean Nusselt numbers for those configurations for which data was obtained for the B and C sizes only are plotted in Figs. 4.3 and 4.4. Here Nusselt number intervals of 7% or less encompass all the data points for each z/d, with the exception of one point. This point is for the B(5, 8)I configuration, $z/d = 3$, at $\overline{Re} \simeq 5 \times 10^4$. Pressure traverse results indicate that for this condition the flow was nearly choked across the first eight spanwise rows of holes and was choked across rows 9 and 10. However, to include this point

still only requires an overall interval of 11%. It may also be noted that this point falls only 7.5% below a straight line extrapolation of the four lower Reynolds number points for this configuration.

The magnitudes of these mean values, to the extent that they can be directly compared, given differences in values and combinations of geometric parameters, are consistent with several recently published results for configurations of similar types [6, 8]. Further discussion of these results will be delayed until after the low-resolution chordwise Nusselt number profiles for some of the geometrically similar configurations have been examined.

Table 4.2 Summary of Geometrically Similar Configurations for Which Tests Were Run

$(x_n/d, y_n/d)$ HOLE PATTERN	z/d	Plenum/Jet Plate Sizes	d(cm) Smallest Size	Maximum Length Scale Factor
(5, 4)I	1, 2, 3	B, C, D	0.254	3
(5, 8)I	1, 2, 3	B, C	0.254	2
(10, 4)I	1, 2, 3	B, C, D	0.127	3
(10, 6)I	1, 2, 3	A, C	0.0635	4
(10, 8)I	1, 2, 3	A, B, C, D	0.0635	6
(5, 4)S	1, 3	B, D	0.254	3
(5, 8)S	1, 2, 3	B, C	0.254	2
(10, 4)S	1, 2, 3	B, C	0.127	2
(10, 8)S	1, 2, 3	B, C	0.127	2

4.3.2 Low Resolution Nusselt Number Profiles

Low resolution chordwise profiles of Nu, resolved to $2x_n$, are plotted in Fig. 4.5 for the same cases shown in Fig. 4.1, with $\overline{Re}$ as a parameter in each plot. The Figure is again arranged to directly compare results for geometrically similar configurations of different sizes. Results are compared up to the largest nominal $\overline{Re}$ (2×10^4) for which data was obtained for the A and C sizes included in the comparison. The corresponding values of $\overline{Nu}$ are shown at the right hand side of each graph. In these and subsequent similar graphs, the spanwise jet hole row locations relative to the heat transfer surface are indicated by the vertical arrows. Similar to the mean Nusselt numbers, the chordwise profiles are fairly coincident for the different sizes with the same geometric configuration, yet differences exist which exceed experimental uncertainties. The comparisons for A(10, 6)I and C(10, 6)I at z/d = 1 show that the chordwise profiles differ somewhat, but in such a way that the mean values are essentially coincident. The same trend is detectable for z/d = 2, but is less pronounced. However, for z/d = 3 at $\overline{Re}$ = 2×10^4 significant differences in both Nu and $\overline{Nu}$ are apparent. Recall that

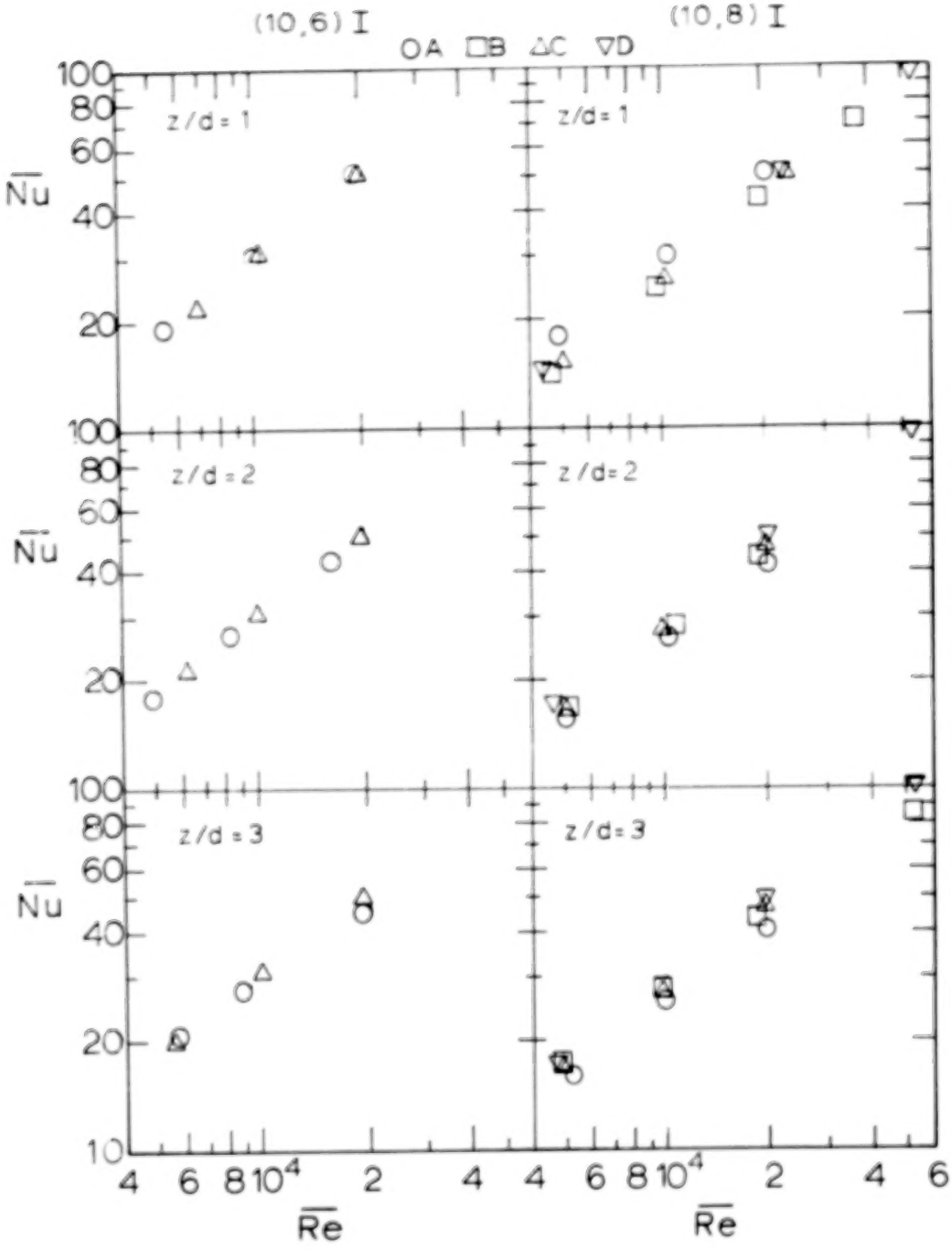

Fig. 4.1 Comparison of mean Nusselt numbers for geometrically similar inline configurations which include A-size results.

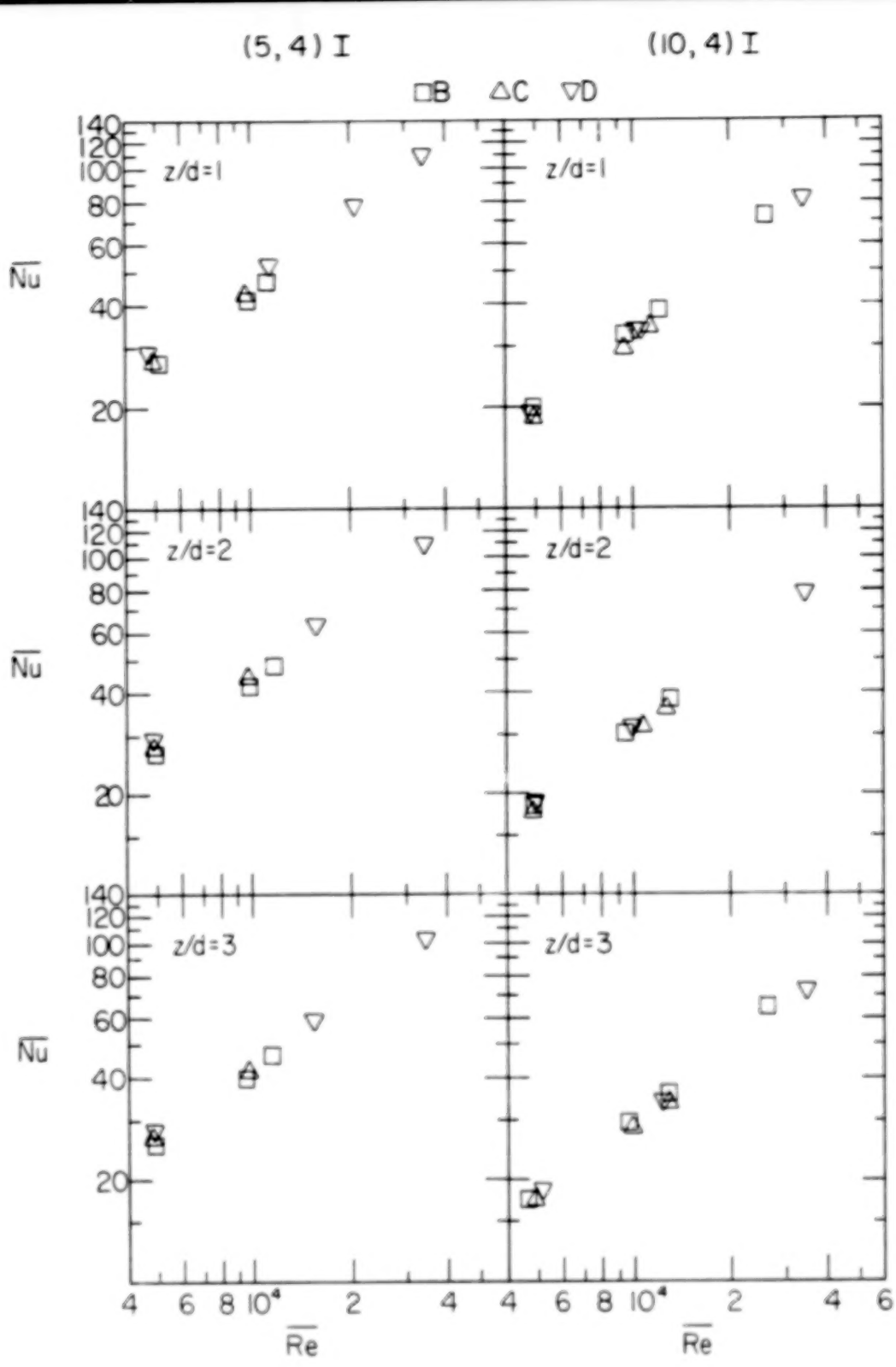

Fig. 4.2 Comparison of mean Nusselt numbers for geometrically similar inline configurations of B, C, and D-sizes.

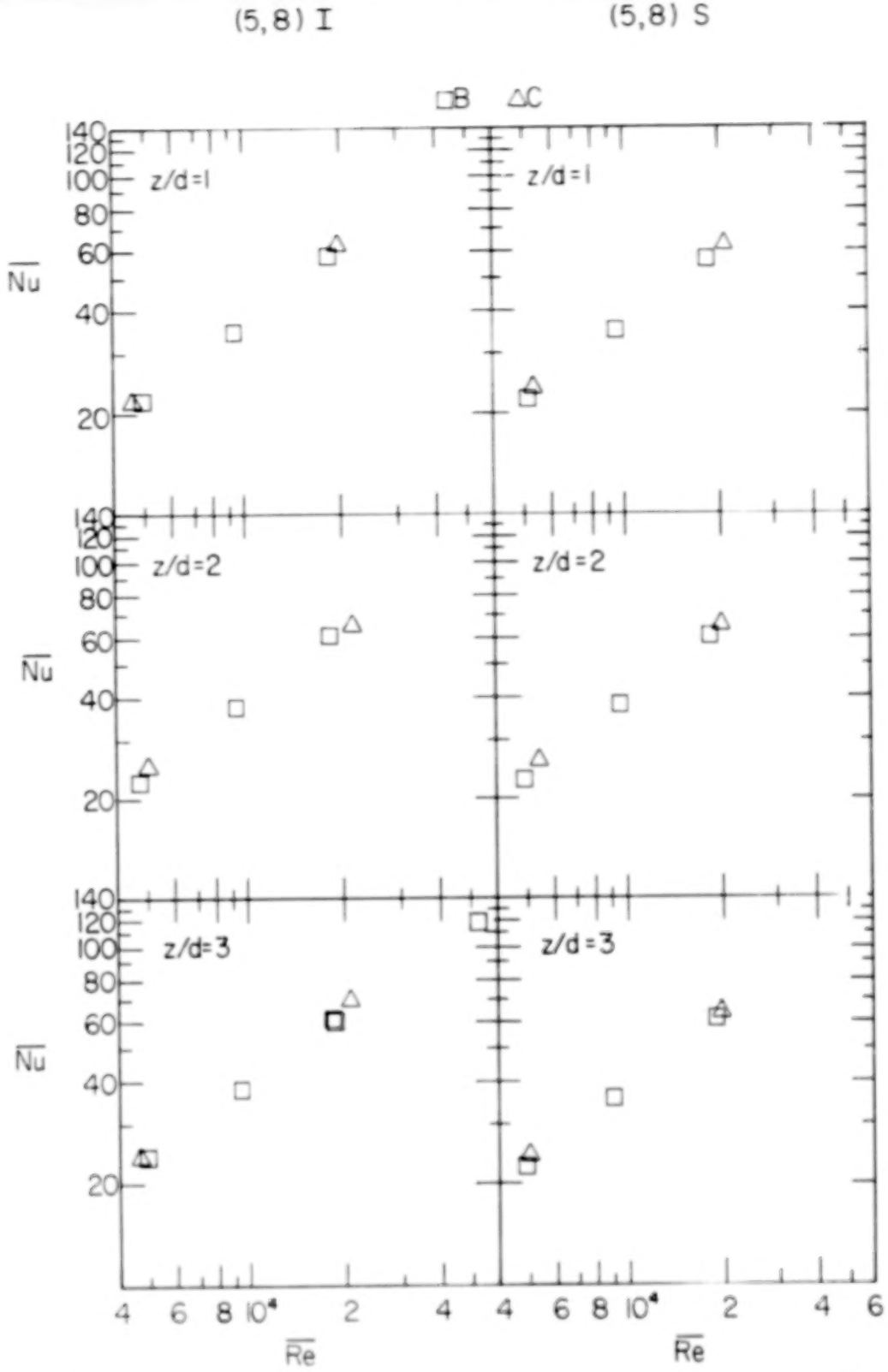

Fig. 4.3 Comparison of mean Nusselt numbers for geometrically similar inline and staggered configurations of B and C sizes.

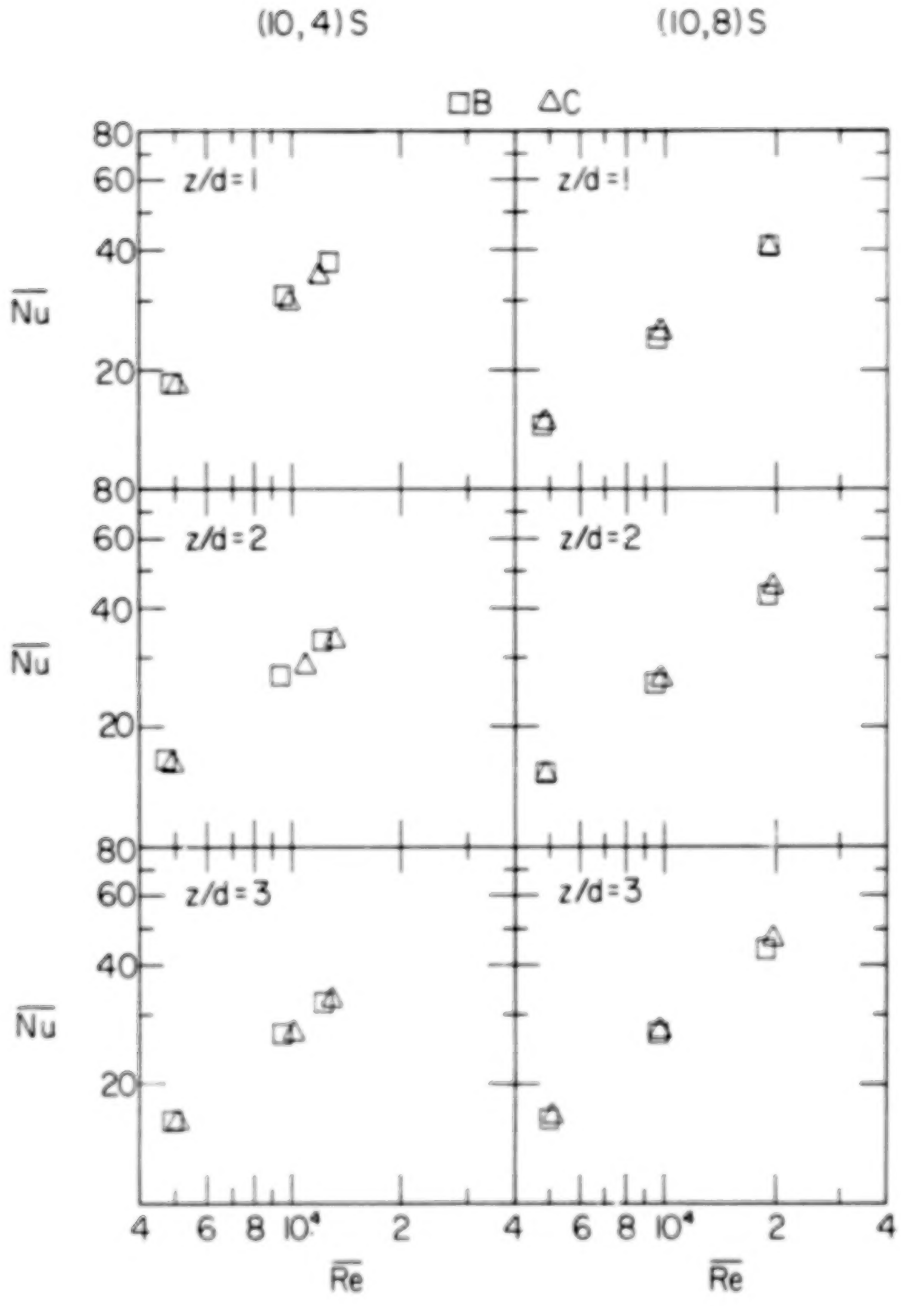

Fig. 4.4 Comparison of mean Nusselt numbers for geometrically similar staggered configurations of B and C-sizes.

in this case the flow was choked across the downstream rows for the A-size but not for the C-size. For the (10, 8)I configuration the chordwise profiles for the B, C, and D sizes are, overall, more consistent with each other than with the A size results, as in the case of the mean values. On the whole the overall spread of the B, C, and D - size data for this $\overline{Re}$ range is substantially within or on the margin of estimated experimental uncertainty while some of the A-size data falls outside that range.

Chordwise profiles resolved to x_n are shown in Fig. 4.6 for geometrically similar B and D size configurations for which data was obtained at higher jet Reynolds numbers. The profiles are shown for the highest nominal Reynolds number values within the range covered by the available data. For (10, 8, 3)I at $\overline{Re} = 5 \times 10^4$ the B-size data falls consistently below the D-size, the difference increasing in the downstream direction. It is noted that, unlike the conditions for this configuration in B-size at lower $\overline{Re}$ (Fig. 4.5), the flow was apparently choked across all the holes for B-size at $\overline{Re} = 5 \times 10^4$, but not for the D-size. This is similar to the occurrence previously noted for A-size configuration, but at a lower $\overline{Re}$. For the (10, 8, 1)I case at $Re = 3.5 \times 10^4$ the consistency is quite good. In this case the flow was not choked across the holes for either B or D-size.

4.3.3 Statistical Analysis

In order to assess in detail the degree of consistency of the results obtained for geometrically similar configurations a statistical study of all the data obtained for such cases was performed. Least square fits in the form of Eq. (4.1) were carried out for the combined data of the several sizes for each set of geometrically similar configurations (Table 4.2). Both mean and resolved Nusselt numbers as a function of mean jet Reynolds number were treated; and percent deviations of the Nusselt number data points from the fit line were computed. This was followed by determination of the deviations, without regard to sign, which encompassed 95, 99, and 100% of the data points; i.e., resulted in confidence levels of 95, 99, and 100%. The results for the two configurations which included A-size data are summarized in Table 4.3; and reflect the prior observation that the B, C, and D size results are more consistent with each other than with the A-size results.

It has been noted several times that observed differences in Nusselt numbers for the smaller sizes at the larger channel heights and highest Reynolds numbers are associated with pressure ratios across the holes which indicate the flow is choked. Thus, a possible explanation of these differences is compressibility effects. Choking across holes is more likely to occur for larger channel heights where most of the total pressure drop from plenum to exhaust occurs across the holes rather than along the channel. For the smallest channel height the exhaust-to-plenum pressure ratios for the larger Reynolds numbers also become less than the critical value; but the flow is not choked across the holes since a much larger fraction of the total pressure drop occurs along the channel. However, in some cases the crossflow itself is choked; thus, compressibility effects may also be significant for the smaller sizes at the smallest channel height. All of these effects appear with the low laboratory pressure levels and the resulting relatively large pressure drops

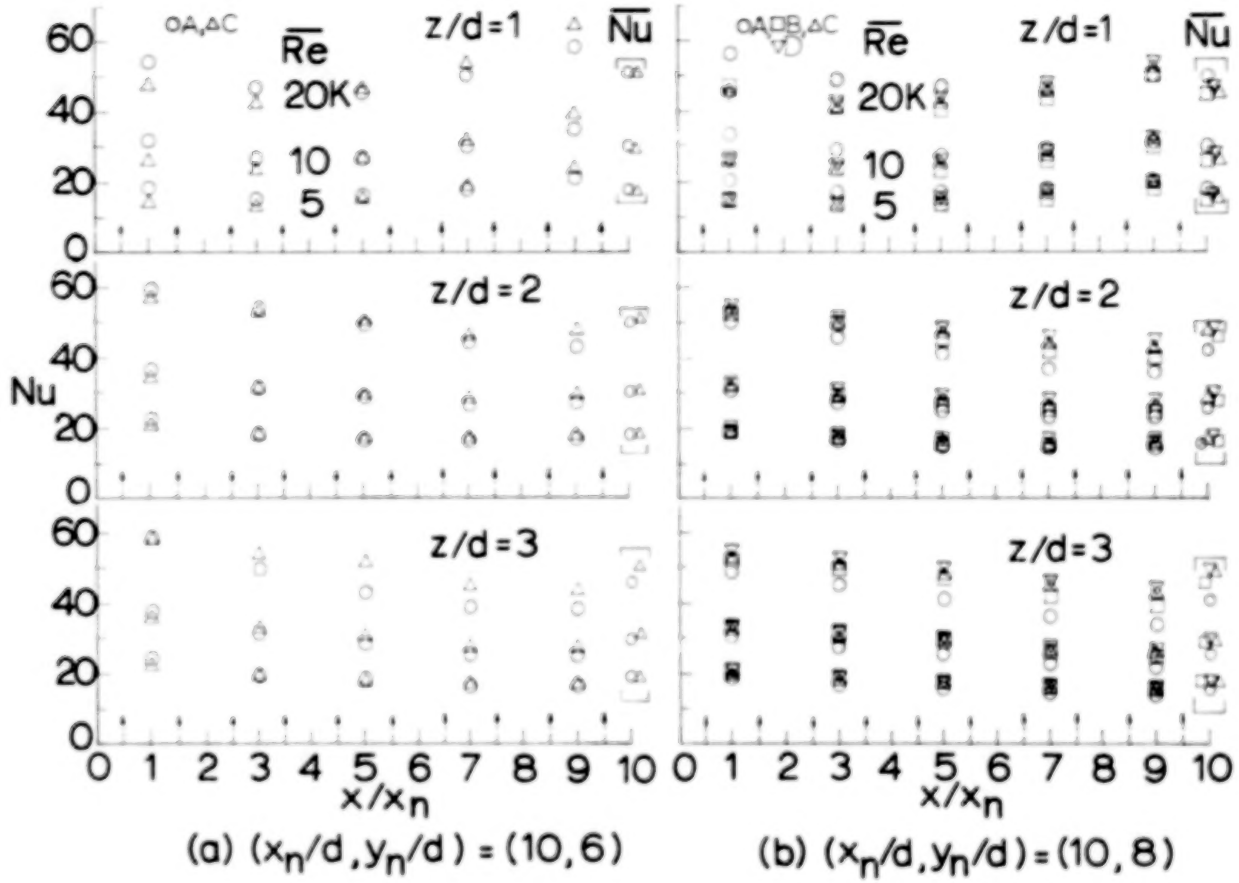

Fig. 4.5 Comparison of low-resolution chordwise Nusselt number profiles for geometrically similar inline configurations which include A-size results.

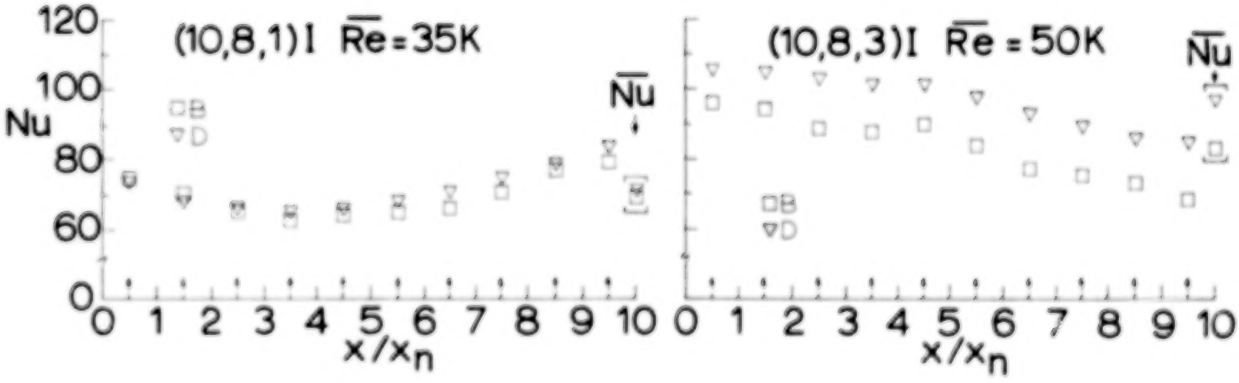

Fig. 4.6 Comparison of low-resolution chordwise Nusselt number profiles for geometrically similar inline configurations at high Reynolds numbers.

required to achieve the larger jet Reynolds numbers with the smaller jet diameters. The pressure levels in the anticipated turbine application are much higher, with correspondingly lower Mach numbers. Therefore, it is reasoned that the present data obtained with sizes larger than A-size best models the prototype heat transfer characteristics for the gas turbine engine application.

However, it should also be noted that an apparently significant effect occurs for the A-size data at smaller Reynolds numbers, particularly at z/d = 1 (Fig. 4.5), which cannot be attributed to compressibility effects. The possibility exists that an effect similar to that reported by Gardon and Akfirat [15] may be, in some measure, a contributing factor. They reported the detection of a slot width dependence for slot jet stagnation point heat transfer at slot width-to-spacing ratios less than eight, which was attributed to turbulence effects.

Table 4.3 Maximum Deviations of Mean and Resolved Nusselt Numbers from Least Squares Fits to Combined Data of Geometrically Similar Configurations

$(x_n/d, y_n/d)$ Hole Pattern	z/d	Sizes Included in Fits	Nusselt Number (Mean or Resolved)	Maximum Absolute Percent Deviation for Confidence Level of			Total Number of Points Involved
				95%	99%	100%	
(10, 8)I	1, 2, 3	A, B, C, D	$\overline{Nu}$	11	14	14	38
			$Nu(2x_n)$	14	19	26	190
		B, C, D	$\overline{Nu}$	8	9	9	29
			$Nu(2x_n)$	9	10	11	145
(10, 6)I	1, 2, 3	A, C	$\overline{Nu}$	5	5	5	18
			$Nu(2x_n)$	9	13	14	90
		C	$\overline{Nu}$	1	1	1	9
			$Nu(2x_n)$	2	3	3	45

Despite these A-size observations, the results are quite encouraging from the standpoint of utilizing the data for design purposes. For a 95% confidence level the maximum absolute deviation of $\overline{Nu}$ from the best fit lines for the (10, 6)I configuration, which includes both A and C-sizes, is 5%, while for Nu it is 9% (Table 4.3). The corresponding deviations for configuration (10, 8)I which includes data for all four sizes are 11% for $\overline{Nu}$ and 14% for Nu. In addition, if this (10, 8)I data is analyzed as it was for Table 4.3, but classified according to channel height (Table 4.4) it appears that excluding z/d = 1 results in maximum absolute deviations from the best fit line for a full 100% confidence level of 12% for $\overline{Nu}$ and 16% for Nu even with A-size data included in the fit.

Table 4.4 Maximum Deviations of Mean and Resolved Nusselt Numbers from Least Squares Fits to Combined Data for Configuration (10, 8)I for Individual Channel Heights.

Sizes Included in Fits	z/d	Nusselt Number (Mean or Resolved)	Maximum Absolute Percent Deviation for Confidence Level of			Total Number of Points Involved
			95%	99%	100%	
A, B, C, D	1	$\overline{Nu}$	14	14	14	13
		$Nu(2x_n)$	18	26	26	65
	2	$\overline{Nu}$	11	11	11	12
		$Nu(2x_n)$	13	14	14	60
	3	$\overline{Nu}$	12	12	12	13
		$Nu(2x_n)$	12	16	16	65
B, C, D	1	$\overline{Nu}$	6	6	6	10
		$Nu(2x_n)$	8	9	9	50
	2	$\overline{Nu}$	8	8	8	9
		$Nu(2x_n)$	9	10	10	45
	3	$\overline{Nu}$	9	9	9	10
		$Nu(2x_n)$	11	11	11	50

A final statistical summary covering all remaining geometrically similar cases (A-size data was not obtained for these cases) is given in Table 4.5. These results are again quite satisfactory, indicating that for a 95% confidence level the maximum absolute deviation from the best fit lines through data sets for geometrically similar cases was 7% for both $\overline{Nu}$ and Nu.

Table 4.5 Maximum Deviations of Mean and Resolved Nusselt Numbers from Least Squares Fits to Combined Data of Geometrically Similar Configurations not Included in Table 4.3

$(x_n/d, y_n/d)$ PATTERN	z/d	Sizes Included in Fits	Nusselt Number (Mean or Resolved)	Maximum Absolute Percent Deviation for Confidence Level of			Total Number of Points Involved
				95%	99%	100%	
(5, 4)I	1, 2, 3	B, C, D	$\overline{Nu}$	7	8	12	167
(5, 8)I	1, 2, 3	B, C					
(10, 4)I	1, 2, 3	B, C, D					
(5, 4)S	1, 3	B, D	$Nu(x_n)$	7	10	14	1670
(5, 8)S	1, 2, 3	B, C					
(10, 4)S	1, 2, 3	B, C					
(10, 8)S	1, 2, 3	B, C					

4.4 Low Resolution Heat Transfer Characteristics

4.4.1 Effect of Channel Height

Reference to Figs. 4.5 and 4.6, previously presented, indicates that Nusselt numbers for z/d = 1 first decrease, then increase as one proceeds downstream. For the larger channel heights the Nusselt numbers essentially decrease monotonically. This behavior occurs irrespective of the magnitude of $\overline{Re}$. The effect of channel height on heat transfer coefficients for otherwise fixed geometry (x_n, y_n, d, ℓ and hole pattern) and fixed flow rate can be visualized directly in each of the four graphs of Fig. 4.7 drawn from the B-size data. Each graph is for a different set $(x_n/d, y_n/d)$, at $\overline{Re} = 10^4$. The differences in the profiles are in every case greater between z/d = 1 and 2, than between z/d = 2 and 3, the effect being most pronounced for the closest spanwise spacing, $y_n/d = 4$, shown in the two graphs at the top of the Figure.

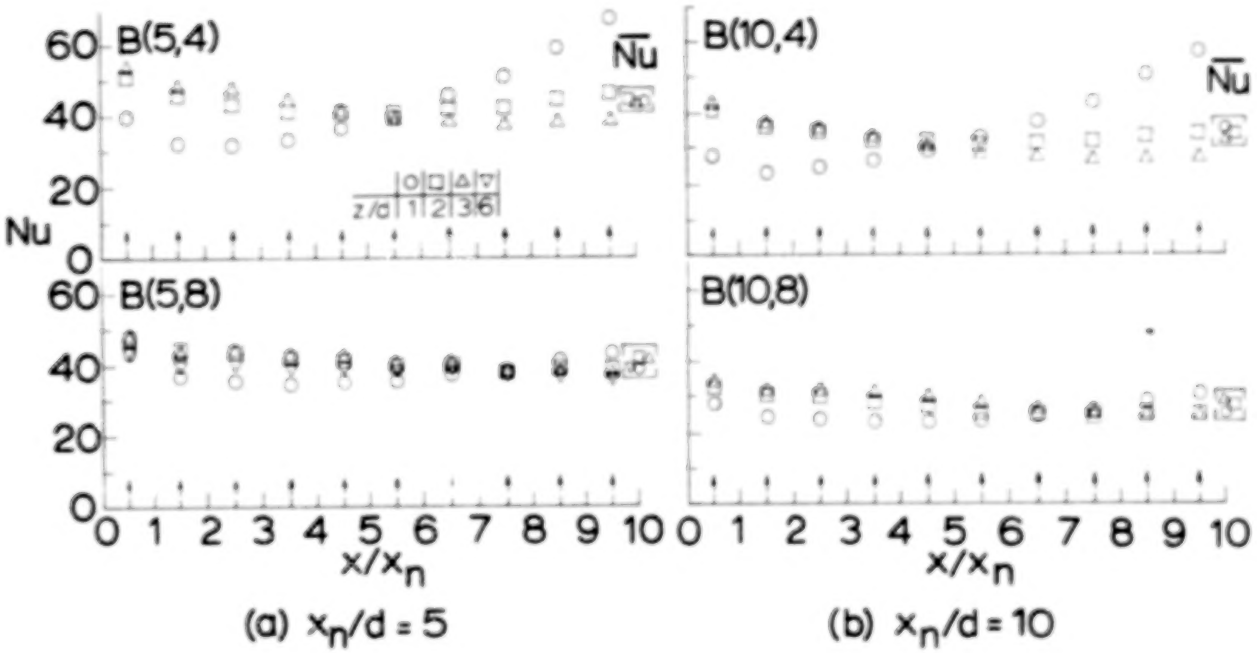

Fig. 4.7 Effect of channel height on low-resolution chordwise Nusselt number profiles and mean values - inline hole pattern, $\overline{Re} = 10^4$.

The lower left hand graph includes results for z/d = 6 which differ only slightly from the results for z/d = 2 and 3. These graphs show clearly that although the chordwise profiles of heat transfer coefficients can vary significantly with channel height, especially with close spanwise spacings, the mean values remain relatively insensitive to channel height over the range covered. Note that over the range $1 \leq z/d \leq 3$, for all (x_n/d, y_n/d) shown, the upstream cooling rate is higher for the larger z/d, but the difference decreases until at some point downstream all z/d result in the same cooling rate, while further downstream the smaller values of z/d give the higher cooling rates. These effects are undoubtedly related, at least in part, to the fact that for this range of z/d jet impingement cooling with minimal crossflow, which is the upstream condition, increases with channel height, while cooling rates due to channel-type flows, which here arise downstream as a crossflow, typically vary inversely with channel height.

4.4.2 Effect of Hole Diameter

The effect of hole diameter is examined under the condition that other geometric parameters (x_n, y_n, z, & and hole pattern) as well as the mean flow rate per unit heat transfer surface area ($\overline{G}^*$) are held fixed. This may be accomplished in dimensionless form utilizing a Stanton number defined as $h/\overline{G}^* c_p$ rather than a Nusselt number. The effect of reducing the hole diameter by one-half is shown in Fig. 4.8, by comparing results for configuration B(5, 4, 1) with those for B(10, 8, 2) at the same value of $\overline{G}^*$. The comparison is made for both the inline and staggered hole patterns. For both cases, cutting the diameter in half roughly triples the upstream heat transfer coefficients, while downstream the increase is much smaller. The mean heat transfer coefficient

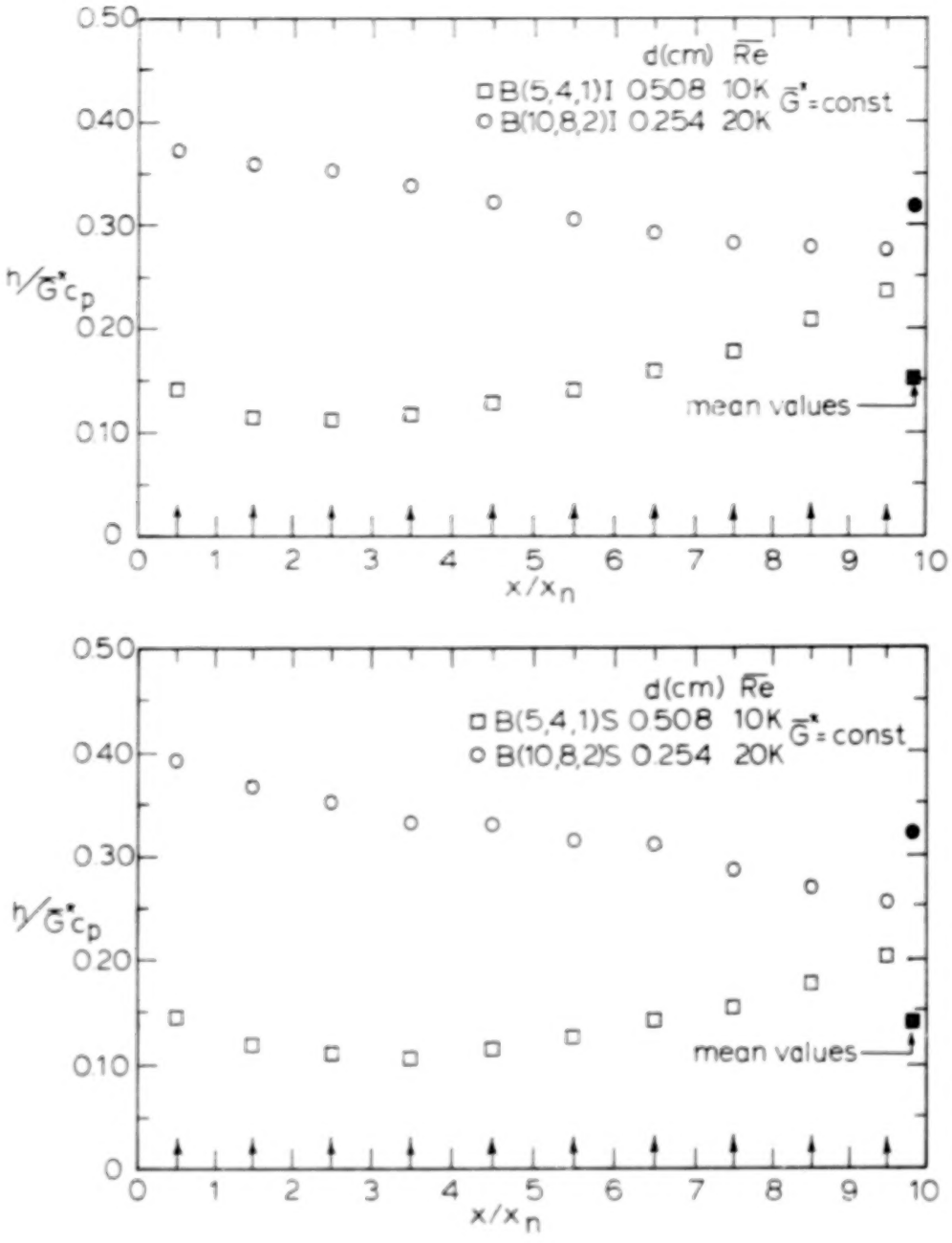

Fig. 4.8 Effect of hole diameter on low-resolution chordwise heat transfer coefficient profiles and mean values for fixed $\bar{G}^*$ - inline and staggered hole patterns.

is slightly more than doubled. This, of course, occurs at the expense of an increased pressure drop. Note also the profiles have significantly different shapes.

4.4.3 Effect of Hole Spacing

Additional chordwise Nusselt number profiles drawn from the B-size tests are presented in the series of graphs of Fig. 4.9. The open points represent data for the specified inline hole patterns, while the solid points represent data for the corresponding staggered hole patterns. For the moment attention is focused on the inline hole pattern data only (open points). Discussion of the effect of inline vs. staggered hole patterns will be taken up in the next section. The individual graphs directly compare profiles for $y_n/d = 4$ with those for $y_n/d = 8$, all for the same $\overline{Re}^*$, at specified values of x_n/d and z/d. Such a comparison directly reflects the effect of spanwise hole spacing, y_n, for a fixed G^*, and otherwise fixed geometry (x_n, z, d, ℓ and hole pattern). It is apparent that, compared in this way the mean heat transfer coefficients for $y_n/d = 8$ are significantly larger than those for $y_n/d = 4$ irrespective of the values of the other geometric parameters, x_n/d and z/d.

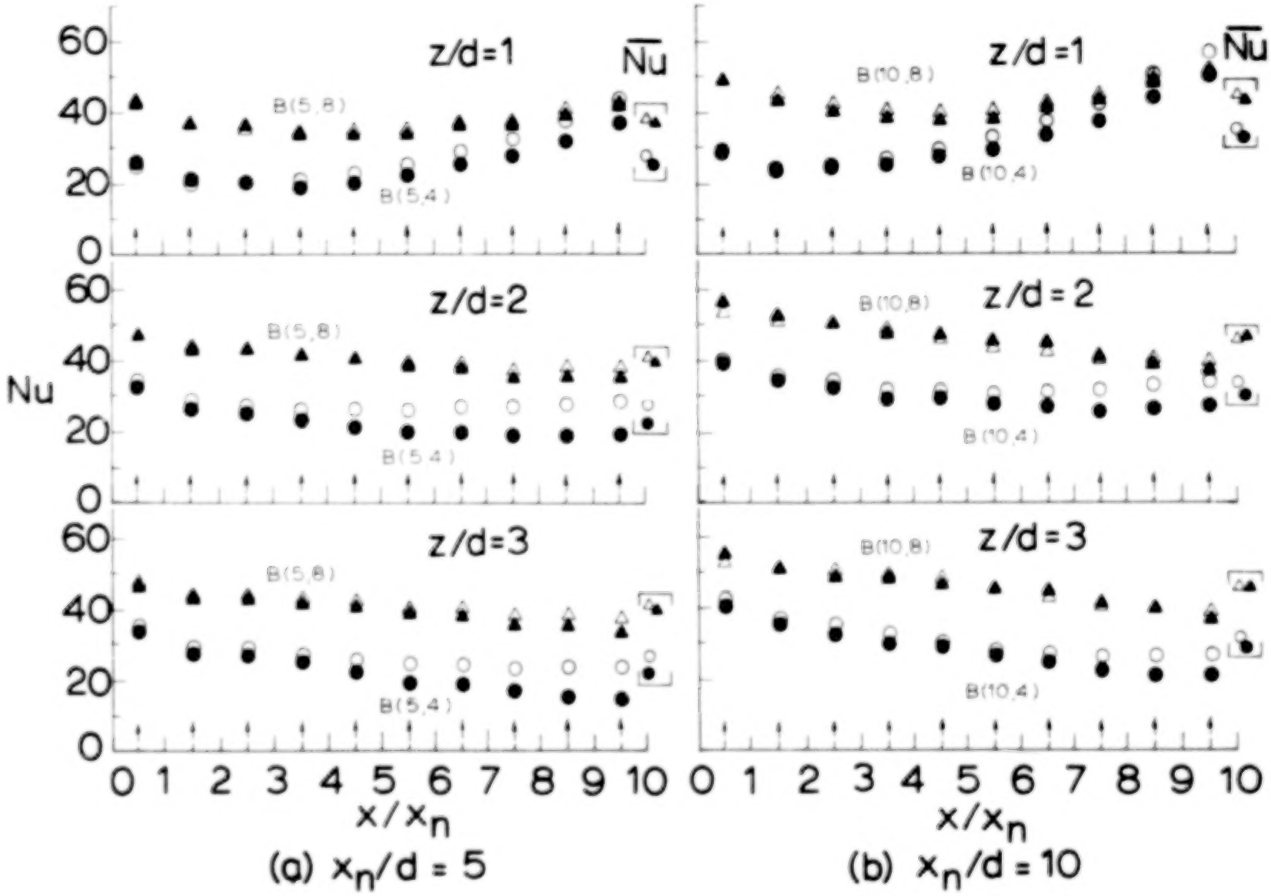

Fig. 4.9 Effect of hole spacing and hole pattern on low-resolution chordwise Nusselt number profiles and mean values. Open points are inline patterns. Solid points are corresponding staggered patterns. $\overline{Re}^* = 196$.

However, the chordwise profiles show that for z/d = 1 and 2 the differences are largest upstream; and, for z/d = 1, in particular, almost disappear downstream. For z/d = 3 the differences are fairly uniform along the channel. This behavior lends support to the view that for the smaller channel heights there is a significant contribution to the downstream heat transfer due to the crossflow.

The effect of varying the chordwise hole spacing for a fixed cooled surface length cannot be determined directly from the present data base since the ratio ℓ/x_n was fixed at ten for all tests. In Fig. 4.9, increasing x_n/d from 5 to 10 does show the effect of spreading ten spanwise rows of holes over twice the cooled surface length while maintaining a fixed $\overline{G}^*$ and otherwise fixed geometry (y_n, z, d, and hole pattern). Such an increase in x_n increases the mean heat transfer coefficient irregardless of the values of the other geometric parameters.

It will subsequently be possible to determine the effect of varying N_c (i.e., x_n independently of ℓ) utilizing the present data base. The value of $\overline{Nu}$ can be calculated over any number of upstream rows less than ten. To properly interpret and compare such results, however, the mean jet Reynolds number over the corresponding number of rows must be determined. Such a procedure requires accurate knowledge of the chordwise jet flow distribution, and should be checked experimentally by selected tests utilizing jet plates with varying numbers of spanwise rows. The necessary data is currently being analyzed in order to extend the present results.

4.4.4 Effect of Hole Pattern

Attention is now turned to the comparison between heat transfer coefficients for the corresponding inline and staggered hole patterns. A major result obtained from these comparative tests is that the mean heat transfer coefficients for the inline patterns were in every case equal to (within experimental uncertainty) or larger than those for the corresponding staggered patterns. This is illustrated in Fig. 4.9 for the B-size data, where it is apparent that the largest differences occurred for the highest hole density B(5,4) at the largest channel heights, z/d = 2 and 3. For these cases the inline mean heat transfer coefficients exceed the staggered values by 18%. Little or no effect is apparent for the largest spanwise spacing, $y_n/d = 8$, regardless of the values of the other parameters. For B(10,4) the inline mean values exceed the staggered values by about 10%. These chordwise profiles clearly show that the hole pattern effect increases in significance in the downstream direction. For B(5,4),z/d = 3, the downstream ($x/x_n = 9.5$) value of Nu for the inline pattern exceeds the staggered value by about 60%, indicating that the local effects can be quite significant. It seems reasonable that these hole pattern effects would tend to be most significant at the downstream locations, and for the highest hole density at the largest channel height since all of these conditions presumably enhance the possible degree of interaction of adjacent jets. With the complex jet and crossflow interactions which occur in these flow configurations it is not immediately obvious, however, why it is the inline pattern which produces the highest heat transfer rates. This point is discussed further in the next section, following presentation of the higher-resolution results.

A summary comparison of mean Nusselt numbers for all configurations for which both inline and staggered hole patterns were tested is presented in Table 4.6 as a function of jet Reynolds number. Test results for $Re > 2 \times 10^4$ were obtained for the staggered pattern for only two configurations, both in D-size. For these cases the comparison is presented up to $\overline{Re} = 3.5 \times 10^4$; otherwise the comparison is limited to $\overline{Re} \leq 2 \times 10^4$, so as not to require extrapolation of the staggered pattern data. It may be observed that to within experimental uncertainty, ratios of $\overline{Nu}$ for staggered patterns to $\overline{Nu}$ for corresponding inline patterns are less than or equal to unity and are independent of $\overline{Re}$.

Table 4.6 Ratio of $\overline{Nu}$ for Staggered Hole Pattern to that for Corresponding Inline Pattern

Size	$(x_n/d, y_n/d)$	z/d	$\overline{Re}$ (10^3)			
			5	10	20	35
A	(10,6)	1	0.93	0.91	0.90	--
		2	0.91	0.90	0.89	--
		3	0.85	0.88	0.91	--
		6	0.86	0.90	0.94	--
B	(5,4)	1	0.90	0.91	0.92	--
		2	0.84	0.85	0.87	--
		3	0.85	0.85	0.85	--
B	(5,8)	1	0.99	0.98	0.97	--
		2	0.98	0.98	0.97	--
		3	0.94	0.95	0.96	--
		6	0.95	0.94	0.93	--
B	(10,4)	1	0.92	0.92	0.92	--
		2	0.90	0.90	0.89	--
		3	0.90	0.92	0.94	--
B	(10,8)	1	1.04	1.00	0.97	--
		2	1.01	1.01	1.01	--
		3	0.93	0.98	1.02	--
C	(5,8)	1	0.99	0.97	0.96	--
		2	0.96	1.00	1.04	--
		3	0.95	0.94	0.93	--
C	(10,4)	1	0 94	0.95	0.96	--
		2	0.88	0.89	0.89	--
		3	0.91	0.93	0.95	--
C	(10,8)	1	1.02	0.99	0.97	--
		2	0.97	0.98	0.99	--
		3	0.97	0.96	0.96	--
D	(5,4)	1	0.93	0.94	0.94	0.95
		3	0.85	0.85	0.86	0.86

4.5 Higher-Resolution Heat Transfer Characteristics

The low-resolution results clearly show the overall chordwise trends, but do not detect the significant periodic variations which were observed when the resolution was increased to better than one chordwise hole spacing, as was possible for the C and D-size data. These variations are most clearly shown by the D-size data at its maximum resolution of $x_n/3$. However, caution must be exercised in the interpretation of the data for C-size at its maximum resolution of $x_n/2$, for the reasons already noted in Section 4.2.

In this section the effect of the geometric parameters on the characteristics of the periodic variations is discussed utilizing the results from the D-size tests. Higher-resolution Nusselt number profiles for each D-size configuration tested are shown in the series of plots of Figs. 4.10 thru 4.15. The resolved values are plotted as ratios to the corresponding mean values for $\overline{Re} = 1.5 \times 10^4$. Over the range of $\overline{Re}$ covered (5×10^3 to 5×10^4), some dependence of these normalized higher-resolution Nusselt numbers on $\overline{Re}$ was observed. However, the basic character of the periodic variations as a function of the geometric parameters remained the same over the entire range of $\overline{Re}$. Thus, the profiles presented in Figs. 4.10 thru 4.15 for $\overline{Re} = 1.5 \times 10^4$ are representative of the geometric effects over this entire range. Profiles smoothed across the periodic variations are also shown for each case. These curves were drawn thru the data points resolved to one chordwise spacing (points omitted for clarity). Each figure is for a given hole spacing combination (x_n/d, y_n/d), with individual plots for each z/d (= 1, 2, and 3). All results shown are for inline patterns only, except for configurations D(5,4,1) and D(5,4,3) (Fig. 4.10) for which results for the staggered pattern were also obtained. The D-size tests were run in the staggered pattern for the (5,4) hole spacing since prior low-resolution results had indicated the hole pattern effect was largest for this spacing.

In examining these results it may be helpful for the reader to refer to Fig. 2.3 which shows the relationship between the spanwise rows of holes and the test plate segments. It should also be borne in mind that while the chordwise resolution was fine enough to clearly show the nature of the periodic variations, the results do not precisely reflect profiles of infinite resolution which would show even larger amplitude variations.

In this connection, the maximum chordwise resolution of heat transfer coefficients relative to hole diameter for the D-size should be noted. Since $N_C = \ell/x_n$ was fixed at ten for all tests, and ℓ is constant for a given size configuration, x_n was also constant for all tests of a given size. Thus, the parameter x_n/d was varied by changing d. Since the heat transfer surface segment width was fixed, the chordwise resolution relative to hole diameter was different depending on the x_n/d of the jet plate under test. These resolutions were 1.67d for $x_n/d = 5$, 3.33d for $x_n/d = 10$, and 5d for $x_n/d = 15$; they were independent of all other geometric parameters. Therefore, for a given x_n/d, comparisons made to examine the effects of other geometric parameters reflect identical resolutions relative to hole diameter.

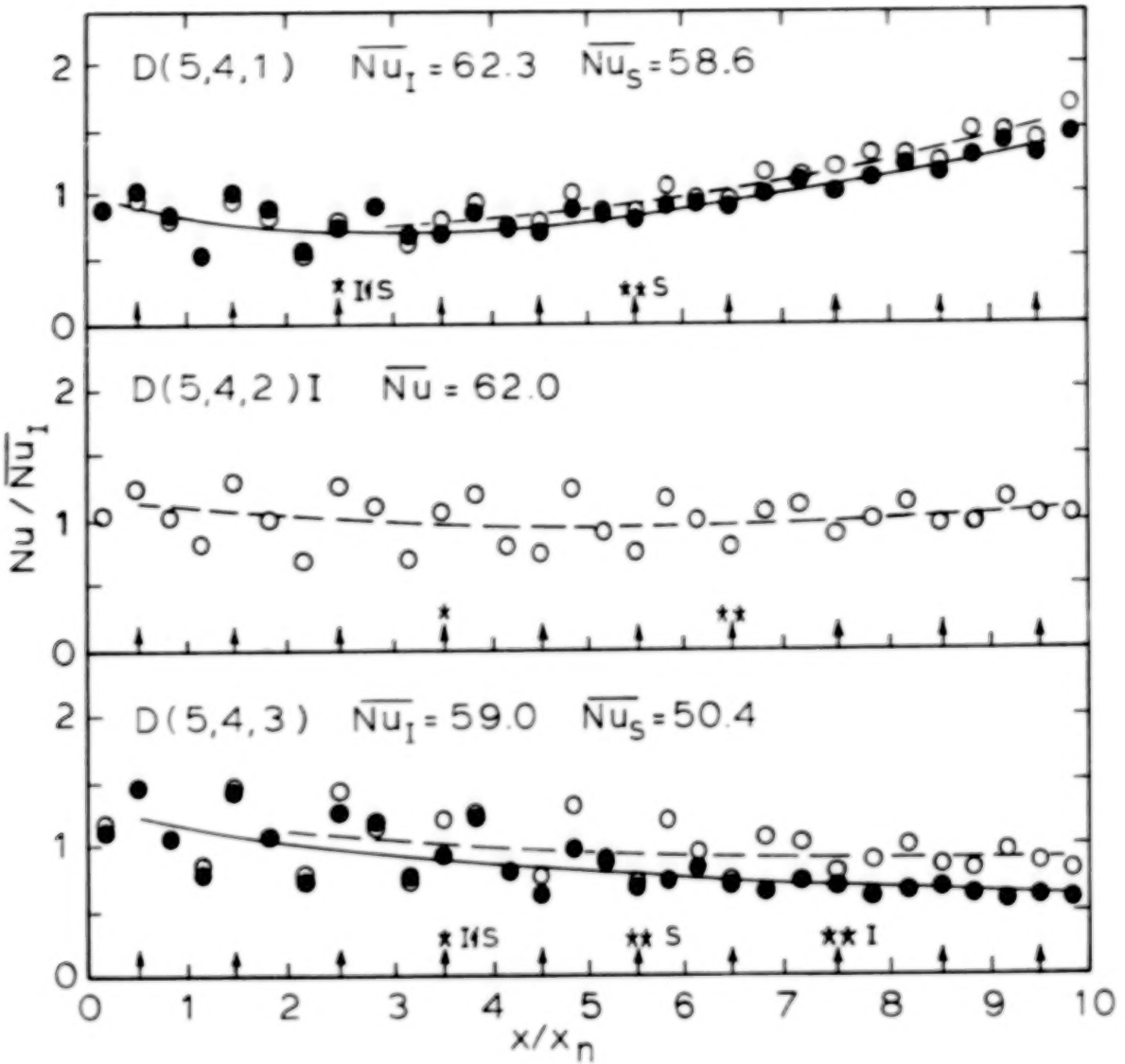

Fig. 4.10 Normalized higher-resolution chordwise Nusselt number profiles for inline (open points) and staggered (solid points) patterns for D(5,4) configuration.

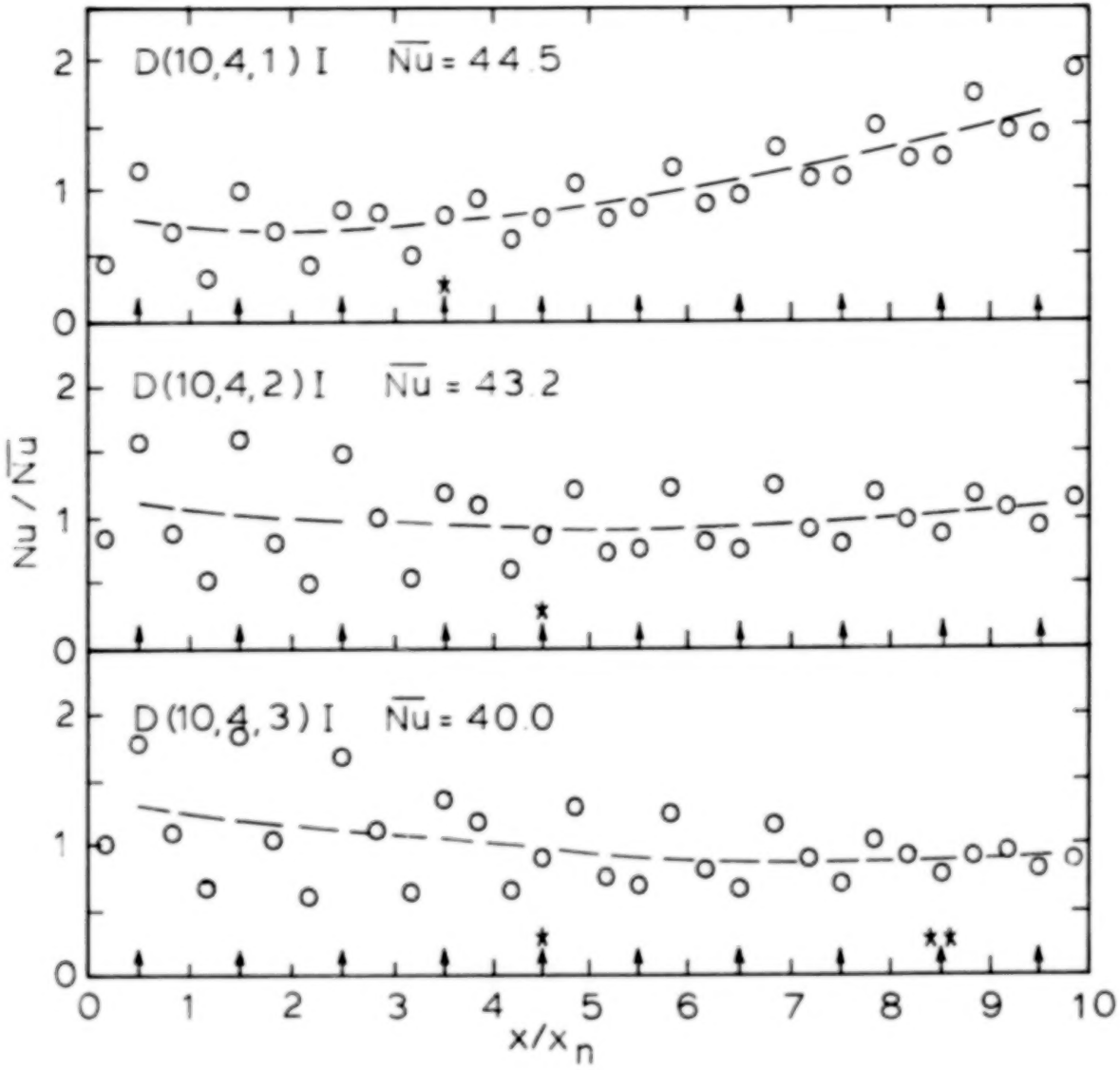

Fig. 4.11 Normalized higher-resolution chordwise Nusselt number profiles for D(10,4)I configuration.

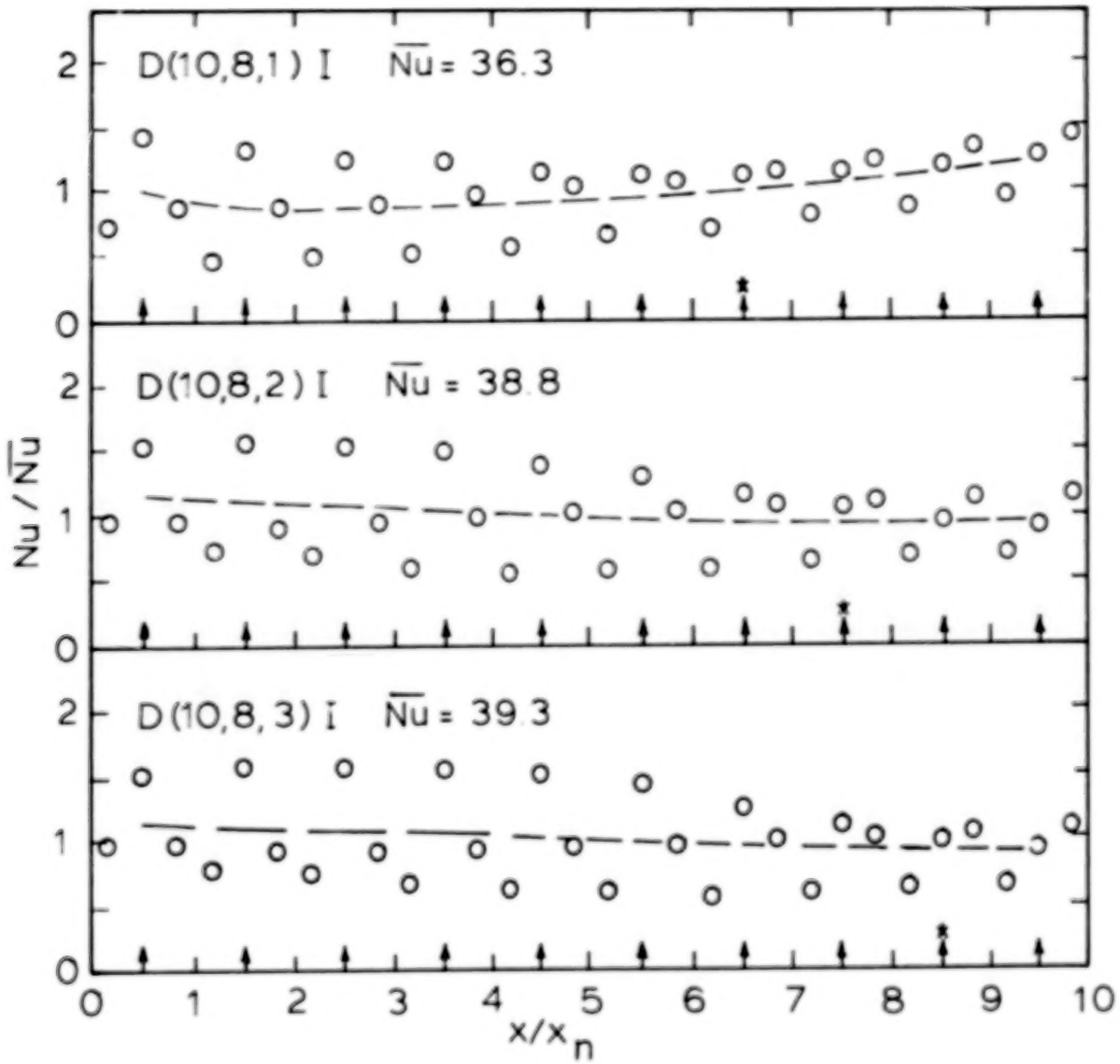

Fig. 4.12 Normalized higher-resolution chordwise Nusselt number profiles for D(10,8)I configuration.

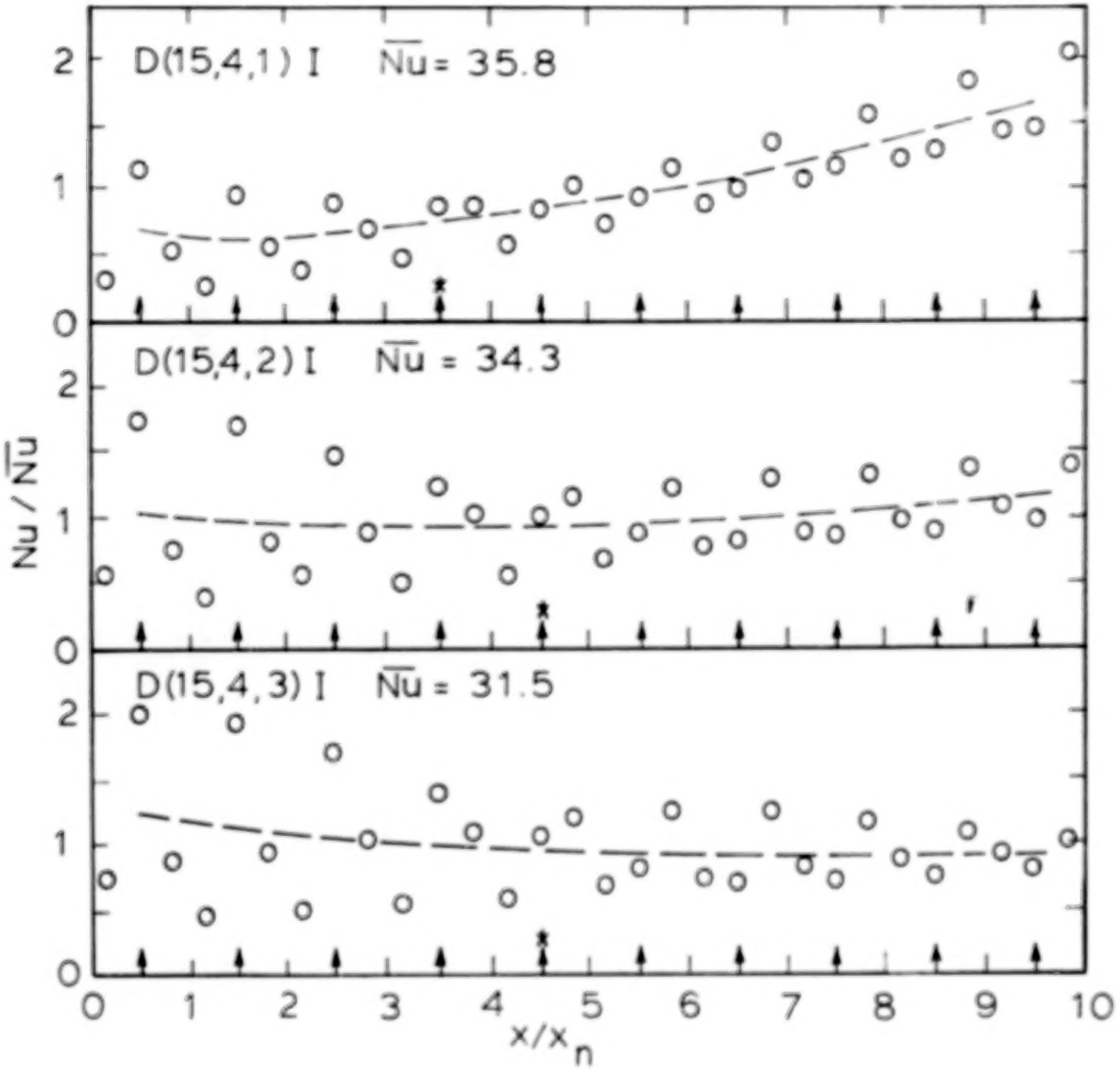

Fig. 4.13 Normalized higher-resolution chordwise Nusselt number profiles for D(15,4)I configuration.

BLANK PAGE

BLANK PAGE

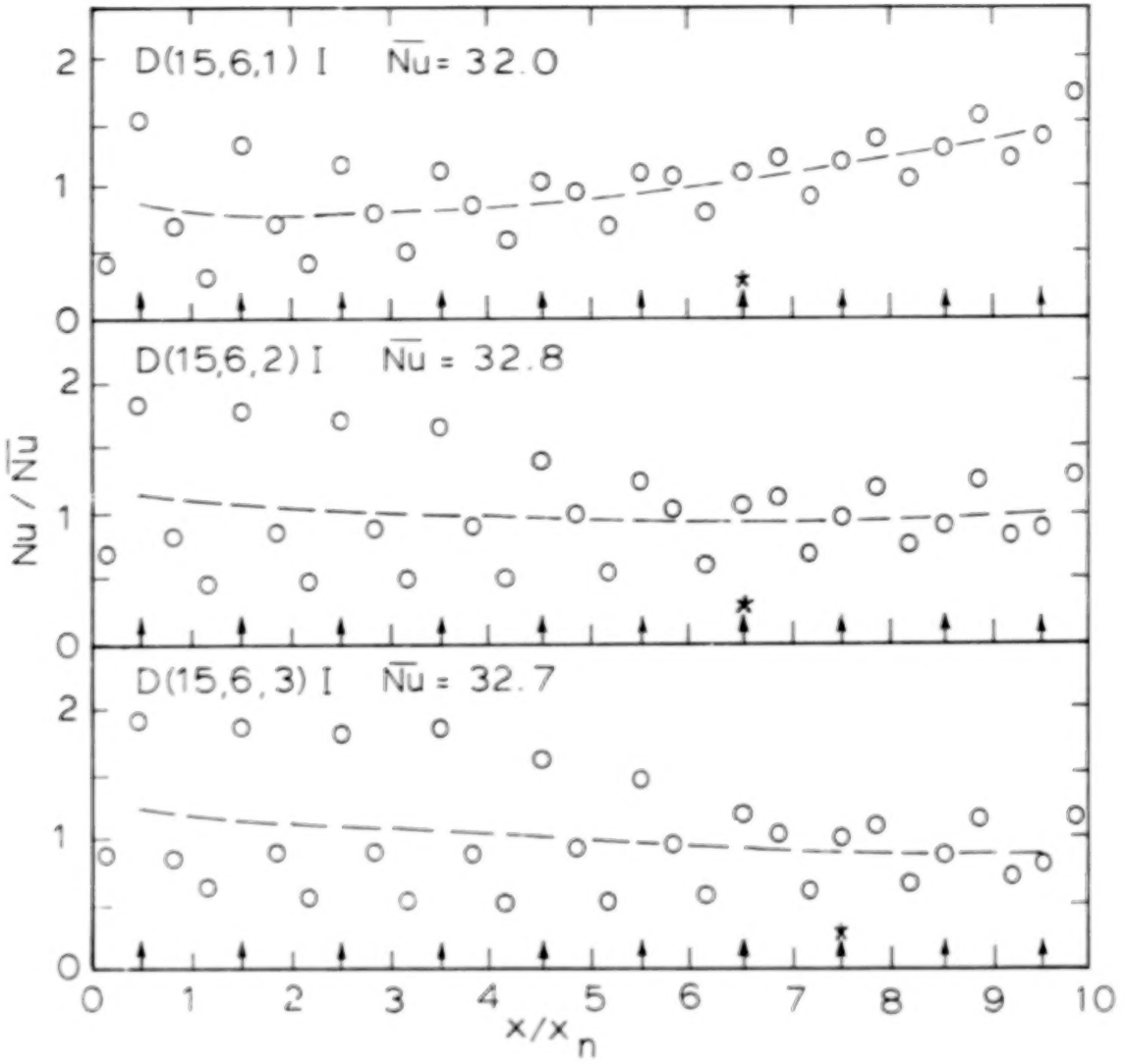

Fig. 4.14 Normalized higher-resolution chordwise Nusselt number profiles for D(15,6)I configuration.

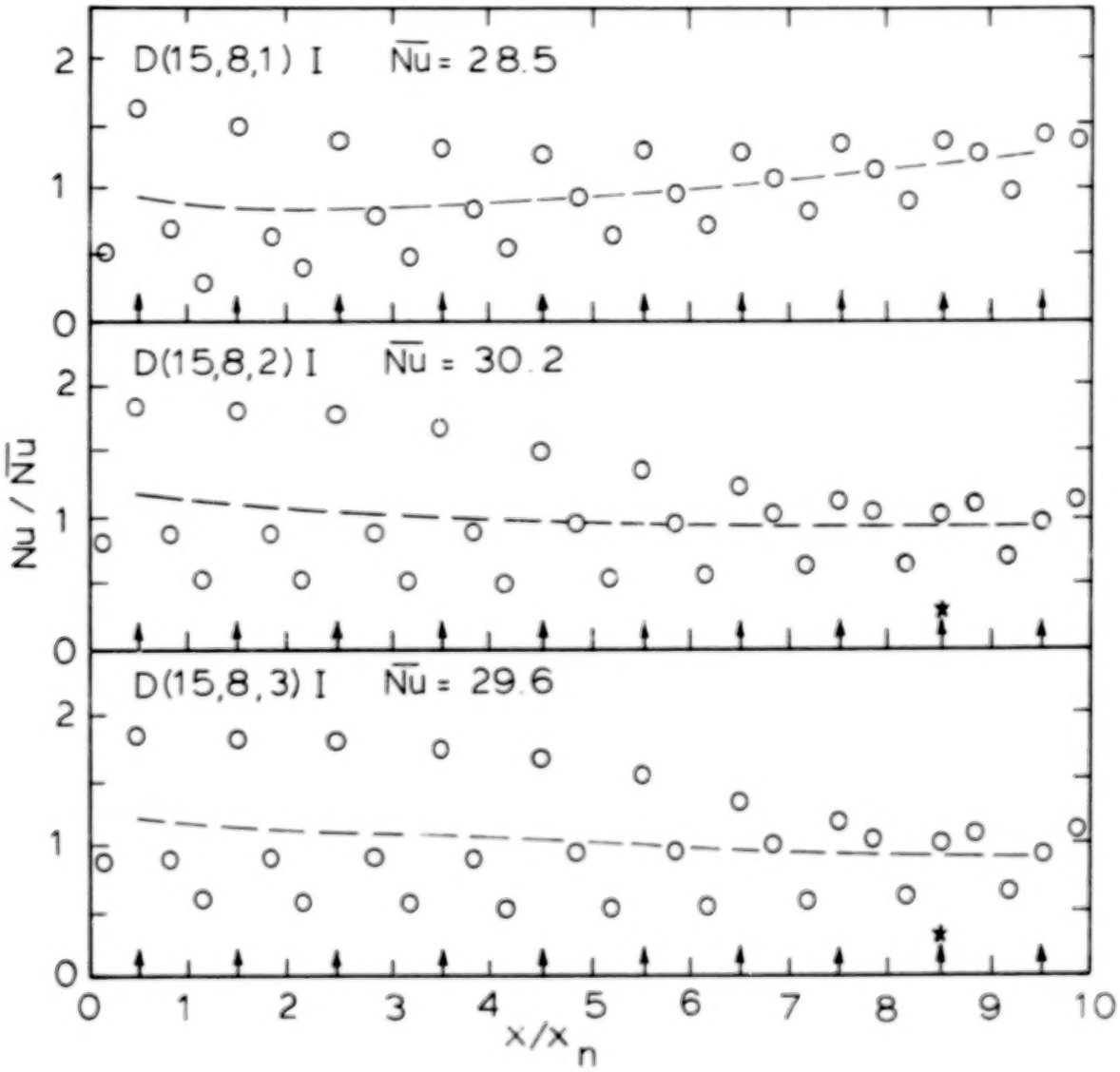

Fig. 4.15 Normalized higher-resolution chordwise Nusselt number profiles for D(15,8)I configuration.

Characteristic of these results are the amplitude attenuation and the increasing displacement of the peak value of Nu for each row of holes as one proceeds in the downstream direction, effects clearly associated with the influence of the increasing crossflow magnitude. These and other characteristics of the higher-resolution D-size results are discussed in detail in the following paragraphs.

Values of $Nu/\overline{Nu}$ (Figs. 4.10 to 4.15) range overall from 0.25 to just over 2. For $z/d = 1$, the peak value associated with the last row of jets is always larger than or equal to the other peak values, with the single exception of the least dense hole array, configuration D(15,8,1)I. For $z/d = 2$ and 3, the largest peak values are always associated with the upstream jet rows. In general, the minimum values for each row of a given configuration are more uniform than the peak values.

For the closest spanwise spacing, $y_n/d = 4$, the amplitude attenuation becomes stronger as z/d is increased. The upstream amplitudes are somewhat larger for $z/d = 2$ and 3 than for $z/d = 1$, while downstream the reverse is true. While the high resolution nonuniformity increases with z/d, the smoothed profiles become more nearly uniform. For $y_n/d = 8$, both the upstream and downstream amplitudes, and hence the degree of amplitude attenuation are similar for all z/d. Likewise, the smoothed profiles are all fairly uniform.

Viewed from the standpoint of the effect of y_n/d for a fixed z/d, it may be observed that for $z/d = 1$ the resulting downstream amplitudes are not sensitive to y_n/d, but for $z/d = 2$ and 3 the amplitude is clearly damped out more for $y_n/d = 4$ than 8.

The results clearly indicate that the presence of the crossflow downstream can strongly attentuate the periodic variations. If, in applications, thermal stresses proved to be severe at upstream locations due to the large periodic variations of the heat transfer coefficient, the presence of an initial crossflow would certainly be advantageous in alleviating such a problem.

As previously discussed (Section 4.4.3) the effect of varying the chordwise hole spacing for a fixed cooled surface length cannot be determined directly from the present data since the ratio ℓ/x_n was fixed at ten for all tests. However, comparison of results in Figs. 4.10 thru 4.15 for the several values of x_n/d (5,10, and 15) with the other parameters fixed shows that spreading ten rows of holes over a larger surface length (i.e., increasing both x_n and ℓ, while holding d, y_n, and z fixed) clearly increases the amplitude of the variations both upstream and downstream. Indeed, infinitely resolved chordwise profiles would undoubtedly show this increase to be even more pronounced, since the smallest amplitude data, for $x_n/d = 5$, were obtained with the highest resolution relative to hole diameter, while the largest amplitude results, for $x_n/d = 15$, were obtained with the lowest resolution relative to hole diameter.

Attention is now turned to the increasing displacement of the peak value of Nu for each row of holes which occurs in the downstream direction. It may be observed (Figs. 4.10 to 4.15) that upstream the peak value of $Nu/\overline{Nu}$ associated

with a spanwise row of holes is always for the heat transfer surface segment centered directly opposite the row, while at some row downstream the peak value shifts to the segment immediately downstream of that row. Since the segment width is $x_n/3$ for the D-size configurations, this means that the local peak value of Nu for that row is displaced by at least $(1/2)(x_n/3) = x_n/6$ downstream of the row location. The row at which this peak shift occurs is marked by a single asterisk in each plot of Figs. 4.10 thru 4.15.

In several instances, [D(5,4) at all z/d (Fig. 4.10) and D(10,4) at z/d = 3 (Fig. 4.11)], the peak value subsequently shifts to the second segment downstream of the row location. These rows are marked by a double asterisk. At these rows the local peak value is displaced by at least $(1.5)(x_n/3) = x_n/2$ downstream of the row location. For other configurations this second peak shift is not observed.

Examination of these peak shift points gives an indication of how rapidly the displacement of the local peak value of Nu increases from row to row depending on the geometric parameters of the configuration. Overall, this displacement appears to be a weak function of z/d over the range covered, but depends more strongly on y_n/d. The trend is for the displacement at a given row to be smaller for the larger y_n/d. There is a similar trend, though not as strong, with x_n/d. For the most dense hole packing in inline pattern, D(5,4)I (Fig. 4.10), the displacement has reached a value of $x_n/2$ about 3/4 of the way down the channel, while for the lowest hole density, D(15,8)I (Fig. 4.15), it is still only approaching $x_n/6$ as the end of the channel is reached.

It is tempting to identify the observed displacement of the local peak values of Nu with the distance by which the jet impingement points are deflected downstream from the centerlines of the jet holes, since the observation of a peak shift from one segment to the next undoubtedly depends strongly on the location of the impingement point relative to the segments. However, the particular row at which a peak shift is observed may also depend somewhat on the local distribution of Nu about the impingement point. Due to the crossflow this distribution presumably becomes flatter and more asymmetrical from row to row in the downstream direction. The presence of crossflow also has some direct contribution to the segment Nu values, since they are averaged over the spanwise direction. Despite these uncertainties, the evidence suggests that the deflection of the jet impingement point itself is primarily dependent on y_n/d, with only a weak dependence on z/d and x_n/d over the range of these parameters covered.

The ratio of the crossflow mass velocity to the jet mass velocity will decrease with both z/d and y_n/d. The observed effect of y_n/d on the displacement of the peak values is consistent with this trend. The fact that the effect of z/d on this displacement is not as strong may be due to a compensating effect. The path length of the jet from injection point to impingement point is longer for larger z/d. Thus, even for the same crossflow-to-jet velocity ratio the displacement of the impingement point would be larger for larger z/d.

The effect of hole pattern on the mean values and the chordwise profiles of Nu resolved to one chordwise hole spacing were discussed in Section 4.4.4. The higher-resolution results presented in Fig. 4.10 provide some additional insight into the effects of the staggered pattern as compared with the inline pattern. It appears that the periodic variations are essentially identical upstream for the two hole patterns, but like the smoothed profiles differ significantly downstream. The amplitude attenuation is more severe for the staggered pattern than for the inline, especially for z/d = 3, and in this case the variation for the staggered pattern has almost disappeared at the downstream end. The second peak shift (double asterisk) occurs further upstream for the staggered patterns than for the inline. Both of these effects suggest that the crossflow/jet interactions and possible resulting interactions between adjacent jets are stronger for the staggered pattern.

One may speculate as follows. Consider a particular spanwise row for the inline pattern. Most of the crossflow from fluid injected at this row is diverted due to the presence of the jets in the row immediately downstream so that it flows between these jets. The path of least resistance for this fluid is to continue flowing down imaginary channels between adjacent pairs of chordwise rows. Thus, for the inline pattern the jets across a given spanwise row tend to be deflected downstream and diffused primarily due to crossflow from the row immediately upstream; each row tends to be "protected" from crossflow originating two rows upstream by the jets of the row immediately upstream. The hypothesis that the crossflow for the inline patterns tends to be channelized between adjacent chordwise hole rows is consistent with observations of discoloration patterns on the test surface which suggest such a flow pattern.

In contrast, for the staggered pattern the flow for a jet hole of, say, spanwise row n first flows directly between two jets in row n + 1. It is then diverted to flow around a jet in row n + 2, and in so doing joins the crossflow originating from the hole directly upstream in row n + 1. This combined flow, along with any existing crossflow already originated upstream, interacts directly with the immediately downstream jet in row n + 3. Thus, the direct influence of the crossflow on each jet is larger than for the inline case. Each jet is therefore deflected and diffused more than its inline counterpart would be. This reduces the contribution to the heat rate made by the jet, thus reducing the spanwise average Nu.

Close examination of the inline vs. staggered data points for D(5,4,3) (Fig. 4.10) indicates that as the crossflow effect increases downstream the difference between the inline and staggered peak values for each row is larger than for the minimum values. This observation also suggests that the degradation of the jet impingement heat transfer is greatest for the staggered case, and is a major factor in the reduction of the overall heat transfer rate as compared with the inline pattern. However, it should be emphasized that the differences due to hole pattern become significant only for the denser hole patterns.

The effect of hole diameter on the chordwise periodic variations of the heat transfer coefficient is shown in Fig. 4.16 under the condition that other geometric parameters as well as the mean flow rate per unit heat transfer

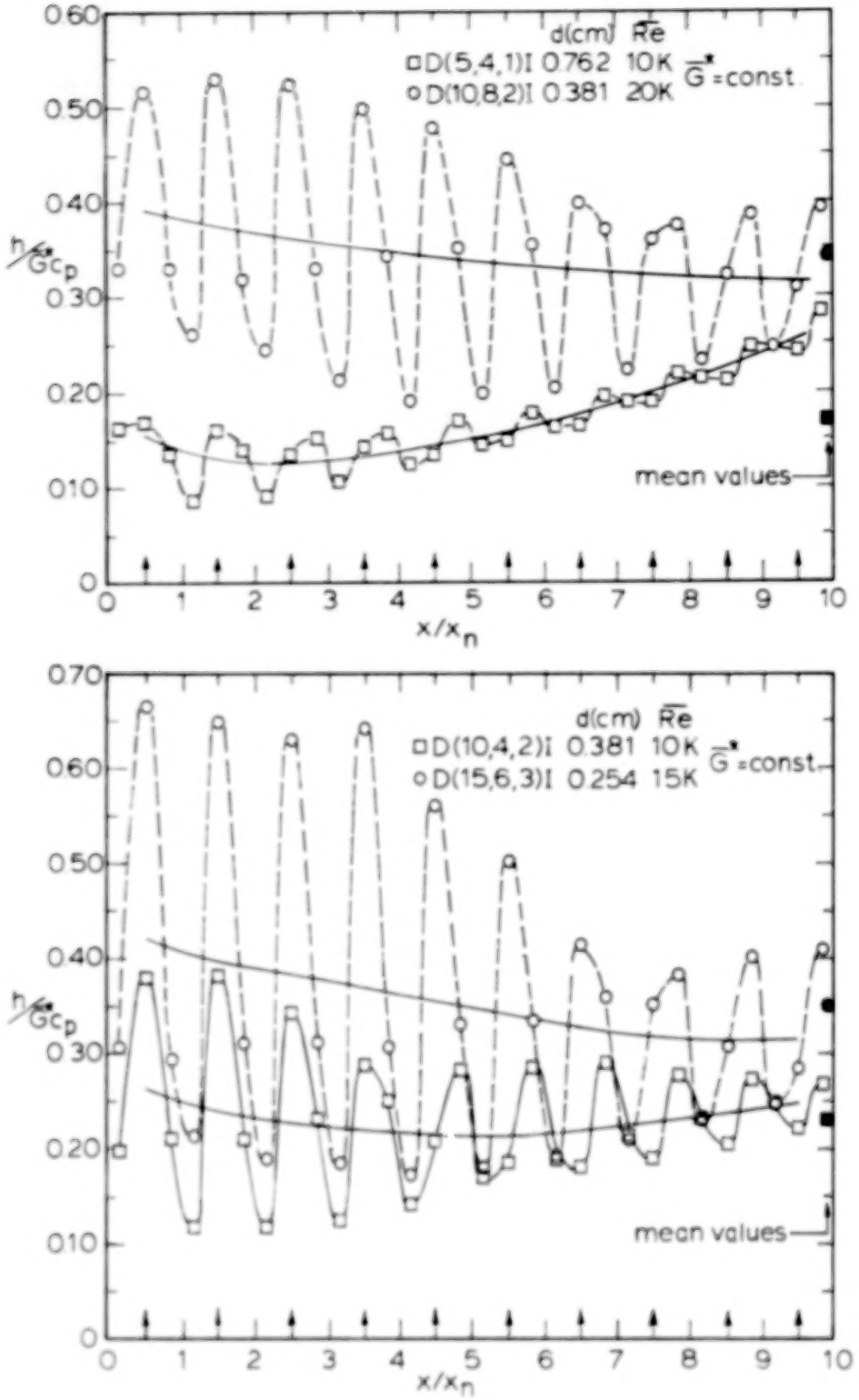

Fig. 4.16 Effect of hole diameter on chordwise periodic variations, smoothed profiles, and mean values of heat transfer coefficient for fixed $\bar{G}^*$ - inline hole pattern.

surface area ($\bar{G}^*$) are held fixed. This is accomplished in dimensionless form utilizing a Stanton number defined as $h/\bar{G}^* c_p$ rather than a Nusselt number.

The effect of reducing the hole diameter by one-half is shown in the upper plot of Fig. 4.16, by comparing results for configuration D(5,4,1)I with those for D(10,8,2)I. The effect of this reduction in diameter is to double the mean heat transfer coefficient and provide a more uniform smoothed profile, but significantly increase the amplitude of the periodic variations.

The lower plot of Fig. 4.16 represents a case where the diameter is reduced by two-thirds, by comparing configurations D(10,4,2)I and D(15,6,3)I. Here the mean heat transfer coefficient is increased by about 50%, the amplitudes of the variations are again increased, but there is not a strong effect on the uniformity of the smoothed profile. It should be emphasized that the increases in amplitude with diameter reduction as shown in Fig. 4.16 would be even larger if the chordwise resolution were infinitely small. This is because, as already indicated, the resolution relative to hole diameter is better for the larger hole diameters since the heat transfer test plate segment size was fixed for all tests.

For constant $\bar{G}^*$ the mean heat transfer coefficient varies essentially inversely with hole diameter over the parameter ranges covered by these results. From this standpoint, the use of smaller hole diameters for turbine airfoil cooling is quite advantageous. The disadvantages include the significantly increased pressure drop, the increased probability of plugging of holes with foreign matter, and the potential for thermal stress problems associated with the very large spatial variations of the heat transfer coefficient. The designer must also weigh these effects against the influence of hole diameter on the smoothed chordwise profiles.

5. SUMMARY OF RESULTS

Extensive experimental results for crossflow impingement heat transfer characteristics of configurations which model those of interest in current and future gas turbine airfoil cooling applications have been obtained. The configurations tested were inline and staggered two-dimensional arrays of circular jets with ten spanwise rows of holes. The cooling air was constrained to exit in the chordwise direction along the channel formed by the jet orifice plate and the heat transfer surface.

Mean and chordwise resolved Nusselt numbers as a function of mean jet Reynolds number have been documented in tabular form. The characteristics of these results have been presented in graphical form drawn from the tabular data. Interpolated data points were used where necessary or appropriate for making comparisons.

Results for the maximum chordwise resolution of one-third the chordwise hole spacing, referred to as higher-resolution results, reflect the periodic variations of the chordwise heat transfer coefficient profiles. Results resolved to one or two chordwise hole spacings, referred to as low-resolution results, show more clearly the nature of the profiles smoothed across the periodic variations.

A significant characteristic of the low-resolution profiles is the occurrence of a minimum value of the heat transfer coefficient for the smaller channel heights and spanwise hole spacings. For the smallest channel height and spanwise hole spacing (one and four hole diameters, respectively) the downstream heat transfer coefficients are significantly larger than the upstream values.

The mean heat transfer coefficients are not very sensitive to channel height, irregardless of hole spacings. However, for the smallest spanwise spacing the shapes of the chordwise profiles vary significantly with channel height. Upstream the low-resolution heat transfer coefficients are smallest for the smallest channel height, while downstream the reverse occurs. At some intermediate location the profiles intersect such that the heat transfer coefficients are identical for all channel heights tested. When the spanwise spacing is doubled to eight diameters the same trends with channel height occur but the differences are much less pronounced. That is, the low-resolution profiles are quite similar and fairly uniform.

For a fixed mass flow rate, the mean heat transfer coefficients vary inversely with hole diameter. Reducing the hole diameter tends to provide a more uniform low-resolution heat transfer coefficient profile, but greatly increases the amplitude of the periodic variations.

For a fixed flow rate per unit hole area the mean heat transfer coefficient increases as the holes are spaced more closely, but for a fixed flow rate per unit heat transfer surface area the mean coefficient increases as the holes are spaced farther apart. The low-resolution coefficients also follow these trends,

but the chordwise profiles for different hole spacings do not always lie uniformly above or below each other, particularly for the smaller channel heights.

For the larger hole spacings tested the mean and resolved heat transfer coefficient characteristics for corresponding inline and staggered patterns are essentially identical. However, as the hole spacing was decreased the differences became significant, particularly for the larger channel heights and toward the downstream end of the channel. For a chordwise spacing of five, a spanwise spacing of four, and a channel height of three hole diameters, the inline mean heat transfer coefficient exceeds the staggered value by 18%. At the final downstream spanwise row (the tenth row) the low-resolution inline value exceeds the staggered value by 60%.

The higher-resolution results show that large periodic variations in heat transfer coefficients exist upstream, and, though damped, can remain significant downstream at the tenth row of holes. However, for the densest hole packing at its largest channel height in the staggered pattern, the variations essentially disappear after the seventh row. These results also indicate that the downstream deflection of the jet impingement points due to the crossflow is nearly independent of channel height over the range covered, but increases with decreasing hole spacing; and for the densest hole packing this deflection at the downstream end of the channel exceeds one-half the chordwise hole spacing.

6. CONCLUDING REMARKS

One of the motivations for the investigation was to obtain additional information on the effect of the crossflow originating from upstream jets on the downstream heat transfer characteristics. A significant result is that the heat transfer coefficients do not always decrease monotonically as the crossflow rate increases in the downstream direction. Indeed, it was found that for narrow channel heights and close spanwise hole spacings the downstream values are significantly larger than those upstream. For $z/d = 1$ and $y_n/d = 4$ the value (resolved to one chordwise spacing) at the tenth row was more than double the minimum value which occurred upstream at the second or third row. This type of behavior is significant for the designer to keep in mind, particularly since the implication might be drawn from several prior studies, which included suggested correlations, that heat transfer performance always tends to be degraded downstream with increasing crossflow [5,6]. A second significant result is the characterization of the amplitude attenuation of the chordwise periodic variations due to the crossflow. A final significant result involving crossflow effects is the observation that for arrays with smaller hole spacings in the presence of a crossflow, the inline pattern results in significantly higher heat transfer coefficients than the staggered pattern.

When compared at a fixed mean jet Reynolds number, some of the heat transfer results for the smaller size configurations differed from those for their larger geometrically similar counterparts by amounts significant relative to experimental uncertainties. For the smaller hole sizes at the larger flow rates, these differences appear to be attributable to compressibility effects arising because of the large pressure drops required relative to the laboratory air supply pressure levels. The pressure levels in the anticipated turbine application are much higher with correspondingly lower Mach numbers, so that in this sense, it is expected that the data for the larger sizes best models the prototype heat transfer characteristics. However, even apart from the latter consideration, the differences observed are considered to be of only minor significance, if any, from the standpoint of design application. Therefore, the crossflow impingement heat transfer characteristics reported herein for two-dimensional arrays of circular jets should be of immediate utility in design activities.

Of further utility and convenience to the designer is a formal prediction scheme which may be applied in appropriate detail and with good confidence. Such a prediction scheme is particularly essential for conducting optimization studies. The heat transfer data base documented herein will serve as the basis for development of correlations which it is hoped will meet this need. This development is currently underway. An attempt is being made to correlate heat transfer coefficients resolved to one chordwise hole spacing with the individual jet and crossflow rates of spanwise hole rows and with geometric parameters. Additional current activity includes acquisition of data for jet arrays in the presence of an initial crossflow introduced upstream of the array at a temperature equal to or greater than that at which the jet air is introduced. As noted in the Introduction such configurations are also of interest for turbine cooling applications. If correlation development in terms of jet and crossflow

rates localized to individual rows is successful for the noninitial crossflow heat transfer results documented herein, the correlation will then be tested against the initial crossflow data as well.

REFERENCES

1. Gauntner, J.W., Gladden, H.J., Gauntner, D.J., and Yeh, F.C., "Crossflow Effects on Impingement Cooling of a Turbine Vane," NASA TM X-3029, March 1974.

2. Metzger, D.E., Florschuetz, L.W., Takeuchi, D.I., Behee, R.D., and Berry, R.A., "Heat Transfer Characteristics for Inline and Staggered Arrays of Circular Jets with Crossflow of Spent Air," ASME Journal of Heat Transfer, Vol. 101, 1979, pp. 526-531.

3. Friedman, S.J., and Mueller, A.C., "Heat Transfer to Flat Surfaces," Proceedings, General Discussion on Heat Transfer, The Institute of Mechanical Engineers, London, England, 1951, pp. 138-142.

4. Huang, G.C., "Investigations of Heat Transfer Coefficients for Air Flow Through Round Jets Impinging Normal to a Heat Transfer Surface," ASME Journal of Heat Transfer, Vol. 85, pp. 237-243.

5. Kercher, D.M., and Tabakoff, W., "Heat Transfer by a Square Array of Round Air Jets Impinging Perpendicular to a Flat Surface Including the Effect of Spent Air," ASME Journal of Engineering for Power, Vol. 92, No. 1, Jan. 1970, pp. 73-82.

6. Chance, J.L., "Experimental Investigation of Air Impingement Heat Transfer Under an Array of Round Jets," Tappi, Vol. 57, No. 6, 1974, pp. 108-112.

7. Gardon, R., and Cobonpue, J., "Heat Transfer Between a Flat Plate and Jets of Air Impinging on It," International Developments in Heat Transfer, Proceedings of 2nd International Heat Transfer Conference, ASME, New York, N.Y., 1962, pp. 454-460.

8. Hollworth, B.R. and Berry, R.D., "Heat Transfer from Arrays of Impinging Jets with Large Jet-to-Jet Spacing," ASME Paper 78-GT-117, Gas Turbine Conference, London, April 1978.

9. Martin, H., "Heat and Mass Transfer between Impinging Gas Jets and Solid Surfaces," Advances in Heat Transfer, Vol. 13, Academic Press, New York, 1977, pp. 1-60.

10. Metzger, D.E., and Korstad, R.J., "Effects of Cross Flow in Impingement Heat Transfer," ASME Journal of Engineering for Power, Vol. 94, 1972, pp. 35-41.

11. Bouchez, J.P., and Goldstein, R.J., "Impingement Cooling From a Circular Jet in a Crossflow," International Journal of Heat and Mass Transfer, Vol. 18, 1975, pp. 719-730.

12. Sparrow, E.M., Goldstein, R.J., and Rouf, M.A., "Effect of Nozzle-Surface Separation Distance on Impingement Heat Transfer for a Jet in a Crossflow," ASME Journal of Heat Transfer, Vol. 97, 1975, pp. 528-533.

13. Kline, S.J. and McClintock, F., "Describing Uncertainties in Single Sample Experiments," Mech. Eng., Vol. 75, January 1953, pp. 3-8.

14. Touloukian, Y.S. and Ho, C.Y., ed., Thermophysical Properties of Matter - The TPRC Data Series, Thermal Conductivity, Vol. 3, 1970 and Viscosity, Vol. 11, 1975, Plenum, New York.

15. Gardon, R., and Akfirat, J.C., "The Role of Turbulence in Determining the Heat Transfer Characteristics of Impinging Jets," International Journal of Heat and Mass Transfer, Vol. 8, 1965, pp. 1261-1272.

APPENDIX A

CORRECTION FOR SEGMENT HEAT TRANSFER COEFFICIENTS DUE TO SURFACE TEMPERATURE DEPRESSION AT TEST PLATE SEGMENT INTERFACES

Nomenclature for Appendix A

a = half-width of Lexan strip

A = total heat transfer surface area associated with test plate segment, $(A_c + A_L)$

A_c = heat transfer surface area of copper segment

A_L = heat transfer surface area of Lexan strip

b = thickness of Lexan strip

Bi_L = Biot number, $h_L\ a/k_L$

h = heat transfer coefficient at surface of copper segment

h_L = heat transfer coefficient at surface of Lexan strip

h_{ref} = reference condition heat transfer coefficient for total segment surface area, A (assumes precisely isothermal surface)

k_L = thermal conductivity Lexan strip

n = summation index

N = $\pi\ (n + 1/2)$

Q = heat rate from total surface area (A) associated with test plate segment

Q_L = heat rate from surface area (A_L) of Lexan strip

Q_L^* = normalized heat rate from Lexan strip, $Q_L/[h_L A_L\ (T_s - T_r)]$

T = temperature

T_r = fluid reference temperature for defining heat transfer coefficient (equivalent to adiabatic wall temperature)

T_s = temperature at surface of copper test plate segment

x = space coordinate

y = space coordinate

Consider the detailed construction of the heat transfer test plate as illustrated in Fig. 2.4 of the main text. Even if one considers that the surface of each copper segment is isothermal at the same temperature level, the entire heat transfer surface will not be precisely isothermal since there will be a temperature depression at the surface of each of the thin Lexan strips located between the copper segments. The maximum temperature depression would occur if the Lexan were a perfect insulator. In this limiting case, the appropriate surface area to use in computing a segment heat transfer coefficient via Eq. (3.1) would be just the surface area, A_C, of the copper segment itself, over which the surface temperature would be assumed uniform at T_S. This would provide an upper limiting value for h. The lower limit would occur for the assumption of zero temperature depression. In this limit the total heat transfer surface area associated with each segment (copper segment plus Lexan strip surface area, $A = A_C + A_L$) would be used in Eq. (3.1). Take this lower limit (isothermal test plate surface) as a reference case. Then

$$h_{ref} = \frac{Q}{A(T_s - T_r)}$$

where Q is the heat rate from the total surface area A.

Now, since it is more nearly correct to assume a uniform temperature only over the surface of the copper segment itself, the actual segment heat transfer coefficient may be written as

$$h = \frac{Q - Q_L}{A_C(T_s - T_r)}$$

where Q_L is the heat rate from the Lexan strip surface area.

The above two equations may be combined and rewritten in the form

$$\frac{h}{h_{ref}} = \frac{1 + A_L/A_C}{1 + Q_L^*(h_L/h)(A_L/A_C)} \qquad (A.1)$$

where

$$Q_L^* = \frac{Q_L}{h_L A_L (T_s - T_r)}$$

Q_L^* is the heat rate from the Lexan strip surface normalized by the heat rate which would occur if the strip surface were at a uniform temperature, T_S.

The appropriate correction to h_{ref} depends on both Q_L^* and h_L/h, according to Eq. (A.1). The range of h_L/h may be estimated from the data of Appendix B. Q_L^* can be estimated based on a two-dimensional model for heat conduction from the copper segments through the Lexan strip to the surface of the strip. This model is outlined below.

Referring to Fig. 2.4, it was assumed that the temperatures along the opposing surfaces of the strip in direct contact with (i.e., bonded to) the copper were uniform at a value equal to the copper segment surface temperature, T_s. The lower edge of the Lexan strip in contact with the balsawood was assumed to be adiabatic, while a convective boundary condition was imposed at the upper edge which forms a part of the test plate heat transfer surface. The model is illustrated in Fig. A.1, where the symmetry about the midplane between the copper segments has been utilized.

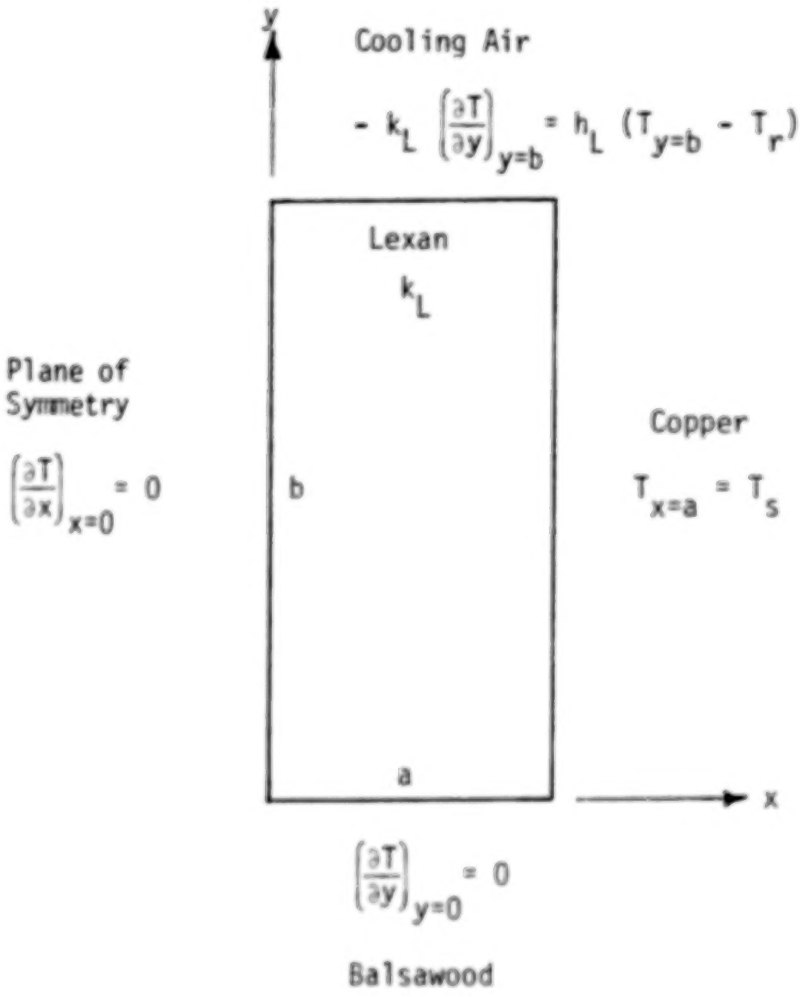

Fig. A.1 Two-dimensional heat conduction model for heat flow through cross-section of Lexan strip separating copper test plate segments.

The solution to the Laplace equation, for T(x,y) subject to the boundary conditions indicated in Fig.A.1, may be found by the classical technique of separation of variables. The result may be written in the form

$$\frac{T_s - T}{T_s - T_r} = 2Bi_L \sum_{n=0}^{\infty} \frac{(-1)^n \cos(Nx/a)\cosh(Ny/b)}{N[N\sinh(Nb/a) + Bi_L \cosh(Nb/a)]}$$

where

$$N = \pi(n + \tfrac{1}{2})$$

If this solution is used to compute the heat rate from the convective surface at y = b, the result, normalized by the heat rate which would occur if the surface were at a uniform temperature T_s, may be written as

$$Q_L^* = 2 \sum_{n=0}^{\infty} \frac{1 - \exp(2Nb/a)}{N[(N + Bi_L) - (N - Bi_L)\exp(2Nb/a)]}$$

In the present case the half-thickness, a, of the Lexan strip is 0.040 cm (1/64 in.), while b = 0.079 cm (1/32 in.), so that b/a = 2. Based on the range of heat transfer coefficients from the data of Appendix B, the range of Bi_L was about 0.1 to 5. Evaluation of Q_L^* indicated that over this range of Bi_L, Q_L^* was essentially independent of b/a for b/a $\geq$ 2. This indicates that the assumption of an adiabatic surface at y = 0 is valid for the present conditions.

For $0.1 < Bi_L < 5$, and b/a $\geq$ 2, one finds $0.30 < Q_L^* < 0.95$. Detailed examination based on the data of Appendix B indicated that for the bulk of the conditions encountered, $Q_L^*(h_L/h)$ values were such that h/h_{ref} values from Eq. (A.1) fell between 1.01 and 1.05. If the arithmetic mean of A and A_c is used in Eq. (3.1) to compute h, then h/h_{ref} is just 1.032. Therefore, final computation of segment heat transfer coefficients was based on the use of Eq. (3.1) with the area taken as the arithmetic mean of A and A_c. This results in an uncertainty in h due to this correction of $\pm$ 2% for a confidence level of about 95%.

APPENDIX B

TABULAR DATA

This Appendix contains tabular data for all test configurations summarized in Table 2.1. Mean Nusselt numbers ($\overline{Nu}$) and segment Nusselt numbers (Nu) are tabulated as a function of mean jet Reynolds number ($\overline{Re}$) for each configuration. Also tabulated are the plenum temperature (T_o), the plenum pressure (P_o), and the exhaust-to-plenum pressure ratio (P_e/P_o) for each test run.

Segment Nusselt numbers are listed according to segment number counted from the upstream end of the channel.

The data are presented in order of increasing plenum/jet plate assembly size (A, B, C, and D). For each size the inline hole pattern data (I) is listed first followed by the staggered pattern data (S). For each given size and hole pattern, the data is tabulated in order of increasing hole spacings and channel heights.

In examining the segment Nusselt number data, the reader is urged to keep in mind the relationship between the spanwise jet hole rows and the test plate segments as illustrated in Fig. 2.3. This is particularly important for the C-size data, as previously discussed in Section 4.2, to preclude possible misinterpretation.

SIZE (x_m/d, y_m/d) HOLE PATTERN	z/d	$\overline{Re}$ (10^3)	$\overline{Nu}$	Segment Nu (by Segment Number)					T_o(K)	P_o(kPa)	P_e/P_o
				1	2	3	4	5			
A(10,6)I	1	5.5	18.4	19.4	15.7	16.7	18.5	21.7	296.1	153.	.636
		10.1	29.2	31.2	25.9	26.0	29.0	33.7	300.4	248.	.391
		19.5	49.9	53.7	44.8	44.4	49.1	57.7	307.8	490.	.198
	2	4.9	17.1	21.3	17.1	15.4	15.5	16.1	295.9	118.	.825
		9.3	25.6	31.2	27.1	23.8	22.5	23.4	298.2	163.	.595
		16.0	41.4	49.8	43.7	40.6	37.0	36.1	305.5	295.	.329
	3	5.7	19.8	25.4	20.6	19.0	17.1	16.9	295.3	111.	.874
		9.8	25.6	33.5	28.4	26.5	22.5	22.3	297.9	161.	.604
		19.5	43.8	56.8	47.5	43.6	37.3	37.1	303.8	346.	.281
	6	5.7	17.8	22.2	18.8	18.1	16.0	14.1	294.2	111.	.874
		10.2	26.1	32.5	28.2	26.4	23.2	20.4	296.6	180.	.540
		19.7	38.8	50.5	42.3	39.5	32.3	29.6	303.9	353.	.276
A(10,8)I	1	4.9	17.5	19.2	16.2	16.0	17.1	19.2	297.6	145.	.668
		10.5	29.6	33.4	28.8	27.1	28.0	30.7	302.1	236.	.411
		20.4	49.9	55.2	48.3	46.9	47.5	51.7	306.5	441.	.221
	2	5.1	15.2	18.5	15.7	14.2	13.6	13.8	295.3	114.	.847
		10.3	25.4	30.5	27.1	24.5	22.2	22.5	298.8	159.	.609
		20.2	40.6	48.7	44.1	39.7	35.8	34.8	303.9	290.	.334
	3	5.2	15.7	18.6	16.7	15.5	13.9	13.5	296.1	113.	.856
		10.0	25.3	30.3	27.4	25.3	22.3	21.1	298.4	151.	.643
		20.0	39.7	47.3	43.6	39.7	34.8	33.0	304.6	289.	.336
A(10,6)S	1	4.8	15.5	14.7	12.8	14.5	16.2	19.4	295.7	140.	.693
		9.4	24.9	25.1	20.7	22.9	25.8	30.1	298.3	233.	.417
		20.1	46.4	46.6	41.3	41.7	46.8	55.5	302.3	477.	.203
	2	4.6	15.0	18.9	15.3	14.2	13.4	13.4	296.1	115.	.848
		9.9	26.0	32.4	27.6	24.6	23.2	22.3	298.2	169.	.580
		17.4	39.0	48.6	42.1	37.1	34.6	32.8	302.6	273.	.353
	3	4.8	15.1	19.7	16.2	14.5	13.3	11.9	296.5	113.	.861
		9.9	25.2	32.5	27.5	24.7	22.0	19.4	298.5	158.	.616
		16.1	34.7	45.7	38.7	32.9	30.0	26.4	301.9	238.	.408
	6	4.9	14.0	18.3	15.6	14.2	12.1	9.8	296.4	112.	.862
		9.8	23.0	29.8	26.0	23.7	19.6	15.9	298.9	154.	.630
		15.9	31.1	41.0	35.6	31.9	26.2	21.2	302.1	234.	.413

SIZE (x_n/d, y_n/d) HOLE PATTERN	z/d	$\overline{Re}$ (10^3)	$\overline{Nu}$	Segment Nu (by Segment Number)										T_o(K)	P_o(kPa)	P_e/P_o
				1	2	3	4	5	6	7	8	9	10			
B(5,4)I	1	5.1	27.0	24.4	19.7	19.9	20.6	22.2	24.5	28.1	31.4	36.5	42.2	301.3	102.	.946
		9.4	41.7	38.3	30.6	30.3	32.1	34.6	37.9	43.6	48.4	56.4	64.6	311.9	117.	.826
		11.4	46.7	42.9	34.8	34.2	36.0	38.9	42.5	48.8	54.0	63.5	71.9	314.6	124.	.779
	2	4.9	26.5	32.2	27.2	26.0	24.8	24.9	24.6	25.6	25.7	26.7	27.7	300.2	98.	.980
		9.9	42.0	49.0	43.5	41.2	39.1	39.2	39.1	40.4	41.8	42.9	44.7	311.1	104.	.931
		11.8	47.8	55.0	49.9	47.1	44.8	44.6	44.4	46.0	46.2	48.8	51.0	312.3	107.	.904
	3	4.9	25.5	33.6	28.2	28.1	26.1	24.5	23.5	23.2	22.3	22.6	22.6	301.6	98.	.985
		9.7	40.2	50.4	45.3	45.2	41.6	38.8	36.9	36.2	35.3	35.8	36.2	309.6	101.	.953
		11.6	46.5	58.4	53.0	52.4	48.2	44.5	42.6	41.7	40.7	41.6	42.1	311.4	104.	.933
		20.8	69.1	82.2	78.5	76.2	72.0	67.9	63.9	61.4	62.1	63.5	63.2	294.8	116.	.836
B(5,8)I	1	4.9	21.8	25.7	19.3	19.8	19.4	19.8	20.2	21.6	22.1	24.1	25.5	296.0	99.	.977
		9.5	34.9	40.7	35.4	32.6	31.3	31.6	32.1	34.0	34.4	37.4	39.3	299.6	104.	.929
		18.5	59.0	65.2	59.8	57.8	55.6	55.2	55.3	57.7	57.5	61.9	64.7	309.2	124.	.781
	2	4.9	22.5	27.1	24.0	23.7	22.3	21.8	21.1	21.6	20.7	21.4	21.3	294.0	98.	.986
		9.4	37.7	43.6	40.7	39.9	38.6	37.5	35.7	35.8	34.4	35.2	35.2	299.9	101.	.957
		19.4	61.4	68.4	65.3	64.3	63.7	62.4	59.9	59.3	56.3	57.6	57.1	308.3	113.	.852
	3	4.8	24.0	29.3	25.5	25.8	24.6	23.9	22.7	23.0	21.8	22.1	21.8	294.0	98.	.987
		9.5	38.2	43.6	40.2	40.5	39.5	39.1	37.1	37.2	35.0	35.1	34.5	299.6	101.	.961
		18.2	51.7	67.2	64.6	63.1	62.8	64.3	61.1	60.1	59.0	58.9	56.7	308.3	112.	.862
		19.5	61.5	67.8	64.1	64.0	63.1	62.9	60.7	60.8	57.5	57.7	56.2	310.0	113.	.859
		52.7	119.8	130.9	127.4	121.2	121.5	126.9	121.1	116.2	114.0	113.1	106.1	294.3	193.	.498
	6	4.8	22.5	26.7	22.9	23.4	22.9	22.9	21.8	22.3	20.9	21.0	20.4	296.5	98.	.988
		9.9	37.1	41.4	37.7	39.4	37.8	38.0	36.6	37.2	34.8	34.9	34.0	302.0	101.	.957
		19.1	59.2	63.1	59.3	60.1	59.7	59.6	57.5	58.2	55.3	55.5	54.0	312.2	113.	.859

SIZE (x_n/d, y_n/d) HOLE PATTERN	z/d	$\overline{Re}$ (10^3)	$\overline{Nu}$	Segment Nu (by Segment Number)										T_o(K)	P_o(kPa)	P_e/P_o
				1	2	3	4	5	6	7	8	9	10			
B(10,4)I	1	4.9	20.0	15.5	12.5	14.1	14.9	16.7	18.5	21.3	24.3	28.9	33.5	299.0	126.	.760
		9.6	32.9	26.4	21.4	22.9	24.7	27.5	30.5	34.9	40.0	47.0	53.4	304.4	191.	.506
		17.1	49.0	31.4	25.9	27.0	29.2	32.4	36.2	41.3	47.1	56.1	63.2	304.4	236.	.409
		26.3	73.8	57.8	52.4	52.1	54.4	62.2	69.0	75.1	90.1	106.4	119.1	294.2	443.	.217
	2	4.9	15.8	22.7	19.2	18.8	17.2	17.7	17.4	17.8	18.3	19.1	19.9	299.0	106.	.920
		9.5	30.6	37.4	32.5	31.8	29.1	28.5	27.8	28.5	29.0	30.2	31.4	304.8	127.	.766
		15.0	58.7	46.6	41.5	40.2	37.5	36.4	35.1	36.0	36.4	37.9	39.1	305.8	149.	.653
	3	4.6	17.5	24.4	20.0	19.3	17.9	17.1	16.1	15.4	15.1	15.0	15.1	298.3	102.	.947
		9.7	29.3	39.9	34.6	33.1	30.7	28.5	26.3	25.3	24.6	24.9	25.1	304.0	119.	.812
		12.9	35.9	48.5	43.1	40.7	37.8	35.0	32.1	30.9	30.2	30.5	30.5	306.1	135.	.718
		26.4	65.3	87.0	80.3	73.2	67.0	66.8	58.4	54.3	54.6	54.8	54.2	294.4	217.	.442
B(10,8)I	1	4.7	13.8	14.9	12.3	12.3	12.1	12.4	12.7	13.7	14.4	15.8	17.2	301.5	106.	.909
		9.6	23.9	26.9	23.1	22.6	20.9	20.8	21.4	22.9	24.1	26.8	29.5	305.6	132.	.729
		19.3	42.2	46.3	41.8	39.6	38.6	38.4	38.6	40.6	42.5	46.6	49.1	308.2	213.	.450
		26.8	69.9	73.4	69.4	64.0	62.0	65.6	66.5	66.8	72.6	78.2	80.3	294.1	365.	.266
	2	5.2	16.3	20.4	17.9	17.7	16.7	15.8	15.0	14.9	14.6	15.0	15.2	296.8	102.	.948
		10.8	27.2	32.6	30.3	29.9	28.5	27.1	25.9	25.1	24.3	24.4	24.5	299.6	117.	.829
		19.0	43.1	51.0	48.5	47.9	45.7	43.5	41.2	39.8	38.3	37.9	37.5	306.9	168.	.574
	3	4.9	17.0	21.0	18.6	18.7	18.0	17.3	16.3	15.5	14.9	14.9	14.7	296.0	101.	.950
		9.7	27.2	32.3	29.9	29.8	29.0	28.2	26.6	25.2	24.0	23.7	23.4	299.1	116.	.832
		14.6	42.6	49.4	47.1	46.7	45.6	44.6	42.1	39.7	37.6	37.0	35.8	304.9	160.	.604
		52.4	92.6	95.8	93.6	87.1	85.9	88.9	83.1	75.9	75.2	72.9	67.5	293.5	407.	.236

SIZE (x_n/d, y_n/d) HOLE PATTERN	z/d	$\overline{Re}$ (10^3)	$\overline{Nu}$	Segment Nu (by Segment Number)										T_o(K)	P_o(kPa)	P_e/P_o
				1	2	3	4	5	6	7	8	9	10			
B(5,4)S	1	4.7	22.9	23.8	18.9	18.9	17.4	18.5	20.4	23.2	25.3	29.1	33.7	300.0	101.	.955
		8.2	34.9	38.2	31.0	29.4	27.9	30.3	33.3	37.5	41.3	46.9	53.6	307.0	113.	.854
		12.8	46.0	47.6	39.5	36.4	34.5	37.8	41.3	46.3	51.2	58.3	66.9	308.5	127.	.759
	2	4.7	21.7	31.2	25.4	24.0	22.2	20.5	19.2	19.2	18.3	18.1	18.9	299.8	99.	.982
		9.5	39.4	46.8	41.1	38.5	35.1	32.3	30.7	30.3	29.0	29.3	30.6	309.0	103.	.939
		12.4	42.7	56.7	51.5	47.9	44.2	40.4	38.0	37.4	36.1	36.5	38.1	310.1	108.	.900
	3	4.8	21.2	32.4	26.4	25.8	24.4	21.3	18.8	18.2	16.2	14.6	14.1	300.3	99.	.987
		9.3	33.8	49.0	43.3	41.6	38.7	33.6	29.8	28.7	25.9	23.8	23.1	309.2	101.	.955
		11.5	39.3	55.8	50.7	47.9	44.7	39.2	34.4	32.7	31.2	28.7	27.7	308.9	103.	.935
		12.2	39.9	56.3	51.1	49.5	46.1	39.7	35.3	33.9	30.7	28.6	28.0	310.9	104.	.928
		21.0	59.1	81.4	76.0	72.4	67.3	59.6	51.8	49.3	47.1	43.6	42.2	294.6	115.	.840
B(5,8)S	1	5.1	21.7	24.6	19.1	20.1	17.6	20.0	20.2	21.9	22.2	24.0	25.8	295.0	100.	.978
		9.5	34.9	41.0	36.7	34.7	30.5	31.0	31.5	33.7	34.1	36.7	39.0	299.5	103.	.935
		18.3	56.6	63.9	60.1	57.9	54.2	51.9	51.1	53.6	53.7	58.3	61.0	309.3	122.	.796
	2	4.9	22.6	28.2	24.4	24.6	23.0	22.4	21.1	21.0	20.2	20.7	20.6	295.1	98.	.987
		9.7	37.6	45.0	41.1	41.2	39.4	38.5	36.8	35.4	32.8	33.3	32.9	300.7	101.	.956
		15.6	59.8	68.2	64.3	64.5	62.9	61.8	59.3	58.3	55.9	52.8	52.4	309.4	113.	.855
	3	4.9	22.5	28.0	24.4	24.4	23.7	23.0	21.7	21.2	19.8	19.8	19.2	294.9	98.	.987
		9.1	35.8	42.1	38.9	38.7	38.0	37.0	35.1	34.5	31.9	31.3	30.2	299.3	100.	.964
		19.4	61.5	68.6	66.2	65.7	65.0	63.8	61.1	60.0	56.5	55.6	52.6	310.5	114.	.854
	6	5.1	21.8	27.4	23.1	23.7	22.5	22.4	21.0	20.8	19.6	19.3	17.9	296.1	102.	.941
		10.2	35.8	42.5	39.1	39.2	38.3	37.3	35.1	34.2	32.2	31.2	29.0	300.2	101.	.956
		20.0	55.7	63.2	61.0	61.2	60.1	58.6	54.8	52.9	50.3	49.2	45.7	310.2	113.	.856

SIZE (x_n/d, y_n/d) HOLE PATTERN	z/d	$\overline{Re}$ (10^3)	$\overline{Nu}$	Segment Nu (by Segment Number)										T_o(K)	P_o(kPa)	P_e/P_o
				1	2	3	4	5	6	7	8	9	10			
B(10,4)S	1	4.9	18.5	16.5	13.2	14.0	14.1	15.5	16.6	19.1	21.4	25.1	29.6	303.9	122.	.789
		9.7	30.4	27.0	22.1	22.6	23.4	25.4	27.7	31.5	35.2	41.5	47.4	305.8	182.	.531
		12.8	37.5	33.7	28.1	27.7	28.6	31.2	34.1	38.8	43.4	51.5	58.0	306.6	235.	.411
	2	4.7	16.6	22.6	18.8	17.8	16.1	16.4	15.4	15.1	14.4	14.7	15.3	305.2	104.	.926
		9.4	27.2	35.8	31.4	29.6	26.5	26.8	25.3	24.5	23.5	23.9	24.8	306.3	124.	.777
		12.2	33.1	43.4	38.4	36.2	32.5	32.5	30.6	29.7	28.5	29.1	30.0	307.3	139.	.699
	3	4.8	16.2	24.3	19.9	18.4	16.9	16.8	15.3	14.2	12.6	12.1	11.9	307.3	102.	.943
		9.5	26.7	38.2	33.0	30.6	28.1	27.5	25.0	23.4	21.1	20.1	20.2	309.1	118.	.818
		12.3	32.1	45.4	40.3	36.9	34.0	33.1	30.2	28.1	25.3	24.2	23.9	308.5	131.	.737
B(10,8)S	1	4.8	14.5	15.8	12.9	12.5	12.3	12.7	13.2	14.6	15.6	17.0	18.4	295.9	106.	.910
		9.7	29.2	27.0	23.2	22.2	20.5	20.7	21.8	23.9	25.3	27.7	29.7	299.5	132.	.733
		19.0	40.8	46.3	40.8	37.7	36.6	35.8	35.8	39.2	41.4	45.8	48.3	306.0	213.	.453
	2	4.9	15.5	20.0	17.3	16.8	15.7	15.5	14.6	14.3	13.3	13.6	13.8	295.9	102.	.947
		9.6	26.0	32.4	29.2	28.2	26.6	26.3	25.1	24.9	23.1	22.3	21.9	299.1	116.	.830
		19.2	43.2	53.3	49.4	47.5	44.8	44.3	42.3	41.6	38.2	36.3	34.7	304.8	169.	.572
	3	4.9	16.0	21.0	17.8	17.2	16.3	16.1	15.4	15.2	14.2	13.9	13.4	296.3	102.	.951
		9.6	26.4	32.7	29.2	28.1	27.1	26.7	25.6	25.5	23.7	23.2	22.0	300.0	115.	.839
		18.9	42.8	52.2	48.1	45.6	44.0	43.3	42.4	41.4	38.5	37.1	34.5	307.1	166.	.583

SIZE $(x_n/d, y_n/d)$ HOLE PATTERN	z/d	$\overline{Re}$ (10^3)	$\overline{Nu}$	Segment Nu (by Segment Number)										T_o(K)	P_o(kPa)	P_e/P_o
				1	2	3	4	5	6	7	8	9	10			
				11	12	13	14	15	16	17	18	19	20			
C(5,4)I	1	4.9	27.5	26.7	23.4	16.7	25.2	15.0	25.6	16.9	27.0	18.8	28.1	297.7	98.	.986
				25.0	27.7	24.8	31.0	28.8	33.7	33.2	37.8	38.3	45.5			
		9.6	43.1	41.3	37.6	26.3	39.1	22.7	39.5	27.1	41.5	30.5	43.2	302.8	101.	.954
				39.0	43.4	40.1	47.3	46.3	51.7	53.8	59.1	62.1	70.7			
	2	4.9	27.4	35.0	32.5	25.8	32.5	18.9	34.5	18.1	34.2	20.7	31.7	298.0	98.	.993
				26.3	27.9	25.1	25.9	26.9	24.4	27.5	24.9	27.8	27.0			
		9.8	44.0	52.7	50.0	42.6	51.4	32.3	54.3	29.8	54.0	33.6	50.2	304.3	99.	.981
				41.4	44.5	41.0	40.7	43.9	38.9	45.8	40.5	47.5	44.1			
	3	4.8	25.2	36.6	33.5	27.1	33.7	22.0	36.1	19.1	35.9	19.2	32.8	298.9	97.	.994
				24.7	26.4	23.0	22.8	24.0	20.1	24.0	19.9	22.5	21.1			
		9.8	41.9	54.2	51.8	44.9	52.9	39.2	55.4	32.0	56.7	31.1	52.1	304.1	99.	.985
				38.3	42.0	37.2	36.1	38.6	32.4	38.2	32.5	37.9	35.1			
C(5,6)I	1	5.0	25.3	27.2	24.5	18.6	28.9	17.5	25.2	17.6	25.5	17.8	26.9	295.4	98.	.990
				22.0	27.6	20.6	30.5	23.1	32.2	25.8	33.5	28.2	37.6			
		19.2	66.8	70.2	64.9	51.5	66.3	47.3	68.1	49.7	68.1	48.8	70.4	302.8	107.	.909
				55.7	71.6	55.0	75.6	61.4	79.2	69.2	83.7	75.5	92.1			
	2	5.0	27.4	35.9	29.8	29.6	31.1	24.0	31.6	21.7	31.6	20.3	31.5	296.8	98.	.994
				22.6	30.4	19.8	31.0	21.7	29.7	24.2	27.7	25.4	29.2			
		14.8	68.9	79.0	72.5	75.2	74.7	70.1	76.4	64.2	77.8	55.1	80.6	307.0	103.	.950
				56.7	77.8	52.2	77.4	54.8	73.3	59.5	68.5	63.0	70.2			
	3	6.1	24.4	37.8	30.2	31.3	31.1	29.7	31.4	25.6	32.1	21.4	33.0	296.5	98.	.994
				23.1	31.7	19.8	32.9	20.4	31.9	21.7	30.3	22.8	29.9			
		19.1	71.0	82.8	74.5	76.7	76.2	75.8	75.7	72.5	77.5	63.0	82.1	305.8	102.	.951
				58.9	81.8	52.1	80.4	52.4	77.4	56.2	74.0	57.7	71.3			

SIZE (x_n/d, y_n/d) HOLE PATTERN	z/d	$\overline{Re}(10^3)$	$\overline{Nu}$	Segment Nu (by Segment Number)										T_o(K)	P_o(kPa)	P_e/P_o
				1 11	2 12	3 13	4 14	5 15	6 16	7 17	8 18	9 19	10 20			
C(5,8)I	1	4.6	21.7	25.4 19.5	21.4 23.1	17.5 17.5	20.4 25.4	16.7 18.7	21.9 26.7	16.6 20.7	22.8 28.1	16.3 21.5	23.3 29.9	296.9	97.	.993
		19.7	63.4	69.4 55.4	64.6 66.8	62.5 52.2	65.2 69.7	54.6 54.6	66.7 71.8	52.8 58.8	66.9 74.9	51.9 62.2	67.9 79.0	304.3	104.	.928
	2	5.0	25.0	32.7 21.6	26.8 27.0	24.9 18.6	27.7 27.9	24.1 18.9	28.1 27.9	21.5 19.7	28.5 27.6	19.5 20.1	28.5 27.2	296.4	97.	.994
		21.4	65.7	75.4 59.5	70.3 73.0	69.5 51.6	69.9 72.6	66.1 51.0	69.7 71.9	64.1 52.4	71.0 70.2	59.5 53.0	74.2 69.4	303.4	102.	.952
	3	4.6	24.2	32.6 21.7	25.7 26.2	26.2 14.1	26.1 26.6	24.3 17.2	27.1 26.9	23.0 18.0	26.7 26.5	20.5 18.0	27.3 26.2	295.6	98.	.995
		20.6	70.7	80.3 68.1	72.7 76.5	73.6 59.0	73.1 76.5	72.4 55.8	72.5 79.2	72.1 55.0	73.8 77.2	68.1 53.6	76.2 75.6	303.2	102.	.952
C(10,4)I	1	4.9	19.0	13.6 14.9	15.1 21.2	6.2 15.9	16.4 23.5	8.9 19.0	17.0 27.0	9.3 22.8	19.0 31.5	10.9 26.6	20.4 37.4	297.9	102.	.948
		9.4	30.1	20.1 25.8	24.1 33.2	13.1 26.0	26.3 37.5	13.7 30.9	27.7 42.7	15.1 37.2	30.2 49.3	18.0 43.2	32.3 57.9	304.1	115.	.843
		11.3	34.8	24.8 27.3	28.5 38.5	15.4 30.2	30.3 43.1	15.5 35.9	32.0 49.2	17.4 43.0	34.7 56.4	20.8 50.1	37.3 65.4	306.2	124.	.781
	2	4.8	19.0	20.8 13.7	20.1 21.3	14.3 14.0	21.4 20.2	11.6 15.7	22.8 19.6	9.7 17.6	23.7 19.3	10.1 18.6	24.1 20.0	297.8	99.	.981
		10.6	32.1	38.4 23.6	36.8 37.2	28.8 24.7	38.2 34.8	23.5 27.8	40.6 34.4	19.2 30.9	42.1 34.0	18.4 33.3	41.6 35.4	303.7	105.	.926
		12.6	36.2	43.1 26.5	41.1 41.6	33.0 27.8	43.0 39.2	27.2 31.4	45.2 38.9	20.9 34.8	47.4 38.4	20.9 37.6	46.5 39.9	304.6	108.	.898
	3	4.8	17.4	24.1 12.9	22.6 20.3	17.2 12.8	23.4 17.5	13.3 14.0	24.5 15.8	10.8 15.2	25.1 14.9	9.8 15.5	24.3 14.9	297.7	99.	.986
		9.4	28.6	38.7 20.9	37.1 32.4	29.7 21.0	37.9 28.1	23.5 23.2	39.4 25.9	18.8 25.0	40.4 24.4	17.0 26.0	38.9 24.3	302.5	102.	.953
		13.7	34.0	45.1 24.5	43.7 38.2	35.9 25.0	44.7 33.3	28.7 27.5	46.2 31.0	22.9 29.9	47.6 28.4	20.5 30.9	45.9 29.0	304.2	105.	.925

SIZE (x_n/d, y_n/d) HOLE PATTERN	z/d	$\overline{Re}(10^3)$	$\overline{Nu}$	Segment Nu (by Segment Number)										T_o(K)	P_o(kPa)	P_e/P_o
				1 11	2 12	3 13	4 14	5 15	6 16	7 17	8 18	9 19	10 20			
C(10,6)I	1	6.7	20.7	18.2 15.8	19.8 24.5	11.6 15.5	20.6 27.2	11.3 18.2	20.7 29.5	11.8 21.4	21.4 31.8	12.6 24.0	23.2 35.3	298.5	103.	.947
		10.4	29.1	27.4 21.4	29.7 34.0	19.7 21.8	30.4 37.5	15.7 25.5	29.8 40.0	16.5 30.1	29.9 43.2	17.6 33.2	32.2 47.5	301.7	109.	.885
		19.1	48.8	45.7 35.9	49.3 56.7	36.1 37.4	50.0 60.6	30.6 43.3	52.3 64.8	28.4 50.5	52.0 68.3	30.6 55.3	55.0 73.6	303.5	138.	.700
	2	6.8	20.1	24.8 13.1	23.9 24.5	15.9 12.3	23.6 25.0	18.4 13.6	23.9 24.4	14.2 15.5	25.0 25.0	11.9 16.6	25.5 23.5	298.2	100.	.980
		9.8	28.9	34.6 18.6	34.2 35.5	29.2 17.2	33.5 35.3	27.5 19.1	33.8 34.4	23.2 21.7	35.2 32.6	18.7 23.3	37.3 32.4	302.1	103.	.950
		19.1	47.7	55.5 31.5	55.5 59.4	49.6 28.2	55.2 57.5	46.8 31.1	54.5 56.2	41.1 35.0	57.0 53.0	34.9 37.4	61.0 53.1	304.2	117.	.836
	3	5.4	14.9	24.3 12.5	23.0 22.8	19.5 10.3	22.3 23.7	18.1 11.4	22.2 22.7	16.0 12.8	22.7 21.3	13.5 13.6	24.0 20.7	297.4	102.	.986
		9.9	29.3	36.4 23.7	35.1 36.2	31.2 16.2	34.4 36.3	29.1 17.3	33.8 34.5	26.6 19.4	34.9 31.8	23.7 20.6	37.2 30.6	300.1	102.	.956
		19.2	47.4	57.0 35.4	56.2 58.2	51.4 27.4	54.8 58.1	48.2 28.3	53.8 54.9	44.7 31.4	55.3 50.8	40.8 33.0	58.8 49.2	307.4	113.	.854

SIZE (x_n/d, y_n/d) HOLE PATTERN	z/d	$\overline{Re}(10^3)$	$\overline{Nu}$	Segment Nu (by Segment Number)										T_o(K)	P_o(kPa)	P_e/P_o
				1 11	2 12	3 13	4 14	5 15	6 16	7 17	8 18	9 19	10 20			
C(10,8)I	1	5.1	15.0	14.6 12.1	14.3 17.6	9.0 11.2	14.8 17.9	9.7 12.4	15.6 20.8	10.0 13.8	16.5 22.2	10.2 14.9	17.3 24.7	296.5	100.	.972
		10.2	25.5	26.6 19.9	27.7 28.8	20.1 16.3	27.7 31.1	17.3 20.2	27.6 33.4	15.8 22.8	27.7 35.9	16.1 24.9	28.5 39.5	297.9	105.	.932
		25.5	49.8	50.8 37.9	53.7 56.3	40.9 37.6	54.1 59.4	36.7 40.6	54.1 63.0	34.0 44.8	55.8 65.1	34.1 48.5	58.2 70.2	305.8	139.	.696
	2	5.1	16.4	19.7 11.9	19.1 19.3	16.5 10.0	18.8 20.1	15.1 10.1	19.2 20.2	13.4 11.0	19.5 20.1	11.6 11.2	20.2 20.4	297.1	99.	.986
		9.9	26.9	32.2 20.7	31.2 31.9	28.5 16.8	30.6 32.6	26.3 16.4	30.8 32.5	23.5 17.3	31.2 31.7	21.3 17.8	32.9 32.1	298.5	102.	.956
		19.9	46.2	53.7 36.2	52.7 55.0	49.8 30.5	51.8 56.8	47.0 29.0	51.9 55.8	42.1 29.5	52.8 53.8	38.3 30.1	55.6 53.2	303.0	116.	.841
	3	4.9	16.6	20.5 13.1	19.2 19.3	17.4 10.3	19.8 19.7	16.7 10.0	18.7 19.9	15.4 10.3	19.2 19.6	13.9 10.2	19.9 19.7	295.0	98.	.987
		9.7	27.4	32.7 23.4	29.8 34.8	29.9 18.2	30.4 32.6	28.9 16.9	28.2 32.6	26.8 17.0	31.0 31.8	25.0 16.7	32.1 31.9	298.3	111.	.875
		19.7	46.5	51.8 41.0	52.1 53.1	49.4 32.4	51.4 54.3	48.4 29.8	50.1 54.6	46.8 30.0	50.8 53.2	44.9 28.5	53.3 53.4	304.1	114.	.851

SIZE (s_n/d, y_n/d) HOLE PATTERN	z/d	$\overline{Re}(10^3)$	$\overline{Nu}$	Segment Nu (by Segment Number) 1	2	3	4	5	6	7	8	9	10	T_o(K)	P_o(kPa)	P_e/P_o
				11	12	13	14	15	16	17	18	19	20			
C(5,8)S	1	5.3	23.6	24.8	23.6	23.1	25.7	18.3	24.7	17.9	24.9	17.5	25.8	296.4	97.	.992
				20.1	25.6	18.9	26.9	20.8	27.0	25.4	28.5	24.6	30.5			
		20.6	62.9	74.2	68.4	64.6	68.6	57.4	67.8	53.7	64.8	49.8	65.7	306.9	105.	.923
				58.7	60.8	48.2	68.0	53.3	68.2	54.9	70.8	61.3	75.8			
	2	5.4	25.6	35.3	28.1	29.6	29.1	27.2	28.1	24.7	28.9	21.9	27.9	296.4	97.	.994
				22.1	27.1	19.3	27.6	18.3	26.9	19.7	26.7	20.3	26.4			
		20.1	65.2	78.7	72.2	72.3	72.8	71.2	70.9	68.0	70.3	62.9	71.6	305.8	102.	.950
				62.8	70.2	52.2	70.1	48.3	64.6	48.7	64.3	50.8	63.9			
	3	5.0	24.2	32.7	26.7	27.6	27.8	25.7	26.4	25.2	26.8	22.2	26.5	296.3	97.	.995
				22.9	25.4	17.7	25.9	16.8	25.2	17.7	24.7	17.3	24.3			
		19.8	63.9	75.2	70.1	73.5	70.2	69.8	69.0	68.8	68.7	64.6	69.9	304.2	101.	.955
				63.7	68.2	52.7	68.7	47.7	65.8	46.9	61.7	46.1	60.9			
C(10,4)S	1	5.1	19.5	13.9	15.6	8.6	17.8	9.3	17.7	9.8	19.1	11.8	20.5	297.4	103.	.946
				14.8	20.3	15.5	22.1	19.2	24.8	22.8	28.9	25.6	34.8			
		19.9	29.8	22.5	26.5	13.8	27.6	14.3	28.8	15.9	30.7	18.7	31.9	301.3	117.	.832
				24.8	31.8	25.6	34.5	30.5	40.8	36.7	45.9	42.9	53.4			
		12.3	39.6	26.3	31.8	16.3	32.9	16.5	33.7	18.2	35.5	21.7	36.9	304.2	125.	.771
				28.1	34.6	33.8	40.9	35.7	46.1	42.9	52.9	49.9	61.3			
	2	4.9	16.1	19.6	20.3	14.1	22.2	10.4	23.5	9.4	23.6	10.6	21.5	297.6	99.	.982
				13.8	17.4	13.3	15.2	14.2	13.9	15.8	13.9	15.4	15.8			
		11.3	29.8	36.6	37.8	27.6	38.6	20.1	41.4	17.8	40.9	18.9	36.7	303.4	105.	.924
				25.3	29.8	23.5	26.1	25.3	24.8	27.3	24.4	28.4	26.9			
		19.1	43.3	42.8	42.5	33.5	44.4	23.9	48.8	19.8	47.2	21.8	42.1	303.4	110.	.898
				27.1	34.6	29.2	30.4	29.3	28.9	31.6	28.7	33.8	30.7			
	3	4.9	16.8	21.4	22.8	17.2	23.4	11.7	24.5	10.7	24.8	10.1	22.9	298.1	98.	.986
				15.2	18.8	12.6	15.9	12.9	11.6	12.8	11.3	11.4	11.5			
		11.1	35.8	37.9	39.8	30.3	38.7	21.6	40.8	14.5	40.3	17.2	37.7	304.9	102.	.951
				21.2	29.4	21.1	22.5	21.9	19.6	22.8	18.6	20.8	19.2			
		12.9	52.3	45.2	45.1	34.5	45.4	26.9	47.4	22.9	48.3	21.1	44.9	307.7	105.	.923
				29.3	33.2	29.2	27.9	26.4	23.7	26.6	22.4	25.2	22.9			

SIZE (x_n/d, y_n/d) HOLE PATTERN	z/d	$\overline{Re}$ (10^3)	$\overline{Nu}$	Segment Nu (by Segment Number) 1 11	2 12	3 13	4 14	5 15	6 16	7 17	8 18	9 19	10 20	T_o(K)	P_o(kPa)	P_e/P_o
C(10, 8)S	1	9.9	14.8	14.4 11.6	14.3 17.1	9.1 10.8	15.2 19.4	9.2 12.2	15.6 20.6	9.6 14.1	16.0 21.8	9.5 14.7	16.9 23.3	295.1	99.	.977
		9.9	25.0	26.4 18.4	28.0 28.2	19.9 19.1	28.1 31.4	17.3 19.9	27.6 33.0	15.2 22.4	26.5 35.1	15.3 24.2	27.4 37.2	296.4	104.	.926
		19.1	41.1	43.5 29.4	46.0 45.4	34.9 29.0	46.9 49.3	31.1 32.6	45.9 52.0	28.5 36.5	46.4 54.4	26.8 39.8	46.4 57.2	302.8	123.	.783
	2	9.9	15.5	19.8 12.1	18.8 17.8	15.9 9.6	18.9 18.3	14.6 9.0	18.7 18.0	13.1 9.6	18.7 18.4	11.4 9.7	18.9 18.5	295.3	97.	.986
		10.1	26.6	32.2 21.5	31.6 31.2	27.8 18.0	31.5 31.8	25.9 16.4	31.5 30.5	23.3 16.4	31.8 30.3	20.9 16.3	32.8 30.0	298.0	101.	.955
		19.7	45.1	53.1 36.9	52.5 52.9	47.8 32.2	52.4 53.6	44.2 30.3	51.9 52.3	40.5 29.7	52.3 50.9	36.7 28.2	54.5 49.8	303.7	114.	.846
	3	9.8	16.4	21.1 13.5	20.0 18.9	16.9 11.0	19.7 19.3	15.5 10.3	19.7 18.9	14.5 10.2	19.6 18.7	12.8 9.7	20.0 18.2	295.2	98.	.987
		9.8	26.6	32.3 22.4	31.8 30.7	27.8 18.9	31.2 31.1	25.5 17.4	31.0 30.9	24.3 16.8	30.9 30.0	21.9 15.8	31.9 28.9	297.3	110.	.884
		19.6	44.5	51.9 36.4	52.0 50.6	46.9 32.8	51.3 51.7	43.6 30.9	50.4 51.0	41.7 29.7	50.7 50.3	38.2 27.9	52.1 48.8	302.6	113.	.859

CONTENTS

	Page	
SUMMARY	1	1/A5
NOMENCLATURE	3	1/A7
1. INTRODUCTION	5	1/A9
2. EXPERIMENTAL FACILITY	9	1/A13
3. EXPERIMENTAL PROCEDURES AND DATA REDUCTION	18	1/B9
3.1 Typical Test Runs	18	1/B9
3.2 Segment Heat Transfer Coefficients	18	1/B9
3.3 Corrections and Experimental Uncertainties	20	1/B11
3.4 Reproducibility	22	1/B13
4. EXPERIMENTAL RESULTS	23	1/B14
4.1 Presentation Variables and Parameters	23	1/B14
4.2 Documentation of Data Base	25	1/C2
4.3 Geometrically Similar Configurations	26	1/C3
4.3.1 Mean Nusselt Numbers	26	1/C3
4.3.2 Low-Resolution Nusselt Number Profiles	27	1/C4
4.3.3 Statistical Analysis	32	1/C9
4.4 Low-Resolution Heat Transfer Characteristics	36	1/C13
4.4.1 Effect of Channel Height	36	1/C13
4.4.2 Effect of Hole Diameter	37	1/C14
4.4.3 Effect of Hole Spacing	39	1/D2
4.4.4 Effect of Hole Pattern	40	1/D3
4.5 Higher-Resolution Heat Transfer Characteristics	42	1/D5
5. SUMMARY OF RESULTS	54	1/E10
6. CONCLUDING REMARKS	56	1/F9
REFERENCES	58	1/E14
APPENDIX A - CORRECTION FOR SEGMENT HEAT TRANSFER COEFFICIENTS DUE TO SURFACE TEMPERATURE DEPRESSION AT TEST PLATE SEGMENT INTERFACES	60	1/F2
APPENDIX B - TABULAR DATA	64	1/F6

SIZE (x_n/d, y_n/d) HOLE PATTERN	z/d	$\overline{Re}$ (10^3)	$\overline{Nu}$	Segment Nu (by Segment Number)										T_o(K)	P_o(kPa)	P_e/P_o
				1	2	3	4	5	6	7	8	9	10			
				11	12	13	14	15	16	17	18	19	20			
				21	22	23	24	25	26	27	28	29	30			
		4.3	28.7	29.8	29.4	22.8	13.9	27.1	23.0	15.8	23.5	25.5	17.6	301.0	97.	.992
				25.8	25.7	20.4	23.1	28.3	23.4	25.9	29.9	26.9	28.1			
				33.6	31.6	32.2	36.8	35.2	36.2	41.4	40.3	41.1	48.0			
		11.5	52.1	48.9	52.6	42.3	26.0	47.0	43.3	27.4	40.3	46.2	32.8	307.2	99.	.968
				43.8	48.6	38.8	40.9	52.6	45.0	44.0	55.1	50.5	50.9			
				59.6	57.4	59.0	66.9	66.9	64.8	75.1	76.2	73.4	86.6			
	1															
		20.9	77.5	67.8	73.6	61.5	40.9	76.6	63.2	40.0	59.6	70.0	48.4	292.6	105.	.918
				60.3	74.8	57.6	59.6	78.4	67.9	65.9	81.6	75.9	73.6			
				89.8	89.6	84.0	100.3	100.5	95.4	114.1	115.0	109.1	130.4			
		34.5	109.5	91.8	98.6	84.9	65.1	105.7	87.5	57.4	86.5	99.2	68.9	295.2	119.	.810
				78.6	105.5	82.7	83.1	111.3	97.8	91.8	115.4	109.4	102.5			
				127.4	128.0	118.5	142.5	143.8	134.5	164.6	164.1	154.5	182.0			
		4.8	28.9	32.6	40.5	30.3	19.7	40.9	28.7	17.7	35.4	32.0	19.0	303.0	97.	.995
				31.2	33.9	22.6	21.9	36.2	26.2	22.0	32.9	28.3	23.4			
				30.0	30.3	25.5	28.2	30.7	27.8	28.6	31.9	29.3	29.7			
D(5,4)I	2	15.6	63.6	65.8	80.3	65.4	53.9	82.1	64.2	43.0	80.9	69.2	45.1	292.5	99.	.979
				64.1	77.0	50.5	46.8	78.4	59.0	46.6	72.6	63.7	49.7			
				67.8	70.0	55.2	62.8	71.1	60.3	61.6	72.1	64.6	65.0			
		34.6	109.2	109.3	127.3	110.2	98.9	131.8	111.0	83.3	139.7	116.6	79.9	292.6	105.	.917
				118.3	130.8	86.9	78.7	132.1	100.5	80.1	126.4	109.4	84.0			
				114.7	120.0	94.0	109.0	123.9	104.0	105.7	124.6	113.0	111.6			
		4.9	28.0	35.7	42.4	29.7	19.8	42.5	29.2	18.3	40.6	31.8	18.8	301.7	98.	.996
				33.8	34.8	20.8	21.6	37.5	24.8	20.0	34.0	26.7	20.1			
				30.3	28.6	22.1	25.8	28.5	23.9	23.8	27.6	24.5	23.3			
	3	15.5	59.8	67.6	85.2	63.3	52.4	85.5	63.9	48.2	85.8	67.7	44.1	293.8	98.	.984
				70.6	74.6	48.2	44.3	76.8	54.8	43.1	70.9	57.8	43.7			
				63.5	62.0	47.7	52.7	60.1	51.1	48.9	58.1	52.8	49.3			
		34.7	103.9	111.1	141.1	108.8	96.0	141.0	110.9	89.7	142.6	117.1	80.9	294.8	103.	.936
				124.5	128.4	85.2	80.6	130.7	95.6	76.3	122.1	100.7	77.4			
				110.0	108.3	83.4	90.0	105.2	89.7	85.8	101.9	93.4	88.1			

SIZE (x_n/d, y_n/d) HOLE PATTERN	z/d	$\overline{Re}$ (10^3)	$\overline{Nu}$	Segment Nu (by Segment Number)										T_o(K)	P_o(kPa)	P_e/P_o
				1	2	3	4	5	6	7	8	9	10			
				11	12	13	14	15	16	17	18	19	20			
				21	22	23	24	25	26	27	28	29	30			
		4.8	19.5	9.5	21.8	12.9	6.4	18.4	13.1	8.9	16.8	15.5	9.9	300.6	99.	.975
				17.6	17.0	12.3	15.6	19.8	14.7	18.0	22.1	16.9	19.9			
				25.5	20.3	22.7	28.5	23.5	26.1	34.1	27.6	29.5	38.9			
		10.4	33.9	14.8	40.5	23.0	11.4	32.5	23.3	14.7	28.9	27.8	17.5	314.5	107.	.901
				28.6	31.3	21.6	27.3	35.8	26.4	30.2	39.3	30.3	33.3			
	1			44.8	36.3	37.7	50.3	41.6	42.7	58.1	48.9	49.3	68.0			
		10.6	34.0	13.3	40.6	23.1	11.0	32.2	23.8	14.5	28.3	28.4	17.4	307.8	107.	.902
				27.7	32.1	21.5	26.9	35.9	26.3	29.7	39.3	30.5	33.1			
				45.0	36.7	37.7	50.8	42.0	43.0	60.0	49.5	49.6	68.8			
		34.6	83.0	39.7	91.1	57.0	28.8	91.0	58.3	34.0	74.8	71.0	44.2	294.1	181.	.533
				62.6	82.2	53.9	63.6	90.0	67.2	70.2	99.5	77.3	78.3			
				111.6	92.2	89.6	125.4	104.8	99.4	144.3	123.7	111.8	152.6			
		4.9	19.2	16.0	33.2	16.9	9.0	32.5	16.5	9.8	28.0	18.4	9.9	300.3	98.	.989
				25.3	20.0	11.6	17.8	23.2	14.0	16.3	23.4	15.8	15.6			
				23.9	17.8	16.3	25.1	18.9	17.5	22.5	20.6	18.8	22.0			
D(10,4)I	2	9.9	31.8	28.0	52.6	29.2	16.8	54.0	28.7	16.5	48.1	32.0	17.2	307.0	100.	.965
				39.3	34.9	19.7	28.5	39.1	23.0	25.0	39.4	25.8	24.7			
				39.9	29.4	25.8	38.1	31.5	28.0	37.5	34.1	30.1	36.9			
		34.5	79.3	69.6	114.7	74.9	47.5	120.7	77.9	42.7	118.5	83.6	48.1	293.5	129.	.748
				91.2	93.2	49.9	67.6	98.0	59.4	58.3	99.4	65.5	59.8			
				100.9	74.5	63.3	96.2	80.4	68.8	96.1	87.0	75.7	93.4			
		5.1	19.8	19.1	35.9	20.3	10.9	35.9	19.0	10.8	31.1	20.4	11.1	300.2	97.	.991
				27.2	21.3	11.9	17.3	24.5	13.8	13.2	23.4	15.0	12.5			
				22.1	16.7	13.3	19.2	16.9	14.6	16.9	17.3	15.0	15.9			
	3	13.3	34.3	34.3	62.4	38.0	22.8	64.0	35.7	20.1	58.5	39.0	21.6	308.5	101.	.962
				47.1	41.0	22.6	30.6	44.5	25.5	23.0	42.0	27.3	22.3			
				39.6	30.4	23.9	34.7	31.6	26.0	31.6	32.7	27.7	29.6			
		34.9	73.2	75.3	121.9	80.5	54.6	127.5	77.8	45.5	121.5	82.9	49.1	292.4	121.	.797
				95.6	87.1	50.3	65.0	92.0	55.7	49.0	88.8	58.8	48.1			
				84.2	64.9	51.5	76.1	69.0	56.0	69.2	71.3	60.3	66.6			

SIZE (x_n/d, y_n/d) HOLE PATTERN	z/d	$\overline{Re}$ (10^3)	$\overline{Nu}$	Segment Nu (by Segment Number)										T_o(K)	P_o(kPa)	P_e/P_o
				1	2	3	4	5	6	7	8	9	10			
				11	12	13	14	15	16	17	18	19	20			
				21	22	23	24	25	26	27	28	29	30			
		4.3	14.1	10.5	20.1	11.3	5.3	16.9	11.5	7.3	16.2	12.2	7.5	296.7	97.	.990
				18.5	12.5	8.3	16.3	14.1	9.0	16.9	14.7	9.9	17.1			
				16.0	11.1	17.6	17.4	11.8	18.7	19.2	13.1	19.8	20.6			
	1	22.5	50.3	36.1	73.2	46.4	26.2	71.0	46.1	24.6	65.9	48.0	25.9	307.4	114.	.848
				59.5	51.9	28.6	56.8	54.0	33.0	55.0	55.0	36.0	54.0			
				58.2	40.6	55.3	61.4	43.7	56.5	66.4	48.5	60.2	70.9			
		52.9	93.7	72.4	129.6	85.5	54.2	130.2	85.9	47.8	123.7	90.1	49.3	293.1	172.	.564
				105.6	97.8	55.3	105.7	99.0	64.7	101.7	103.1	70.8	100.1			
				108.6	79.4	102.3	114.0	86.2	101.1	121.9	94.4	105.8	125.9			
		4.6	16.5	17.0	27.2	16.1	10.4	27.7	14.6	9.9	26.1	15.7	8.6	296.8	97.	.993
				26.3	15.4	9.0	22.0	16.7	9.6	20.3	16.5	9.9	18.9			
				17.3	10.8	17.8	17.8	11.2	17.1	18.6	11.8	16.3	19.4			
D(10,8)I	2	20.3	48.9	45.7	73.2	46.1	38.6	74.9	44.9	35.9	75.5	45.9	30.9	311.0	106.	.911
				72.2	49.1	26.7	70.1	49.7	27.7	65.7	50.5	28.3	58.5			
				52.7	30.9	52.0	53.2	32.3	46.2	55.0	34.1	44.3	56.3			
		52.7	95.2	89.7	136.4	93.2	78.9	140.3	92.7	74.7	141.6	93.4	66.0	293.1	147.	.656
				128.5	99.2	55.7	133.8	98.5	57.0	123.5	100.9	58.3	108.8			
				103.8	62.7	97.7	105.3	66.2	83.8	107.7	69.8	80.9	108.1			
		4.7	16.8	17.7	27.0	16.6	11.5	28.1	14.9	11.3	27.7	15.1	9.6	296.9	97.	.993
				29.2	15.2	8.9	25.5	16.0	9.1	23.2	16.1	9.5	19.9			
				16.9	10.3	18.3	17.2	10.5	17.1	17.7	10.8	16.2	18.1			
	3	19.6	47.8	44.0	70.1	45.7	38.4	72.2	44.0	36.8	72.4	43.1	34.5	308.7	105.	.924
				71.2	45.8	31.5	72.0	45.0	29.3	69.3	44.9	26.4	62.7			
				47.7	28.5	54.6	48.9	29.6	47.5	50.9	30.5	44.6	51.5			
		53.2	97.9	91.0	138.3	95.1	82.7	142.1	93.8	80.6	143.3	91.1	77.6	292.2	145.	.668
				132.6	96.6	69.3	142.8	93.3	64.4	138.1	93.1	57.1	126.0			
				98.4	59.1	110.8	100.8	61.5	93.9	105.7	63.8	88.0	106.4			

SIZE (x_n/d, y_n/d) HOLE PATTERN	z/d	$\overline{Re}$ (10^3)	$\overline{Nu}$	Segment Nu (by Segment Number)										T_o(K)	P_o(kPa)	P_e/P_o
				1	2	3	4	5	6	7	8	9	10			
				11	12	13	14	15	16	17	18	19	20			
				21	22	23	24	25	26	27	28	29	30			
		5.0	15.9	6.5	16.9	8.3	4.0	14.5	9.0	6.4	13.8	10.2	7.0	299.4	102.	.941
				15.6	12.3	8.6	14.0	15.5	10.8	15.6	17.8	13.3	16.3			
				20.8	16.0	19.8	24.8	19.2	22.8	30.0	23.1	26.9	35.9			
	1	11.8	30.0	9.4	34.9	15.2	7.4	26.9	16.7	11.2	25.3	20.4	13.8	306.8	126.	.764
				25.8	25.4	17.2	24.5	29.7	21.8	27.6	34.2	25.9	30.8			
				40.4	31.8	36.1	47.7	38.0	41.4	57.6	45.5	48.4	67.4			
		12.0	29.2	9.2	35.8	15.9	7.5	28.1	17.2	11.2	26.9	21.2	14.4	295.0	117.	.825
				26.4	26.4	17.5	25.7	31.2	22.3	28.0	35.2	26.3	29.9			
				41.2	31.3	34.4	46.0	35.6	36.9	53.1	41.0	40.8	59.2			
		34.6	68.5	19.8	81.9	38.8	19.1	75.2	41.3	26.9	66.0	51.7	35.7	296.3	231.	.418
				56.7	64.5	43.2	60.1	74.0	54.8	64.6	84.0	64.8	69.1			
				95.4	76.7	78.6	106.6	85.9	84.9	120.3	96.9	92.0	125.3			
		5.0	15.2	9.5	27.2	11.7	6.5	24.4	11.7	7.4	21.7	12.9	7.4	300.0	99.	.979
				20.8	14.6	8.7	16.0	17.6	10.4	14.2	18.6	11.9	13.3			
				19.7	13.6	13.8	20.2	14.7	14.4	20.7	16.0	15.3	21.6			
		11.3	27.3	15.6	49.1	21.2	10.4	47.1	22.1	12.9	40.5	24.7	13.8	307.3	106.	.911
				34.3	27.8	15.3	27.5	32.0	18.6	24.2	33.9	21.2	22.1			
D(15,4)I	2			35.3	24.1	23.5	36.5	26.6	24.8	37.9	29.4	26.9	39.3			
		11.8	28.2	16.5	50.4	22.0	10.9	48.6	23.0	13.3	41.6	25.3	14.5	294.7	106.	.912
				34.8	29.0	15.9	28.3	32.8	19.3	25.0	34.9	21.8	23.6			
				37.0	25.2	24.3	38.1	27.5	25.3	39.2	30.3	27.5	40.6			
		35.1	65.6	37.7	108.7	52.3	26.3	109.7	57.2	31.9	97.5	63.0	36.1	294.1	168.	.577
				76.4	69.7	38.6	66.7	75.3	45.7	57.4	80.6	53.1	53.3			
				84.1	61.2	57.3	86.4	67.2	60.1	88.5	72.8	65.1	87.7			
		4.7	13.6	10.6	29.0	11.7	5.6	27.2	12.2	6.7	23.2	13.4	7.1	300.2	98.	.986
				21.1	14.0	7.6	15.3	16.4	8.9	11.4	16.8	9.9	9.8			
				16.8	11.2	10.0	16.1	11.9	10.6	14.8	12.6	11.1	13.9			
	3	11.8	24.2	19.9	53.1	23.8	12.1	51.9	24.9	13.2	44.7	26.9	14.7	309.2	104.	.933
				37.0	28.1	15.5	28.0	31.5	17.8	21.8	32.6	19.5	18.6			
				32.9	21.9	18.8	31.3	23.4	19.8	29.1	24.8	21.2	27.3			
		35.5	59.0	43.0	112.6	54.5	29.7	111.0	59.6	30.5	100.0	63.3	34.4	294.7	147.	.659
				75.4	68.3	37.2	61.9	71.1	42.2	47.3	73.9	44.9	42.4			
				74.5	50.7	43.2	69.0	53.4	45.3	63.6	56.7	49.2	61.1			

SIZE (x_n/d, y_n/d) HOLE PATTERN	z/d	$\overline{Re}$ (10^3)	$\overline{Nu}$	Segment Nu (by Segment Number)										T_o(K)	P_o(kPa)	P_e/P_o
				1	2	3	4	5	6	7	8	9	10			
				11	12	13	14	15	16	17	18	19	20			
				21	22	23	24	25	26	27	28	29	30			
	1	4.7	13.3	7.3	17.8	8.3	3.9	14.4	9.3	6.0	13.9	9.9	6.7	298.0	99.	.969
				16.0	10.3	7.8	14.9	12.4	8.9	15.9	14.0	10.3	15.8			
				16.2	11.9	16.9	18.2	13.6	18.5	20.7	15.5	20.3	23.2			
		18.7	37.7	14.9	58.4	27.2	11.7	51.7	27.2	15.3	44.5	30.5	18.4	306.5	133.	.719
				41.4	32.5	21.9	38.6	36.6	26.1	40.5	40.4	30.3	41.6			
				45.9	35.5	44.3	51.1	40.3	47.5	57.6	45.8	51.1	63.8			
	2	4.7	13.8	10.3	25.9	11.2	5.8	24.5	11.4	6.8	22.6	11.8	6.8	297.0	98.	.985
				21.8	11.9	7.1	17.7	13.4	7.7	16.8	14.3	9.0	15.3			
D(15,6)1				15.8	10.1	14.4	16.8	10.8	13.5	17.3	11.6	13.3	18.1			
		17.8	37.3	25.9	68.4	31.3	17.9	67.1	32.9	17.8	64.1	33.5	19.2	305.9	114.	.857
				62.4	34.3	19.5	52.9	37.4	20.6	46.6	38.6	22.4	39.1			
				41.7	25.6	36.0	44.1	28.2	34.1	46.7	30.7	32.9	48.0			
	3	4.6	13.5	12.4	26.8	11.0	6.4	26.1	11.3	6.7	24.9	11.2	6.5	297.8	97.	.987
				25.1	11.0	6.2	20.8	12.3	6.5	18.4	12.6	7.2	15.9			
				13.8	8.1	14.1	14.8	8.9	12.5	15.4	9.6	11.8	16.0			
		17.3	36.4	31.3	68.3	30.4	22.7	66.6	32.0	19.7	64.8	32.3	19.2	306.8	108.	.887
				66.1	31.6	18.0	58.3	34.2	18.8	52.2	34.7	19.9	42.8			
				37.1	21.6	36.2	39.4	23.5	31.5	41.5	25.4	29.0	42.3			

SIZE (x_n/d, y_n/d) HOLE PATTERN	z/d	$\overline{Re}$ (10^3)	$\overline{Nu}$	Segment Nu (by Segment Number)										T_o(K)	P_o(kPa)	P_e/P_o
				1	2	3	4	5	6	7	8	9	10			
				11	12	13	14	15	16	17	18	19	20			
				21	22	23	24	25	26	27	28	29	30			
		4.9	12.0	8.9	18.2	7.7	3.8	15.1	8.8	5.6	14.7	9.5	6.2	296.1	99.	.976
				16.6	9.3	6.8	14.8	10.6	7.4	15.6	11.1	8.4	16.1			
				12.5	9.5	16.8	13.7	10.5	17.7	15.3	11.7	18.9	17.2			
		4.9	12.1	7.1	18.4	7.7	3.7	16.0	8.6	5.4	15.2	9.3	6.2	296.7	98.	.976
				17.0	9.3	6.7	15.5	10.8	7.4	16.3	11.1	8.4	16.4			
				12.6	9.5	17.4	13.7	10.5	18.4	15.1	11.8	19.6	17.3			
	1	20.2	36.2	17.4	61.8	26.4	11.1	57.2	26.4	13.9	52.9	28.4	16.7	306.0	124.	.775
				48.6	30.8	19.4	45.4	33.5	22.9	46.3	34.7	25.9	45.2			
				38.5	29.5	47.6	41.6	32.9	47.7	46.3	36.0	50.2	49.8			
		20.3	36.7	18.6	62.9	27.5	11.2	57.7	28.3	15.0	52.5	29.9	17.4	304.7	125.	.771
				51.2	31.8	19.8	44.9	34.8	23.1	44.9	35.9	26.2	45.2			
				39.2	30.2	46.7	42.7	33.3	47.0	46.7	36.6	48.9	50.8			
		52.0	73.8	39.2	121.0	59.3	24.4	118.5	60.3	29.6	107.6	64.1	36.7	295.0	223.	.433
				87.3	71.9	42.7	91.1	75.2	51.3	91.3	78.1	57.2	88.3			
				82.5	63.9	91.2	84.7	68.0	87.6	92.4	72.6	84.0	92.9			
		4.8	13.0	11.4	24.7	11.1	5.8	24.1	10.7	6.4	22.7	11.1	6.3	296.8	98.	.986
				22.4	11.0	6.5	18.0	12.1	6.9	17.0	12.1	7.4	16.0			
				12.9	8.1	15.4	13.5	8.5	14.7	14.4	9.2	14.2	15.1			
D(15,8)I	2	17.9	35.6	28.2	63.8	30.9	20.7	62.5	31.1	19.4	62.5	30.7	18.5	304.5	113.	.855
				63.2	31.2	17.2	54.5	34.1	18.3	50.7	34.3	19.1	45.1			
				34.6	21.0	41.4	37.5	22.4	36.6	38.4	23.9	35.3	40.0			
		51.1	71.4	53.9	128.4	63.4	42.1	129.2	65.3	39.3	130.9	66.3	39.9	294.2	193.	.499
				107.8	70.4	35.9	112.0	70.9	40.4	97.9	71.5	41.2	84.3			
				73.9	45.7	70.9	75.2	49.0	63.3	79.5	53.5	60.4	79.6			
		4.7	13.1	13.1	24.9	11.8	6.8	24.1	11.4	6.9	23.6	11.2	6.5	296.7	98.	.987
				24.5	10.9	6.0	20.6	12.0	6.3	18.7	12.3	7.0	16.3			
				13.1	7.5	14.8	13.4	7.9	13.7	13.7	8.2	13.0	14.3			
	3	18.4	34.8	27.0	62.3	30.4	21.3	61.9	30.8	19.8	61.6	31.3	19.5	304.3	110.	.872
				59.0	31.1	16.9	58.6	32.0	16.5	55.4	32.0	16.7	48.6			
				33.7	18.6	42.3	35.1	19.8	34.9	36.6	20.7	32.0	37.3			
		53.9	71.7	56.0	124.9	61.8	46.0	124.3	65.3	43.8	126.1	67.3	45.1	293.5	197.	.491
				110.1	68.3	34.8	120.9	68.2	38.9	111.3	69.9	38.5	91.6			
				71.0	41.0	74.8	73.6	43.1	66.1	77.9	46.3	60.1	77.8			

BLANK PAGE

BLANK PAGE

SIZE (x_n/d, y_n/d) HOLE PATTERN	z/d	$\overline{Re}(10^3)$	$\overline{Nu}$	Segment Nu (by Segment Number)										T_o(K)	P_o(kPa)	P_e/P_o
				1	2	3	4	5	6	7	8	9	10			
				11	12	13	14	15	16	17	18	19	20			
				21	22	23	24	25	26	27	28	29	30			
		5.0	27.9	26.7	32.2	24.7	14.5	30.5	24.9	16.3	23.8	26.2	18.2	302.1	97.	.991
				21.7	24.3	20.9	20.9	25.8	23.7	24.1	27.3	26.9	27.5			
				30.7	31.0	30.3	33.7	34.6	34.5	38.4	39.5	38.7	43.4			
	1	17.1	62.6	57.7	69.0	57.6	35.4	66.8	60.1	37.5	49.8	61.3	44.9	293.6	103.	.942
				44.9	57.3	48.4	45.6	58.5	56.0	52.4	60.5	62.4	58.8			
				65.4	72.4	66.6	73.2	81.8	75.9	82.7	93.1	86.1	95.0			
		37.7	112.0	102.7	114.6	99.7	71.3	122.8	106.5	70.8	80.5	109.6	85.4	295.0	123.	.785
				75.6	102.6	89.1	80.3	102.4	103.0	91.1	107.0	113.0	103.6			
				116.6	131.2	118.0	132.2	148.5	134.9	152.3	169.3	155.1	170.8			
D(5,4)S		5.2	24.9	34.7	44.1	31.5	19.4	42.6	31.0	19.2	35.1	34.0	20.8	301.7	97.	.996
				29.8	34.9	23.0	17.6	32.0	25.9	19.7	21.8	24.1	20.6			
				19.1	21.1	19.7	18.0	18.4	19.2	17.8	16.8	17.7	17.3			
	3	17.2	55.0	68.9	91.5	68.0	52.0	90.5	69.5	47.3	81.5	75.9	50.1	293.6	98.	.981
				57.6	77.4	52.1	39.7	61.2	56.4	43.5	46.9	53.1	45.5			
				41.7	48.3	44.9	39.8	42.4	44.1	40.5	38.9	40.5	39.1			
		37.7	93.9	113.1	149.2	114.4	95.0	148.7	117.8	84.2	137.4	128.3	88.5	296.4	104.	.924
				96.1	131.5	89.5	70.0	100.4	96.3	74.8	77.9	89.9	77.7			
				70.9	82.2	77.0	68.9	75.3	77.3	71.9	69.6	71.7	70.1			

1. Report No. NASA CR-3217	2. Government Accession No.	3. Recipient's Catalog No.
4. Title and Subtitle MULTIPLE JET IMPINGEMENT HEAT TRANSFER CHARACTERISTIC - EXPERIMENTAL INVESTIGATION OF IN-LINE AND STAGGERED ARRAYS WITH CROSSFLOW		5. Report Date January 1980 6. Performing Organization Code
7. Author(s) L. W. Florschuetz, D. E. Metzger, D. I. Takeuchi, and R. A. Berry		8. Performing Organization Report No. ERC-R-79034 10. Work Unit No.
9. Performing Organization Name and Address Arizona State University Tempe, Arizona 85281		11. Contract or Grant No. NSG-3075 13. Type of Report and Period Covered Contractor Report
12. Sponsoring Agency Name and Address National Aeronautics and Space Administration Washington, D.C. 20546		14. Sponsoring Agency Code

15. Supplementary Notes

Final report. Project Manager, Steven A. Hippensteele, Fluid System Components Division, NASA Lewis Research Center, Cleveland, Ohio 44135.

16. Abstract

Extensive experimental results for heat transfer characteristics have been obtained for configurations designed to model the impingement cooled midchord region of air cooled gas turbine airfoils. The configurations tested were inline and staggered two-dimensional arrays of circular jets with ten spanwise rows of holes. The cooling air was constrained to exit in the chordwise direction along the channel formed by the jet orifice plate and the heat transfer surface. Tests were run for chordwise jet hole spacings of five, ten, and fifteen hole diameters; spanwise spacings of four, six, and eight diameters; and channel heights of one, two, three, and six diameters. Mean jet Reynolds numbers ranged from 5×10^3 to 5×10^4. The thermal boundary condition at the heat transfer test surface was isothermal. Tests were run for sets of geometrically similar configurations of different sizes. Mean and chordwise resolved Nusselt numbers were determined utilizing a specially constructed test surface which was segmented in the chordwise direction. Based on these results, both mean and chordwise resolved heat transfer characteristics are presented in graphical form and discussed in detail as a function of mean jet Reynolds number and the geometric parameters, including hole pattern effects. Results for the maximum chordwise resolution of one-third the chordwise hole spacing reflect the periodic variations of the chordwise heat transfer coefficient profiles. Results resolved to one or two chordwise hole spacings show more clearly the nature of the profiles smoothed across the periodic variations. A complete tabulation of mean and resolved Nusselt number values for all test conditions covered is included as an appendix.

17. Key Words (Suggested by Author(s))	18. Distribution Statement
Jet impingement; Jet array; Heat transfer; Gas turbine; Crossflow; Impingement cooling	Unclassified - unlimited STAR Category 34

19. Security Classif. (of this report)	20. Security Classif. (of this page)	21. No. of Pages	22. Price*
Unclassified	Unclassified	84	A05

* For sale by the National Technical Information Service, Springfield, Virginia 22161

NASA-Langley, 1980

END

6-11-81

90 %

50 %